Università degli Studi di Ferrara

DOTTORATO DI RICERCA IN
"FISICA"

CICLO XXIV

COORDINATORE Prof. Filippo Frontera

Analysis of the precipitation characteristics on the Tibetan Plateau using Remote Sensing, Ground-Based Instruments and Cloud models

Settore Scientifico Disciplinare Fis/06

Dottoranda:
Gjoka Uarda

Tutor:
Dott. Porcù Federico

Anni 2009/2011

Contents

Acronyms list 5

Introduction 9

1 Precipitation over the Tibetan Plateau 11

1.1 Past and ongoing studies over the Plateau 12

1.1.1 GAME-Tibet 12

1.1.2 CAMP-Tibet 15

1.1.3 CEOP-HE and Ev-K2-CNR 17

1.1.4 SHARE-paprika Himalaya 19

1.1.5 CEOP-AEGIS. 20

1.1.6. Third Pole Environment (TPE Program) 22

1.2 Precipitation over the Tibetan Plateau 23

1.2.1 Satellite precipitation estimates. 24

1.2.2 Characteristics of precipitation systems over the Tibetan Plateau 29

2 Instruments for precipitation measure and estimate 35

2.1 Raingauge 35

2.2 Weather Radar 37

2.2.1 Single target radar equation 39

2.2.2 Multiple target radar equation 41

2.2.3 The radar equation 42

2.2.4 Observation radar system on the Tibetan Plateau 44

2.2.4.1 Beam blocking and hybrid scan. 45

2.2.4.2 Mosaic 47

2.2.4.3 Radar data quality control 48

2.2.4.4. QPE 50

2.3 Satellite systems for precipitation observations over the Tibetan Plateau 51

2.3.1 Resources for multisensor precipitation observation. 52
2.3.2 Satellite instruments for precipitation estimation over the Tibetan Plateau 54
2.3.2.1 Aqua and Terra satellite 54
2.3.2.2 DMSP satellite 60
2.3.2.3 TRMM satellite 62
2.3.2.4 CLOUDSAT satellite 63
2.3.2.5 Meteosat 7 satellite 64
2.3.2.6 FengYung-2C satellite 65

3 Data and Algorithms for precipitation retrieval over the Plateau

3.1 3-years raingauges and 3-D radar gridded data for case studies and technique calibration 67
3.1.1 Rain Gauges Data 68
3.1.2 3-D mosaic of quality controlled radar reflectivity 68
3.2 Data from Satellites sensors 70
3.2.1 MODIS data 70
3.2.2 AMSR-E data 71
3.2.3 MVIRI data 72
3.2.4 Cloudsat-CPR data 73
3.2.5 2A25 TRMM PR 73
3.3 Precipitation retrieval algorithms 73
3.3.1 Cloudsat CPR Snow rate estimation technique 74
3.3.2 C-NAW Algorithm 77
3.3.3 CDRD Algorithm 79
3.3.3.1 The forward and the inverse problem 80
3.3.3.2 The theoretical Bayesian method 81
3.3.3.3 The retrieval system 83
3.3.4 TANN Algorithm 85

3.3.4.1 Physical basis 85
3.3.4.2 Implementation over the Tibetan Plateau 87
3.3.5 GCD technique 89
3.4 Available global precipitation products 91
3.4.1 3B42-TRMM product 92
3.4.1.1 High Quality (HQ) microwave estimates 93
3.4.1.2 Variable Rain Rate (VAR) IR estimates 94
3.4.1.3 Combined HQ and VAR estimates 94
3.4.1.4 Rescaling to monthly data 95
3.4.2 CMORPH technique 96

4 Satellite precipitation estimates over the Tibetan Plateau: preliminary studies, applications and intercomparison 97

4.1. Data remapping process 97
4.2 Sensitivity analysis for rain/no-rain discrimination 100
4.2.1 Sensitivity of MODIS channels 100
4.2.2 Sensitivity of AMSR-E channels 104
4.2.3 Sensitivity of TRMM PR 108
4.3 Implementation and/or application of retrieval algorithms 109
4.3.1 Implementation of the "seasonal" algorithms 111
4.3.1.1 Snowrate retrieval from Clousat-CPR data (Kulie and Bennartz, 2009) 111
4.3.1.2 Output of the CDRD technique over the Tibetan Plateau . . 113
4.3.2 Implementation and applications of IR-based statistical Retrieval techniques 115
4.3.2.1 Application of CNAW technique 116
4.3.2.2 Application of TANN-R technique 119
4.3.2.3 Application of TANN-S technique 122
4.4 Algorithm intercomparison 124

4.4.1 Daily precipitation amount 124
4.4.2 Case studies 128
4.4.3 Annual maps 131
Conclusions 137
Bibliography 139
Acknowledgements 145

Acronyms list

AIRS	Atmospheric Infra Red Sounder
ANN	Artificial Neural Network
AMSR-E	Advanced Microwave Scanning Radiometer for EOS (onboard Aqua)
AMSU	Advanced Microwave Sounding Unit
AP	Anomalous Propagation
ASAR	Advanced Synthetic Aperture Radar (onboard ENVISAT)
AVHRR	Advanced Very High Resolution Radiometer
AWS	Automatic Weather Stations
BTD	Brightness Temperature Difference
CAMP	CEOP Asia-Australia Monsoon Project
CAPPI	Constant Altitude Plain Position Indicator
CAS	Chinese Academy of Sciences
CDRD	Cloud Dynamics & Radiation Database
CEOP	Coordinated Enhanced Observing Period
CEOP-AEGIS	Coordinated Asia-European long-term Observing system of Qinghai – Tibet Plateau hydro-meteorological processes and the Asian-monsoon systEm with Ground satellite Image data and numerical Simulations
CEOP-HE	CEOP-High Elevations
CERES	Clouds and Earth's Radiant Energy System
CMA	China Meteorological Administration
CMORPH	CPC MORPHed precipitation
C-NAW	Calibrated Negri Adler Wetzel technique
CNR	Consiglio Nazionale delle Ricerche (National Council of Research of Italy)
CPC	Climate Prediction Center
CPR	Cloud Profiling Radar (onboard CloudSat)
CRD	Cloud Radiation Database
CRM	Cloud Resolving Model
CS	Convective System
CST	Convective Stratiform Technique
DAAC	NASA's Distributed Active Archive Center
DEM	Digital Elevation Model
DMSP	Defense Meteorological Satellites Program
DSD	Drop Size Distribution
ECMWF	European Center for Medium-range Weather Forecasting
ENVISAT	European ENVIronment SATellite
EOS	Earth Observing System
EPS	European Polar Satellite
ESA	European Space Agency
ESSP	Earth Science System Pathfinder

ETS	Equitable Threat Score
EUMETSAT	European Organisation for the Exploitation of Meteorological Satellites
FAR	False Alarm Ratio
FSE	Fractional Standard Error
GAME	GEWEX Asian Monsoon Experiment
GCD	Global Convective Diagnostic
GEO	Geostationary Earth Orbit
GEWEX	Global Energy and Water Cycle Experiment
GFS	Global Forecast System Model
GMS	Geostationary Meteorological Satellite (of Japan)
GOES	Geosynchronous Operational Environmental Satellite
GPI	GOES Precipitation Index
GPROF	Goddard PROFiling algorithm
HSB	Humidity Sounder for Brazil
HPNA	High Precipitation NAW Area
IODC	Indian Ocean Data Coverage
IFOV	Instantaneous Field Of View
IOP	Intense Observation Period
IR	Infrared
ISAC	Institute of Atmospheric Sciences and Climate (CNR)
ISCCP	International Satellite Cloud Climatology Program
ISW	Index for Soil Wetness
ITP	Institute for Tibetan Plateau research
JAXA	Japan Aerospace Exploration Agency
JEXAM	China-Japan Cooperative Study on Asian Monsoon Mechanisms
LANDSAT	Land Remote-Sensing Satellite
LEO	Low Earth Orbit
LIS	Lightning Imaging Sensor
LMCS	Large Mesoscale Convective System
LST	Local Standard Time
LT	Local Time
MCS	Mesoscale Convective System
MHS	Microwave Humidity Sounder
MLP	Multi-Layer Perceptron
MODIS	Moderate Resolution Imaging Spectroradiometer
MSG	Meteosat Second Generation
MVIRI	Meteosat Visible and InfraRed Imager
MW	Microwave
NASA	National Aeronautics and Space Administration (USA)
NCEP	National Centers for Environmental Prediction
NESDIS	National Environmental Satellite, Data and Information System
NAW	Negri Adler Wetzel technique
NIR	Near infrared

NOAA	National Oceanic and Atmospheric Administration (USA)
PAPRIKA	CryosPheric responses to Anthropogenic PRessures in the HIndu Kush-Himalaya
PBL	Planetary Boundary Layer
PCT	Polarization Corrected Temperature
PDF	Probability Density Function
PI	Polarization Index
PIP	Precipitation Intercomparison Project
PMW	Passive MicroWaves
POD	Probability Of Detection
POP	Pre-phase Observation Period
PoP	Probability of Precipitation
PPI	Plain Position Indicator
PR	Precipitation Radar (onboard TRMM)
PRF	Pulse Repetition Frequency
QC	Quality Control
QPE	Quantitative Precipitation Estimation
QPF	Quantitative Precipitation Forecast
RASS	Radio Acoustic Sounding System
RADAR	RAdio Detection And Ranging
RMSE	Root Mean Square Error
RMSD	Root Mean Square Difference
RPM	Round Per Minute
RPS	Round Per Second
RR	Rainrate
SAF	Satellite Application Facility
SAR	Syntetic Aperture Radar
SEVIRI	Spinnig Enhanced Visible and Infrared Imager
SHARE	Stations at High Altitude for Research on the Environment
SI	Scattering Index
SMTMS	Soil Moisture Temperature Measurement Systems
SPOT	Système Pour L'Observation de la Terre
SSM/I	Special Sensor Microwave/Imager
SSMIS	Special Sensor Microwave Imager/Sounder
SSP	Sub Satellite Point
SWE	Snow Water Equivalent
SWIR	Short Wave Infrared
TANN-R	Tibet Artificial Neural Network – trained with Radar data
TANN-S	Tibet Artificial Neural Network – trained with Satellite data
TB	Brightness Temperature
TBV	Brightness Temperature (vertical polarization)
TBH	Brightness Temperature (horizontal polarization)
TCI	TRMM Combined Instrument
TIPEX	Chinese national Tibetan Plateau Experiment

TIROS	Television InfraRed Observing System
TMPA	TRMM Multisensor Precipitation Analysis
TPE	Third Pole Environment
TS	Threat Score
TMI	TRMM Microwave Imager
TRMM	Tropical Rainfall Measuring Mission
UH	Upper-tropospheric Height
UTC	Coordinated Universal Time
UW–NMS	University of Wisconsin – Non-hydrostatic Modeling System
VCP	Volume Coverage Patterns
VIRS	Visible InfraRed Scanner
VIS	Visible
VLF/LF	Very Low Frequency/Low Frequency
VWC	Vegetation Water Content
WCRP	World Climate Research Programme
WMO	World Meteorological Organization
WRF	Weather research and Forecasting model

Introduction

Tibetan Plateau represents an unique environment from many geophysical points of view: with an average elevation higher than 4,000 m above sea level, it is characterized by complex interactions of atmospheric, cryospheric, hydrological, geological and environmental processes that have special significance for the Earth's climate and water cycles. Moreover, these processes are critical for the life of the 1.5 billion people living in the Plateau and surrounding regions in many ways, e.g. in the onset of Asian Monsoon.

Despite the Plateau key role, there is a critical lack of knowledge, because the current estimates of the Plateau water cycle are based on sparse and scarce observations that can not provide the required accuracy, statistical significance spatial and temporal resolution for quantitative studies and reliable monitoring, especially on a climate change perspective. This is particularly true for precipitation, probably the geophysical parameter with highest spatial and temporal variability.

The constantly increasing availability of Earth system observation from space-borne sensors makes the remote sensing an effective option for a wide range of geophysical measurements and estimates, with different levels of accuracy. A large number of precipitation estimation techniques have been proposed in the literature, based on different methodological approaches and making use of data in various spectral bands.

The aim of this work is to set up a multi-platform observational tool for the precipitation monitoring over the Tibetan Plateau. Ground based observational network data are used to calibrate and validate a set of satellite precipitation estimation techniques purposely implemented to work on Tibetan Plateau. The considered techniques make use of various approaches and attempt to exploit the currently available spectrum of satellite measures.

This Thesis is structured as follows. In Chapter one the research in meteorology carried out on the Tibetan Plateau is reviewed, with special emphasis on studies on cloud structure and precipitation characteristics, and on the implementation of satellite estimation techniques. The CEOP-AEGIS Project, which funded my PhD work is also introduced.

In Chapter two the resources for precipitation studies over the Plateau are presented. Raingauge network and ground weather radars, made available to this study by the China Meteorological Administration, are introduced with a description of the pre-processing algorithms. The space-borne sensors considered in this work are also described.

Chapter three is devoted to the description of the data used and the algorithms considered in this work. Some algorithms have been implemented from the literature, others have been originally developed for the use over the Tibetan Plateau. In other cases, algorithm outputs are analyzed.

In Chapter four the results are reported for the three year 2008-2010, and for selected case studies, providing validation of the retrievals and intercomparison among the different approaches. Finally, conclusions are drawn.

Chapter 1

Precipitation over the Tibetan Plateau

Human life and the entire ecosystem of South East Asia depend upon the Asian monsoon system onset, strength, decay and predictability. More than 60% of the earth's population lives in these regions, where droughts and floods due to the variability of precipitation intensity and distribution frequently cause serious damage to ecosystems in these regions and, more importantly, injury and loss of human life.

The headwater areas of seven major rivers in South-East Asia, i.e. Yellow River, Yangtze, Mekong, Salween, Irrawaddy, Brahmaputra and Ganges, are located in the Tibetan Plateau (see Figure 1.1). Despite the relevance of accurate monitoring, estimates of the Plateau water balance rely on sparse and scarce observations that cannot provide the required accuracy, spatial density and temporal frequency.

Figure 1.1 Tibetan Plateau and the major rivers of south east Asia.

In this chapter the main studies carried out on the Tibetan Plateau meteorological characteristics will be summarized, with particular emphasis on precipitation analysis and remote sensing, deeply related to this Thesis work.

1.1 Past and ongoing studies over the Plateau

In this section the main international Projects dealing with the Tibetan Plateau and surrounding regions are introduced, highlighting their areas of interest, the main goals and the experimental campaigns carried on.

1.1.1 GAME-Tibet

To clarify the roles of the interactions between the land surface and the atmosphere over the Tibetan Plateau in the Asian monsoon system, a series of international efforts initiated in 1996 under the framework of the World Climate Research Programme (WCRP) / Global Energy and Water Cycle Experiment (GEWEX) Asian Monsoon Experiment (GAME) Tibet (GAME-Tibet) project.
The interdisciplinary GAME-Tibet project (1996-2001) has been an international, land-atmosphere interaction field experiment implemented in the Tibetan Plateau both at the Plateau scale and at meso-scale. The overall goal of GAME-Tibet was to study the land surface and atmosphere processes and interactions over the Tibetan Plateau. To achieve this goal, the scientific objectives of GAME-Tibet were to improve the quantitative understanding of land-atmosphere interactions over the Tibetan Plateau, to develop process models and methods for applying them over large spatial scales, and to develop and validate satellite-based retrieval methods.
GAME-Tibet started in 1996 with two experimental phases, the pre-phase observation period (POP) in 1997 and the intensive observation period (IOP, May

to September) in 1998, contributed to international research activities in the related science fields by providing the whole resulting dataset through the GAME-Tibet Data Information System in year 2000, when started the most rewarding part of project efforts for the analysis of results and the testing of new theories, models and algorithms. In Figure 1.2 is reported the distribution of experimental sites for IOP, including: towers for Planetary Boundary Layer (PBL) measurements; Weather Doppler Radar; radiosonde and ballon stations; Automatic Weather Stations; Sodar, Portable Automatic Mesonet for flux measurements, Soil Moisture Temperature Measurement Systems, and hydrological stations.

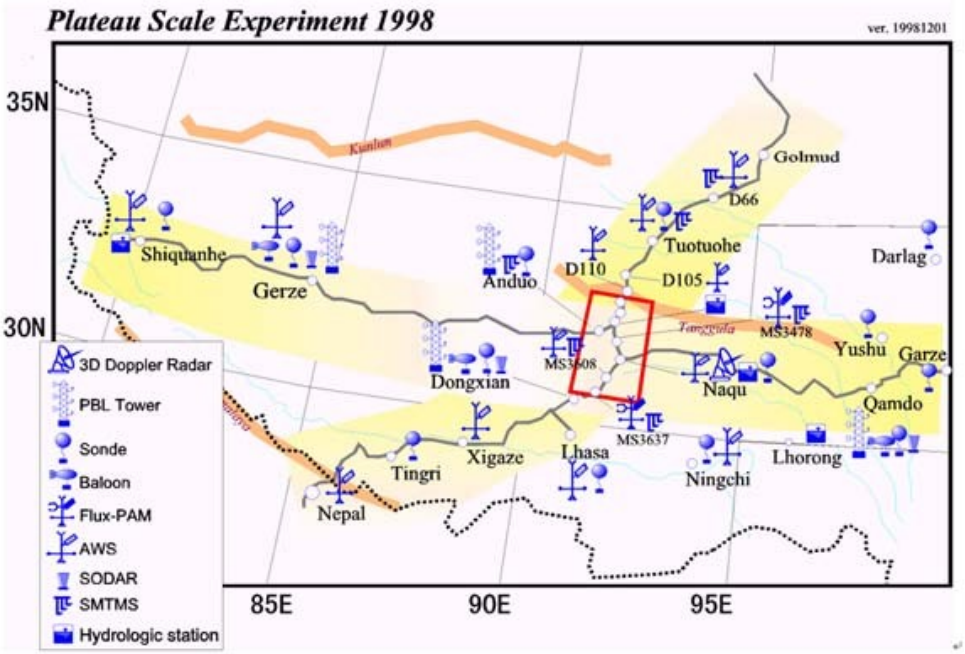

Figure 1.2. Observation area for the GAME-Tibet IOP in 1998.

The process-, modeling-, and satellite-based studies were carried out in cooperation with the Chinese national Tibetan Plateau Experiment (TIPEX) and the China-Japan Cooperative Study on Asian Monsoon Mechanisms (JEXAM) under the framework of the Joint Coordination Committee. Taking into account the importance of seasonal variations in key processes, the experiments were

carried out at two different scales, the Plateau-scale experiment and the meso-scale experiment. To understand one-dimensional land surface-atmosphere interaction processes with spatial and seasonal variations, and to develop and validate sophisticated models, the Plateau-scale experiment was carried out basically using the automatic weather station (AWS) and radiosounding networks. The meso-scale experiment was implemented in the central Plateau, by using two- and three-dimensional intensive observing systems.

GAME-Tibet covered the north to south transect observation of the Plateau-scale experiment and the whole meso-scale one. The following measurements were done during the IOP by the efforts of GAME-Tibet.

Land surface - atmosphere interaction:

- Boundary Layer measurements by using the AWSs at the 14 stations, the PBL Tower at Amdo, and the turbulent flux measurement at Amdo and BJ site.
- Intensive radio-sonde observation at Amdo on selected days to investigate diurnal variations of the PBL in June, July and August.
- Barometer network for local circulation measurement.

Precipitation and cloud studies:

- 3-D Doppler radar observation about 10 km south of Naqu from the end of May to the middle of September.
- Ground-based precipitation measurement using the rain gauge network in the meso-scale area.
- A snow particle measurement system and a microwave radiometer for measurement of total water vapor and cloud liquid water content at Naqu.
- A GPS receiver for water vapor measurement at Amdo.

Land surface monitoring by satellite RS:

- Ground truth data collection of spectral reflectance, soil moisture, surface temperature and surface roughness along the north-south transect and in the west part of the Tibet.

Cold region hydrology including permafrost study:

- Soil moisture and temperature measurements along the north-south and east-west transects.
- River discharge and evaporation measurements in the meso-scale area.

Isotope Study on Precipitation and Surface Water:

- Isotope sampling for study on the origin of precipitation and its recycling along the north-south and east-west transects.
- Isotope sampling for understanding formation processes of stable isotopic composition in the meso-scale experimental field.

The GAME-Tibet project was a major element of the Coordinated Enhanced Observing Period (CEOP) Phase I initiative. CEOP was initiated as a major step towards bringing together the research activities in GEWEX Hydrometeorology Panel (GHP) /GEWEX and related projects in WCRP (CLIVAR; CLiC). CEOP has now developed into an important element of WCRP. The Tibetan Plateau is selected as the Key study area of the CEOP Phase II. The synergistic use of ground and satellite data to study the global energy and water cycle is the core of CEOP.

1.1.2 CAMP-Tibet

In the CEOP framework, a GAME-Tibet follow on project was focused on heath and evapotranspiration fluxes between land and atmosphere. The CEOP Asia-Australia Monsoon Project on the Tibetan Plateau (CAMP/Tibet) lasted from 2001 to 2005 (Ma et al., 2003). The objectives of CAMP/Tibet were: (1) Quantitative understanding of an entire seasonal hydro-meteorological cycle including winter processes by solving surface energy "imbalance" problems in the Tibetan Plateau; (2) Observation of local circulation and evaluation of its impact on Plateau scale water and energy cycle; and (3) establishment of quantitative observational methods for entire water and energy cycle between land surface and atmosphere by using satellites. To achieve the scientific objectives of

CAMP/Tibet, a meso-scale observational network (150×250 km^2, 91-92.50^{o}E, 30.7-33.30^{o}N) were implemented and will be set up in the central Plateau, along the Naqu river, as shown in Figure 1.3.

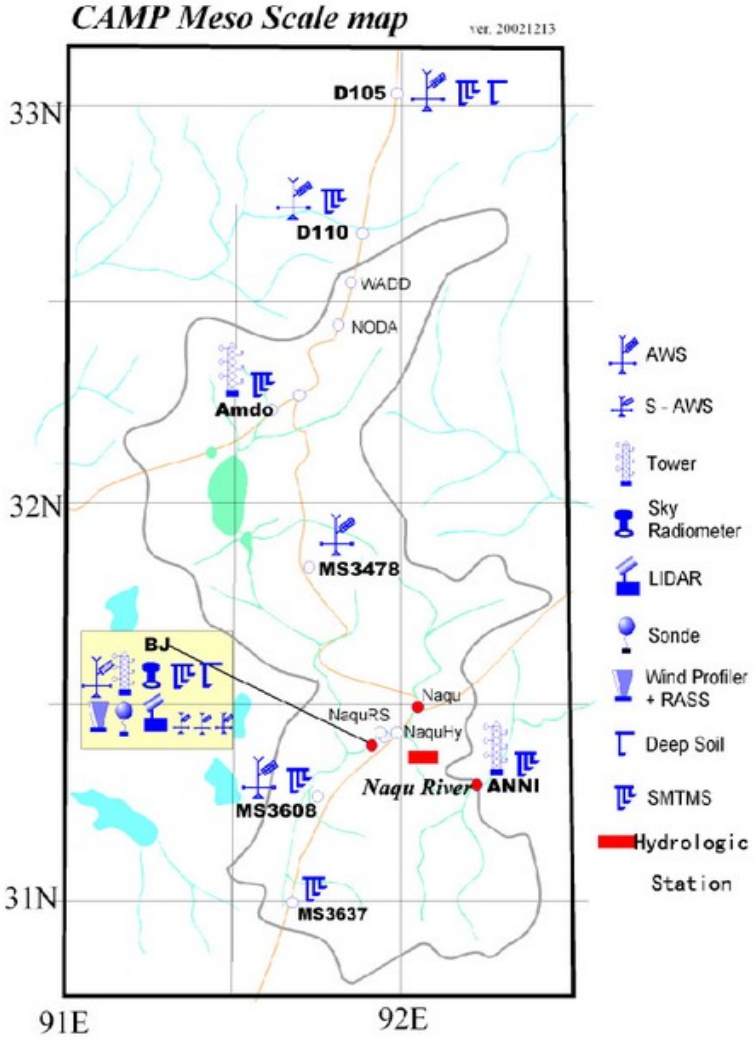

Figure 1.3. IOP area of CAMP/Tibet along the Naqu river with the indications of instruments distribution. Gray solid line indicates the Dasa basin.

The area was equipped with the following instruments: Automatic Weather Stations, sky radiometer, tower for PBL measure, wind profiler and Radar Acoustic Sounding System (RASS), lidar, deep soil probes, radiosonde, Soil Moisture Temperature Measurement Systems, and hydrological stations. The

main station, in BuJao (BJ in Figure 1.3), is located on the wide and plain grassland, which belongs to the sub-frigid climate zone, with annual average temperature between −0.9 °C and −3.3 °C. During the year, there is no absolute frost-free period. The climate is arid, low temperature, very sandy from November to March of every year, and it is warm and rainy with 80% of the precipitation occurring from May to September, every year (Li et al., 2011).

1.2.3 CEOP-HE and Ev-K2-CNR

The Tibetan-Himalaya-Hindu Kush region is one of the areas of interest of CEOP–HE (High Elevations): a working group implemented in early 2008 as a new component of "regional focus" within CEOP Phase II “project of projects”.
CEOP-HE is a concerted, international and interdisciplinary effort aimed to advance knowledge on physical and dynamical processes at high elevations while contributing to global climate change and water cycle studies. CEOP-HE addresses the current lack of harmonic, quality datasets in the majority of the world’s high elevation regions and the need for improved dialogue amongst researchers concerned with this data. In this context, the term “high elevations” should be understood to include obvious factors such as altitudes along and above the timberline, high plateaus, rough relief, low atmospheric pressure and low average temperature, although sites that directly create or influence regional climate patterns (e.g., water supply) or allow for monitoring of boundary layer dynamics are also taken into consideration.
Main peculiarity of CEOP-HE research is related to the extremes characteristics of these sites, whose conditions of low pressure and temperature as well as the inhomogeneous landscape roughness of the high altitude areas could affect data quality and representativeness. It is furthermore important taking into account that high elevation areas are often located in developing countries where the carrying out of capacity buildings activities is very important for local populations.

The overall goal of CEOP-HE within the GEWEX/CEOP Projects is to study multi-scale variability in hydro-meteorological and energy cycles in high elevation environments, improving observation, modelling and data management.
In particular, to achieve the above goal, specific HE objectives are:

- to improve the understanding of the energy cycle and climate change in mountain regions, promoting long-term monitoring and establishing a consolidated network of observatories located at high altitude, with the perspective of coordinating a Global High Elevations Watch;
- to study the water cycle in high elevation regions with particular attention to climate change effects on glaciers, permafrost, hydrology and mountain ecosystems;
- to improve the understanding of aerosol influence on energy and water cycles in high elevation areas;
- to promote and develop research activities in case study areas located at high elevations at the worldwide level.

The initiative was launched and is coordinated by the Ev-K2-CNR Committee, an autonomous, non-profit association, which promotes scientific and technological research in mountain areas, especially on the Hindu Kush – Karakorum – Himalaya region, in Nepal, Pakistan, China (Tibetan Autonomous Region) and India. Ev-K2-CNR is best represented by its Pyramid Laboratory/Observatory located at 5,050 meters a.s.l. in Nepal at the base of Mount Everest. Ev-K2-CNR research has traditionally focused on the fields of Earth Sciences, Environmental Sciences, Medicine and Physiology, Anthropology, and development of new technologies. Today, Ev-K2-CNR's work is mainly organized via broad-scale integrated multi-disciplinary programs aimed at helping resolve urgent environmental and development issues. Ev-K2-CNR works through a network of national and international scientific collaborations, in particular with the Italian National Research Council (CNR).

1.1.4 SHARE-PAPRIKA Himalaya

Ev-K2-CNR launched the SHARE project (Stations at High Altitude for Research on the Environment) with the aim to promote continuous scientific observations in key high-mountain regions of the world able to contribute to knowledge on regional and global climate change. Through these activities, national and international governments are supported in order to promote sustainable development and adaptation policies against climate change effects in the mountain regions. In particular, thanks to a direct cooperation with UNEP (United Nations Environmental Program), extreme attention is devoted in addressing priority issues and present themes.

Specific aims of SHARE are to improve scientific knowledge on climate variability in mountain regions, by ensuring the availability of long term, high quality data. To this aim, a global mountain observation network on atmospheric composition, meteorology and glaciology, hydrology and water resources, biodiversity and human health has been implemented and maintained. SHARE activities also plan to include the design of mitigation and adaptation strategies to oppose the effects of climate change.

Within SHARE, PAPRIKA project (CryosPheric responses to Anthropogenic PRessures in the HIndu Kush-Himalaya regions: impacts on water resources and society adaptation in Nepal) is a four year project (2010-2013) funded by French National Research Agency - Planetary Environmental Changes. The PAPRIKA-Himalaya Project focuses on current and future evolution of the cryosphere system in response to global and regional environmental changes and their consequences on water resources in four main landscape units within Nepal.

It addresses the driving physical and chemical processes acting on the evolution of the cryosphere, their evolution in a changing climate and their impact on water resource dynamics at regional scale. It also addresses perceptions and representations of the water resource and of changes in water availability, on

subsequent adaptations already implemented, and on territorial and social restructurings taking into account people's indigenous knowledge on the potential changes in natural resources and environmental hazards.

PAPRIKA is divided in two interconnected elements: 1) Water Resources Input, Climate and Anthropogenic Pressures on the Cryosphere, Climate, and Monsoon System, and 2) Impact on the Water Resource System and Population.

The first one deals with a better understanding of physical processes driving the dynamics of the glacier/ snow / precipitation system in Nepal. It includes the development of new scientific knowledge in particular linked to the impact of climate change on snow melting and delivers research results through the acquisition of atmospheric and glaciological data as well as the development of a modelling tool for the snow pack. Element 1 develops new scientific knowledge and implements the modelling tools and the downscaling methods used later in the projects.

The second element uses data and modelling outputs generated in Element 1 to provide a state-of-the-art integrated tool for analyzing snow, glacier and water production responses to large-scale Monsoon dynamics and atmospheric aerosol loadings under different climate scenarios. It includes adaptation studies to understand effective perception of change by local communities and adaptation strategies.

1.1.5 CEOP-AEGIS

In 2008 the EU Commission financed the Coordinated Asia-European long-term Observing system of Qinghai – Tibet Plateau hydro-meteorological processes and the Asian-monsoon systEm with Ground satellite Image data and numerical Simulations (CEOP-AEGIS) Project under the 7th Framework Program (FP7). The goal of this project, ending in 2012 is to:

1. construct out of existing ground measurements and current / future satellites an observing system to determine and monitor the water yield of the Plateau, i.e. how much water is finally going into the seven major rivers of SE Asia; this requires estimating snowfall, rainfall, evapotranspiration and changes in soil moisture;
2. monitor the evolution of snow, vegetation cover, surface wetness and surface fluxes and analyze the linkage with convective activity, (extreme) precipitation events and the Asian Monsoon; this aims at using monitoring of snow, vegetation and surface fluxes as a precursor of intense precipitation towards improving forecasts of (extreme) precipitations in SE Asia.

The specific objective of the project is to establish a pilot observation system built upon the elements listed below.

The Project is improving the spatial density and temporal frequency of observations over the Tibetan Plateau at the ground, by means of specific field campaigns aiming to measure radiative and turbulent fluxes, soil moisture, precipitation and precipitation characteristics, glaciers and snow meltwater. Given the scarcity of long-term, large-scale observation, are exploited satellite tools to estimate: snow and vegetation cover, surface albedo and temperature, energy and water fluxes, top soil moisture over the Plateau, glaciers and snow meltwater, precipitation. Where possible, ground and satellite estimates are merged to validate satellite products and to provide multiplatform retrieval algorithms. The use of such unprecedented data set is contributing to advance understanding of land-atmosphere interactions, monsoon system and precipitation, also linked to numerical weather and climate prediction modelling system.

A prototype observing system is to be established for large area water management by monitoring the water balance and water yield of the Plateau: its benefits on the monitoring of floods and drought in China and India are demonstrated.

Finally, CEOP-AEGIS is contributing to a GEO water theme and capacity building infrastructure for South East Asia through dissemination and capacity building activities and stakeholder panels.

1.1.6. Third Pole Environment (TPE Program)

The wide region centered on the Tibetan Plateau, stretching from the Pamir Plateau and Hindu-Kush on the west to the Hengduan Mountains on the east, and from the Kunlun and Qilian Mts on the north to the Himalayas on the south is called the "Third Pole" of the Earth, given its unique environment.

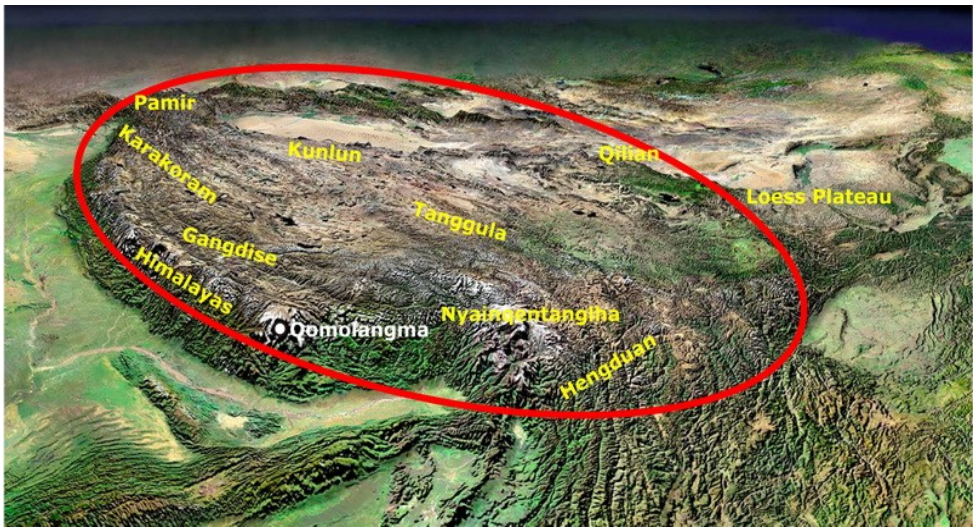

Figure 1.4. Extension of the Third Pole of the Earth.

The Third Pole region covers 5,000,000 km^2 in total and with an average elevation above 4000 m., it is home to thousands of glaciers in the tropical/sub-tropical region that exert a direct influence on social and economic development in the surrounding regions of China, India, Nepal, Tajikistan, Pakistan, Afghanistan and Bhutan. It is subjected to influences from multiple climatic systems, complicated geomorphologies and various internal and external geological impacts. The result is a region with unique interactions among the atmosphere, cryosphere, hydrosphere and biosphere. In particular, the special atmospheric processes and active hydrological processes formed by glaciers, permafrost and persistent snow are especially influential, as are the ecosystem processes acting at multiple scales. These processes compose the fundamental

basis for the unique geographical unit of the Third Pole region. The area demonstrates considerable feedbacks to global environmental changes, while interacting with and affecting each other in response to global environmental variations (Ma et al., 2011).

The TPE program (Yao and Greenwood, 2009), started in 2009, is designed to gather international efforts aims and to attract relevant research institutions and academic talents to focus on a theme of 'water-ice-air-ecosystem-human' interaction in the TPE, to reveal environmental change processes and mechanisms on the Third Pole and their influences and regional responses to global changes, especially monsoon systems, and thus to serve for enhancement of human adaptation to the changing environment and realization of human-nature harmony. Moreover, aims to reveal and quantify, from the perspectives of earth system sciences, the interactions among atmosphere, cryosphere, hydrosphere, biosphere and anthroposphere on the Third Pole and their influences on the globe in order to assess the likely future impacts of global change.

1.2 Precipitation over the Tibetan Plateau

The quantitative estimation of spatial distribution of precipitation in the Tibetan Plateau is one of the important aspects for understanding the function of water cycle processes and estimation of water resources. Unfortunately, precipitation is one of the geophysical parameters with shorter decorrelation length (Rubel, 1996, Kursinski and Mullen, 2008), and for this reason a raingauges network is generally not able to fully describe all the features of precipitation fields. In case of the Tibetan Plateau the raingauges are sparse and entire sub-regions, especially in the north West part, are not monitored at all, as will be discussed in Chapter 2. Few ground based weather radar are also present on the Plateau, operated by the China Meteorological Administration (CMA), but their coverage is strongly

limited by a number of environmental factors, such as beam blocking due to orography.

For these reason, the satellite point of view is a valuable option for precipitation monitoring over the Plateau, and several studies have been carried out to highlight precipitation characteristics.

1.2.1 Satellite precipitation estimates

One of the first studies available in literature is due to Ueno et al. (1994), who used purposely calibrated raingauges to study precipitation patterns during the 1993 monsoon season in the Tanggula basin (see Figure 1.4). The analysis of 12h cumulated precipitation showed that precipitation events are often associated to meso-scale disturbances covering the whole basin simultaneously occurring, but the amount is sporadically distributed in the basin due to the activity of convective clouds, enhanced by surrounding orography. The need of satellite observations is remarked in this work, and addressed by Ueno (1998), who implemented different visible-infrared (VIS-IR) and passive microwave (PMW) algorithms to estimate precipitation for the same 1993 monsoon season. The data of the Japanese Geostationary Meteorological Satellite (GMS) infrared channel (centered at 11 μm), re-sampled every 3 hours on a 0.25×0.25 degree resolution map, were processed following the GOES Precipitation Index (GPI) technique (Arkin and Meisner, 1987), after modification to take into account the climatological properties of precipitation over the Plateau, and estimated 12 hours cumulated precipitation by means of a regression function. The second approach for IR data was the application of the Convective-Stratiform Technique (CST) due to Adler and Negri (1988): also in this case, modifications were necessary, especially to take into account the more coarse spatial resolution of the IR data over the Plateau. Both the IR techniques are inadequate to properly address the variability in precipitation distribution in relation to Plateau scale water cycle processes, due to

the coarse resolution of GMS data. As for passive microwave, the algorithm of Ferraro and Marks, (1995) was applied to the Special Sensor Microwave Imager (SSM/I) data at 19, 22 and 85 GHz (vertical polarization).

From this analysis the distribution of diurnal differences in precipitation show a strong dependence on the major topography, as indicated by meso-scale convective activity. Thus, local circulation with orographical precipitation may be an important factor in the development of meso-scale convection. Moreover, orographical precipitation also affects the regional water balance. Because meteorological observatories are generally located in the bottom of valleys or low level areas within the Plateau, the distribution of night-time precipitation has possibly been emphasized too much as the overall feature in previous studies. Another point is the stepwise onset observed in surface observations and estimates of precipitation distribution. According to previous climatological studies, the onset of rainy season in the southeastern Plateau is earlier than that over the Indian continent. In addition, continuous heavy precipitation periods start in the central Plateau after the onset of the Indian monsoon. One of the most urgent problems highlighted by this study is the improvement of estimation algorithms. To adjust the satellite data in experimental way, two important issues must be addressed: the understanding of the structure for a unique precipitation cell in the Plateau to emphasize the algorithm concept, and the measurement of accurate aerial precipitation amounts to calibrate and validate the algorithms.

Both these issues have been addressed in 1998, during the above mentioned GAME/Tibet project, when the study of precipitation by a 3-D Doppler Radar system with a dense precipitation gauge network has been carried out, taking also advantage of the observation of the Tropical Rainfall Measuring Mission (TRMM) and Chinese Geostationary satellite FY/2.

A new algorithm for precipitation over land by deriving the optical thickness from the brightness temperature of the TRMM Microwave Imager (TMI) was developed by Fujii and Koike (2001). The effect of land surface controlled by soil moisture emissivity on radiation transfer is taken into account in this algorithm.

This means that soil moisture can be estimated at the same time in addition to precipitation. Based on a microwave radiative transfer equation, two indices, Index of Soil Wetness (ISW) and Polarization Index (PI), which remove the effect of land surface physical temperature, are introduced into the algorithm. Surface roughness effects on land surface emissivity are included by using the polarization mixing ratio and the surface roughness. As the results of the algorithm application to the GAME-Tibet meso-scale experimental field, the estimated optical thickness and soil moisture are in good agreement with the patterns of precipitation observed by the 3D Doppler radar, and the observed soil moisture at 4 cm in depth, respectively. A unique relationship between the optical thickness and the observed precipitation by rain gauges can not be seen due to the emission from precipitation layer, the temporal sampling of TMI observation, and the hydrometeor profiles. A reasonable relationship between the estimated optical thickness, and observed precipitation by rain gauges, is obtained after 10 days of longer temporal averaging.

The TMI product has also been validated in this study: daily precipitation values integrated over the Dasa Basin (see Figure 1.3), about 300 km^2 wide, where 11 raingauge stations were present. Three major shortcomings for quantitative precipitation estimation were outlined: 1) the assumption of only extinction with no emission from atmosphere and rain at 85 GHz was too simplistic; 2) the temporal sampling of TMI observations are inadequate to resolve the rapidly varying precipitation patterns; 3) the relationship between optical thickness of precipitation layer and actual rainrate depends upon the hydrometeor type, and it is unknown.

Similar approach was pursued by Yao et al., (2001), that used TMI brightness temperatures to estimate precipitation rate over the Tibetan Plateau. They used four raingauges stations data during the TIPEX IOP (coincident with GAME/Tibet IOP) to assess and calibrate the rainrate at the ground with two parameters computed as linear combinations of brightness temperature (TB): the Scattering Index (SI) and the Polarization Corrected Temperature (PCT). The SI,

firstly introduced by Grody (1991), is computed as a linear combination of TB at different frequencies and estimates the contribution to scattered radiation due to the ice crystals in atmosphere and it is expected to be positively correlated with precipitation at the ground. Usually TBs at high-frequency channels are highly affected by ice-crystal scattering, while the TBs at low-frequency channels are not. If there is no effect from ice-crystal scattering in the atmosphere (rain-free weather), the TB at a high-frequency channel (usually TB85V) can be simulated well by the TBs at low-frequency channels (e.g., TB10V, TB19V, and TB21V). When ice-crystal scattering exists (raining weather), the difference between the simulated value of TB85V by the TBs at low-frequency channels and the actual value of TB85V is used to determine the scattering intensity by ice crystals in the atmosphere. Yao et al. (2001) derived for the Plateau the following formula for SI over land:

SI = (- 65.487 - 0.1862 TB10V - 0.45456 TB19V + 1.86047 TB21V) – TB85V

where the part between brackets is the value of TB85V as estimated by lower frequency TB.

The PCT at 85 GHz, proposed by Spencer et al. (1989), is defined as

PCT(85) = 1.818 TB85V – 0.818 TB85H

and it is expected to be negatively correlated with precipitation, since raindrops tend to de-polarize the highly polarized radiation upwelling from the surface.

A detailed analysis carried on by Yao et al., (2001) shown that the TMI TB85V is negatively correlated to the surface RR on the Tibetan Plateau, similar to what it is in most other areas, but for given rainrate values, the TB85V over the Tibetan Plateau is much lower than that in most other areas of the world. Despite tremendous scattering at 85 GHz, the surface precipitation is not very intense on the Tibetan Plateau. This result is mainly because of the dry atmosphere and intense solar radiation in this area favours evaporation of the rain before it reaches the ground.

To correctly calibrate the proposed algorithm a careful match of TMI data with the surface observation data according to time and place was mandatory: the

effect of snow cover, highly variable on the Tibetan Plateau and deeply affecting precipitation retrieval, was removed before the analysis of precipitation. Five categories of surface types and rain areas on the Tibetan Plateau have been identified: dry soil, wet soil, water area, stratiform rain area, and convective rain area. The precipitation areas on the Tibetan Plateau were screened before the precipitation retrieval. Two datasets of rain-free areas and precipitation areas were formed after surface classification.

With SI, PCT(85), and their combinations as retrieval algorithms, three precipitation retrieval formulas were brought forward as follows:

$RR = 0.864 + 0.06933SI$

$RR = 39.090 - 0.13162PCT(85)$

$RR = 124.236 - 0.42906PCT(85) - 0.34318SI$

where RR is the actual rainrate in mmh^{-1}.

These relationships were applied to precipitation retrieval on the Tibetan Plateau during TIPEX/IOP 1998. It was shown that the retrieved values by means of PCT(85) algorithm was larger than the one by the SI algorithm and smaller than the one by the combined SI and PCT(85) algorithm. The comparison results demonstrate that, on the Tibetan Plateau, the SI algorithm is most suitable for low rainrates retrieval, while the PCT(85) algorithm is most suitable for moderate rainrates, and the combined SI and PCT(85) algorithm is most suitable for relatively large rain retrieval. By means of the two thresholds for TB85V, 265 and 245 K, the three rainrate retrieval formulas were applied comprehensively on the Tibetan Plateau resulting in acceptable and encouraging surface RR retrieval. The intercomparison among Yao at al. (2001) TMI algorithms and the SSM/I algorithms from the 2nd Precipitation Intercomparison Project (PIP-2) (Smith et al., 1998) demonstrates that the use of the combined SI and PCT(85), tuned exclusively for the Tibetan Plateau, is advantageous over a globally developed technique. Also, the utilization of different relationships based on TB85V works better than using a single method and is suitable for precipitation retrieval on the Tibetan Plateau.

More recently, Yin et al. (2008) used different MW and MW-IR based algorithm to infer precipitation over the Plateau at monthly scale. The aim of this work was to look in the biases among the monsoon rain amounts form the different algorithms, and to relate them to the orographic features. A total of 50 parameters describing orography (height, slope, aspect, orientation, among others) computed over a 1×1 km^2 grid are used to try to "correct" the original outputs of the different techniques, through a principal component analysis. This analysis, however, is strongly dependent on the cumulation time used for precipitation evaluation (1 month) and can be only qualitatively referred to shorter time intervals, as requested for hydrological purposes.

1.2.2 Characteristics of precipitation systems over the Tibetan Plateau

The characteristics of convective clouds over the Plateau have been studied during GAME/Tibet IOP (Uyeda et al., 2001) by means of a X-band, Doppler weather radar installed in Naqu (see Figure 1.2). Doppler velocity and radar reflectivity 3D volumes were analyzed for the 1998 monsoon pre-season and monsoon season (from May 17 to September 19). First, a strong signal of diurnal cycle has been detected by diurnal variation of echo top height and echo area: convective clouds usually form in the daytime and decay at night. The maximum echo top height for convective clouds (selected where reflectivity exceeds 10 dBZ) was found at 17 km a.s.l.. Doppler velocity field analysis showed the presence of vortices during daytime cloud developments, often in correlation with the maximum radar reflectivity, and the day maximum vorticity was larger after the monsoon onset than the pre-monsoon period. Combined analysis with radiosounding data highlighted the following processes: formation of a strong updraft by solar heating; descending of westerly wind layer at lower altitude during daytime;

increase of vertical wind shear at lower levels; tilting of the vortex axis to the vertical.

The meso-scale structure of stratified precipitation was the focus of a second radar-based study during GAME/Tibet IOP, taking also advantage of the observations of Precipitation Radar (PR) on board the TRMM satellite for two case studies (Shimizu et al., 2001). Both case studies were stratiform events occurring during evening and night: cloud clusters developed from east to west across the radar site during the day, merged and broadened during the night and dissipated in the morning. Common characteristics were: 1) presence of moist air with relative humidity exceeding 80% below 9 km a.s.l.; 2) no winds variations above 6 km a.s.l.; 3) strengthening of the meso-scale convergence below 6 km a.s.l. related to precipitation enhancement. The passage of a cold front over the radar site did not influenced at all precipitation patterns, mainly dependent on meso-scale convergence lines and divergence aloft. As for precipitation, the averaged rainrates were between 1 and 2 mm h^{-1}.

All Convective Systems (CS) originating from the Tibetan Plateau defined by the International Satellite Cloud Climatology Program (ISCCP) deep convection database (Machado and Rossow, 1993) along with associated TRMM precipitation datasets for four summers (June–August 1998–2001) have been analyzed by Li et al. (2008) to characterize their occurrence frequency, spatial distribution, development, life cycle, track, and precipitation. Three types of summer CS having their initiation over the Tibetan Plateau were identified. The first one does not move out of the plateau and dominates the CS population with 53% of frequency. The second category (25% of the total CS) propagates eastward out of the Tibetan Plateau and impacts primarily precipitation over the upper-middle segment of the Yangtze River basin. The third type is CS moving southward out of the region, which accounts for about 22% of all Tibetan CS. The last type of CS produces heavy rainfall in the southwest of China, Thailand, and even to the east of the Bay of Bengal.

The CS rainfall contribution to total precipitation is up to 76% over the central-eastern area of the Tibetan Plateau, and 30%–40% over the east-southern adjacent regions, showing important impacts of summer Tibetan CS on regional total precipitation. The two maximum initiation centers of summer Tibetan CS are located to the south of 33°N, one over the Yaluzangbu River valley to the west of 95°E and another over the Hengduan Mountain valley to the east of 95°E (see Figure 1.4). The east center is much stronger, and moves slightly northward from June to August because of the northward migration of the sun. The summer Tibetan CS has a mean life span of about 36 h. Approximately 85% of the Tibetan CS disappear within 60 h of their initiations. The southward-moving CS has the longest life cycle, while those CS staying inside the Tibetan Plateau have the shortest life cycle. The relatively stronger convection area is only about 22% of the CS coverage. Embedded convective clusters clearly show the CS initiation–decay processes and have an inhomogeneous distribution. Results also demonstrate that the more intense a Tibetan CS is, the farther away the maximum convective cluster is from its center, indicating an asymmetric development process during the CS life cycle. In addition, CS staying inside the Tibetan Plateau are generally smaller, have shorter life spans, and produce less rainfall than those moving out of this region. The differences between these two types of CSs suggest that the former is mainly forced by the surface heating while the latter is due to interactions with the surrounding atmospheric circulations during their life cycles.

Initiation of CS occur mainly in the afternoon with a maximum around 15:00 LST. The maximum frequency in mid-afternoon is about 6 times the minimum frequency at midnight, demonstrating that surface solar heating is the primary force for initiation of the summer Tibetan CS. The CS development and associated rainfall also have obvious diurnal cycles. It appears that stratiform rainfall has a distinct late night peak and mid-afternoon maximum while convective rainfall shows a major mid-afternoon peak, indicating possibly multiple mechanisms controlling the diurnal cycle of rainfall over the Tibetan

Plateau. The afternoon rainfall peak corresponds to the convection forced by the surface solar radiative heating, while the prominent peak of the CS precipitation in late night also suggests a nighttime intensification process during the development of the summer Tibetan CSs, indicating that the mechanism for the CS development is different from its initiation.

Sugimoto and Ueno (2010) carried on a similar study focused on Large Mesoscale Convective Systems (LMCS) characteristics over the Tibetan Plateau, their initiation mechanisms and their role in modifying the circulation around the eastern part of the Plateau, stretching to the east the upper tropospheric height (UH) and its fluctuations. These authors used 9 years of Meteosat 5 and Meteosat 7 infrared data remapped onto a 0.3 by 0.3 degrees grid, MCS database, following Evans and Shemo (1996) algorithm.

Results show that LMCS genesis is concentrated in the eastern and southern Tibetan Plateau and is characterized by eastward magnification of an upper tropospheric anticyclone with intensification of near-surface low pressure in the western Plateau and enhancement of a low-level longitudinal convergence line in the central Plateau. Diurnal changes of near-surface circulations were composed by eastward propagation of a cyclonic low-pressure system and associated development of low-level convergences that agreed with convective areas detected on the satellite images.

Numerical simulations (Ueno et al, 2011), carried on with the Weather Research and Forecasting model (WRF) before the day of the MCS genesis, show the role of thermally induced low pressure over the western Plateau, corresponding with a large sensible heat flux under the dry land-surface condition during daytime. The low vortex moved eastward with the intensification of the westerlies, which were induced by stronger geostrophic winds over the northern plateau under the Tibetan High development centered over southern Plateau and the approach of the synoptic trough. In the eastern plateau, low-level convergence between the northerlies and southwesterlies was caused in the rear of the migrated low vortex, and an MCS was formed, in correspondence with large convective instability over

wet surface conditions. The importance of soil moisture gradation from the southeast to the northwest for MCS formation is also confirmed by numerical sensitivity experiments: by cutting off the sensible heat flux over the western Plateau simulated the weakening of a low vortex in the west, and no MCS in the east was generated on the following day. The soil moisture gradation is primarily determined by the occurrence of precipitation in the east produced by the convective activity, including the MCSs themselves, and/or night-time orographic precipitation in the central Plateau, which could lead to a northwestward expansion of soil wetness the following morning. This points out the needs of reliable, wide scale, surface fluxes estimates as can be obtained by satellite.

Xu and Zipser (2012) studied diurnal cycle of total rainfall, precipitation features, MCS, deep convection, precipitation vertical structure, and lightning over the eastern Tibetan Plateau and eastward through China using 11 years of TRMM measurements. Results confirmed the propagation of diurnal cycles of precipitating storms, total rainfall, convection, and lightning from the foothills of the eastern Plateau downstream, which is most evident over the Sichuan basin during the pre-Mei-yu and Mei-yu seasons, absent during midsummer. In the first part of the summer the eastern Plateau foothills are dominated by nocturnal rainfall, but the early morning peak of precipitation is only in phase with deep convection, MCS, and lightning during pre-Mei-yu: most of the nocturnal precipitation is in phase with MCS and possibly contributed to by long-lived MCSs evolving from late afternoon or early night convection. Moreover, in all three seasons considered by Xu and Zipser (2012), there is strong low-level convergence in the Sichuan basin during night time with southerly winds flowing into the basin, consistent with the nocturnal maximum of rainfall, while divergence during the day is consistent with a marked rainfall minimum.

Finally, it has to be mentioned the first detailed disdrometric study of the fine structure of precipitation over the Tibetan Plateau, undergoing in the frame of CEOP-AEGIS project: three Pludix type disdrometers (Prodi et al., 2011) have been installed on the Plateau to carry on an 11 months lasting field campaign.

Preliminary results (Caracciolo et al., 2011) show the occurrence of very high precipitation peaks (around 500 mm h^{-1} for one minute), while most of the times the precipitation rate does not exceeds 10 mm h^{-1}. High rainrates occurrence very often is driven by the contribution of large drops with diameter between 2.5 and 3.0 mm: at such altitude (between 3000 and 3500 m a.s.l.) the reduced air density makes the drop speed relatively higher than at the sea level, and this reduces the breakup drop diameter to about 3.2 mm.

Chapter 2

Instruments for precipitation measure and estimate

Rainrate is a relevant parameter for geophysics and hydrology and has in general very short decorrelation length (Kursinski and Mullen, 2008), due to the high temporal and spatial variability. Different classes of instruments, based on different physical principles, are used to measure or estimate precipitation at the ground, each one with its own capabilities and drawbacks: active and passive satellite-borne sensors (at different wavelengths), ground based radar and raingauge networks.

The integrated use of weather satellite and ground observations is necessary to support water resources management in SE Asia and to clarify the interactions between land surface and the atmosphere over the Tibetan Plateau in the Asian monsoon system.

In this Chapter will be presented a review of the instruments considered in this study to estimate precipitation rate on the Tibetan Plateau.

2.1 Raingauge

The rain-gauge also called ‘pluviometer’, is the only instrument used by meteorologist and hydrologist able to measure precipitation at the ground. It collects over a set of periods of time the precipitation elements in a funnel of few square centimetres of section and measures the amount of water collected by the system over a given sampling time.

Generally, the rain gauge measures the precipitation in millimetres and precipitation amount is read in manual or automatic mode, with the reading

frequency depending on the user requirements. The instrument should be placed in an adequate area, where there are no obstructions such as buildings or trees, which could block the rain, as it is designed by World Meteorological Organization indications (WMO, 2008).

Despite raingauge is the only instrument that measures the amount of water at the ground, it has several drawbacks, and the measure is very often not representative, especially in cases of coarse networks.

The raingauges data used in this study, provided by the CMA, are of the tipping bucket type, which is the most common device used worldwide to have continuous, point-like rainrate measurement. Nevertheless, several source of uncertainty in the measurements are well known but difficult to mitigate. First, very light rainrates (2 mm h^{-1} and less) can be incorrectly estimated due to the long time it takes the rain to fill the bucket (Tokay et al., 2003). On the other side, high rainrates (above 50 mm h^{-1}) are usually underestimated due to the loss of water during the tips of the buckets (Duchon and Biddle, 2010). Drifting wind can also greatly reduce the size of the effective catching area, if rain does not fall vertically, resulting in a rainrate underestimation quantitatively assessed in about 15% for an average event (Duchon and Essenberg, 2001). Further errors occur in case of solid precipitation (snow or hail), when frozen particles are collected by the funnel but not measured by the buckets, resulting in a temporal shift of the measurements since the melting (and the measure) can take place several hours (or days, depending on the environmental conditions) after the precipitation event (Leitinger et al, 2010, Sugiura et al, 2003). All these errors can be mitigated and reduced, but in general not eliminated, by a careful maintenance of the instrument (Vuerich et al., 2009, Lanza et al., 2010).

For the present work a total of 197 raingauges over Qinghai-Tibet and surrounding regions are available from CMA (see Figure 2.1), with cumulation time of 60 minutes. Among these 197 raingauges only about 40 are over the Tibetan Plateau very irregularly distributed with very few stations in the northern and western part of the Plateau.

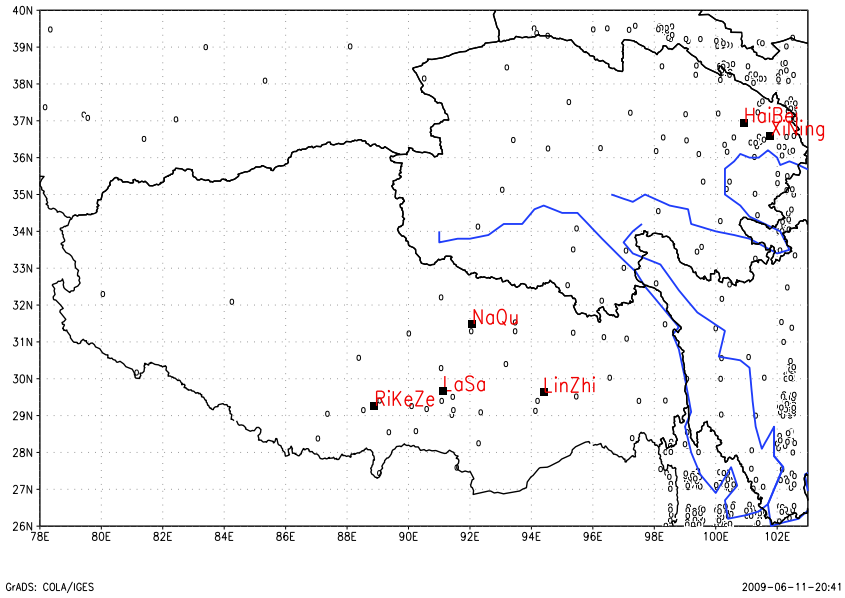

Figure 2.1 Distribution of raingauges (hollow circles), and weather radar (black squares) over the domain of this study (courtesy of CMA).

Rain-gauge measurements often are used as “ground truth” for the quality control of satellite precipitation estimates and have an important role into the calibration procedure of weather radars. Given the scarcity of data available and the low quality of the data we assessed during preliminary studies, we decided to limit the use of raingauges data in this work.

2.2 Weather Radar

The term Radar is an acronym for Radio Detection And Ranging, and in general it is widely used to remotely identify vehicles, moving objects, terrain and weather conditions. Radar is an instrument that emits radiation by the transmitter component, with a known wavelength λ and measures by the receiver component the part of the same radiation backscattered by the target.

When the waves are sent and received by two different antennas the radar is called bistatic. In the other cases when the waves are sent and received by the only one antenna the radar is called monostatic. In this case is used the switch component to connect alternatively the transmitter and the receiver to the antenna.

The first version of an anti-aircraft system for detection and localization (properly called RADAR) was developed in 1938 and then during the Second World War the radar technology was fully developed. The advancement in the radar technology led in the following years to the wavelength reduction (e.g. developing a progressive better directivity capability of the antenna) and increased the possibility to detect smaller objects. With the quality enhancements of the instruments, rain signature started to appear on radar signal: the first observation of meteorological character was recorded in 1941, while the first quantitative precipitation estimate became possible in the '60s. Then the radar Doppler VHF/UHF use for wind and turbulence observations become available around 1970 and, finally, the last generation of radars gained polarimetic capabilities, allowing the crucial feature to infer the shape of the precipitation elements and improving the rainfall estimation (Doviak and Zrnic, 1993).

Most commonly, now are in use Doppler radars which can track the relative velocity of the atmospheric targets in addition of the position and intensity.

The most widely used wavelength bands for weather radars are grouped as S-band ($\lambda = 7 \div 15cm$) for long range precipitation in USA, C-band ($\lambda = 4 \div 7cm$) for all-seasons precipitation monitoring in Europe, X-band ($\lambda = 2 \div 4cm$) for small scale basins/small rainrates monitoring. A further radar family are used in clouds and precipitation studies (especially for research, rather than for operational use) are cloud radars, allowing the detection of cloud droplets, but affected by strong attenuation phenomenon) as the Ka-, W- band radar, with λ around 8.5 mm and 3 mm, respectively.

2.2.1 Single target radar equation

The power flux density colliding with an isolated target $S_i(r,\theta,\varphi)$, where r , θ, φ, are the distance and angles target with respect of the radar position, is defined as:

$$S_i(r,\theta,\varphi) = \frac{P_T}{4\pi r^2} g_M \mid f_n(\theta,\varphi) \mid^2 l(r) \tag{2.1}$$

where P_T is the transmitted power, g_M the maximum gain, $| f_n(\theta,\varphi) |^2$ the radiation pattern and $l(r)$ the atmospheric losses.

The power received by the i-th target P_i, characterized by the backscattering cross section σ_B will be:

$$P_i(r,\theta,\varphi) = S_i(r,\theta,\varphi) \cdot \sigma_B \tag{2.2}$$

By definition, σ_B is the area intercepting an amount of incident power equal to that which radiates isotropically and corresponds to the power effectively backscattered to the radar.

$$S_i(r,\theta,\varphi) \cdot \sigma_B = S_r(r,\theta,\varphi) \cdot 4\pi r^2 \tag{2.3}$$

where S_r is the real backscattered power flux by the i-th target.

The backscattered power flux density returned by scatterer S_r, can be written as:

$$S_r(r,\theta,\varphi) = \frac{S_i(r,\theta,\varphi) \cdot \sigma_B}{4\pi r^2} \tag{2.4}$$

Then S_r will be:

$$S_r(r,\theta,\varphi) = \frac{\sigma_B}{4\pi r^2}\frac{P_T}{4\pi r^2} g_M \mid f_n(\theta,\varphi)\mid^2 l^2(r) \tag{2.5}$$

The backscattered power reached to the radar's antenna is defined as:

$$P_r(r,\theta,\varphi) = A_e(\lambda,\theta,\varphi)S_r(r,\theta,\varphi) \tag{2.6}$$

where A_e is the antenna's effective aperture defined as:

$$A_e = \frac{g(\theta,\varphi)\lambda^2}{4\pi} \tag{2.7}$$

where $g(\theta,\varphi)$ is the antenna gain. Assembling into a constant C_1 all radar fixed parameters, the single scattering radar equation is given by:

$$P_r(r,\theta,\varphi) = P_T C_1 l^2(r)\frac{\sigma_B}{r^4} \tag{2.8}$$

and C_1 is given by :

$$C_1 = \frac{g^2_M}{(4\pi)^3} \mid f_n(\theta,\varphi)\mid^2 \lambda^2 \tag{2.9}$$

Since $\sigma_B \propto \lambda^{-2}$, for a given received power signal, the radar with smaller λ measure a larger σ_B, and it is more sensitive to small objects, for example cloud droplet.

The size of radar antenna must be such as to obtain a narrow half power beamwidth defined as :

$$\beta_{1/2} \approx 70\frac{\lambda}{D} \tag{2.10}$$

where D is the diameter of radar's antenna.

2.2.2 Multiple target radar equation

Each radar cell volume usually contains a variety of meteorological objects and the radar instrument receives the backscattered signal from the objects contained in a radar cell volume.

The received signal will be the contribution of all the received signals from the targets in the cell volume V and the total received power is related with the total backscatter cross section such as:

$$P_{total} = \sum_{V} P_{\sin g.t\arg et} \tag{2.11}$$

$$P_{total} \propto \sigma_{Btotal} \tag{2.12}$$

where the total backscatter cross section is written as:

$$\sigma_{Btotal} = \sum_{V} \sigma_B = V\left(\sum_{V} \frac{\sigma_B}{V}\right) \tag{2.13}$$

The volume averaged backscattered cross section η is called *reflectivity* and is written as:

$$\eta = \sum_{V} \frac{\sigma_B}{V} \tag{2.14}$$

From eq 2.13 and 2.14 σ_{Btotal} can be written as:

$$\sigma_{Btotal} = V\eta \tag{2.15}$$

Assuming an uniform distribution targets and replacing fixed parameters with a constant C_2 we get the multiple target radar equation written as:

$$\overline{P_r} = P_T C_2 l^2(r) \frac{\eta}{r^2} \tag{2.16}$$

According to the multiple target radar equation the signal received from multiple scatterers decreases as r^{-2}, while the signal from a single scatter decreases as r^{-4}.

2.2.3 The radar equation

The energy received by the radar's antenna is characterized by the radar reflectivity factor Z (mentioned as reflectivity) defined as:

$$Z = \sum_{vol} n_i D_i^6 \tag{2.17}$$

where: n_i is the number of raindrops in a volume of the radar beam and D_i is the diameter of the n_i - raindrops in the volume of the radar beam.

For a range from D to $D+dD$ the eq 2.17 becomes:

$$Z = \int_0^\infty N(D,r) D^6 dD \tag{2.18}$$

where $N(D)$ is the Drop Size Distribution, so that $N(D)dD$ is the number of raindrops with diameter from D to $D+dD$ per unit volume. Z-unit is [$mm^6 m^{-3}$] or [dBZ]. Assembling all radar fixed parameter into a constant C the radar equation 2.16 becomes:

$$\overline{P_r} = P_T C l^2(r) \frac{Z}{r^2} \tag{2.19}$$

The relation between rainfall rates and reflected energy from the raindrops establish the (R) rain intensity estimation. This Z-R relationship is generally defined as:

$$Z = AR^b \tag{2.20}$$

where R is rain intensity [mm/h], A and b are defined as empirically values dependent on radar parameters, geographic position, rainfall type etc.

A wide variety of A and b valued can be found in the literature, for different regions and rainfall characteristics. Among the first derived relationships we can mention: for stratiform rain $Z = 200R^{1.6}$ (Marshall and Palmer, 1948), for orographic rain $Z = 31R^{1.71}$, for thunderstorm rain $Z = 486R^{1.37}$, and $Z = 250R^{1.2}$ for tropical rain.

2.2.4 Observation radar system on the Tibetan Plateau

In Tibetan Plateau and in Qinghai Province, are installed six C band Doppler radars, located in Lhasa, Naqu, Rikeze, Linzhi (Tibet Autonomous Region) and Xining and Haibei (Qinghai Province) as shown in Figure 2.1. These radars form two small networks, used by CMA for the summertime precipitation monitoring of the two regions. Their usual operational mode performs volumetric scans every 6 minutes every day during the summer, while no operations are carried on outside the monsoon season. All the pre-processing of the radar data have been carried out at CMA, and we will just summarize the algorithms used.

The radar operates in C band with Doppler capabilities, with beam width of 0.95°, gate depth of 250m and performs a volume scan with 14 or 9 elevation angles (VCP-Volume Coverage Patterns on vertical height sampling). Figure 2.2 presents VCP scans with 14 elevation angles.

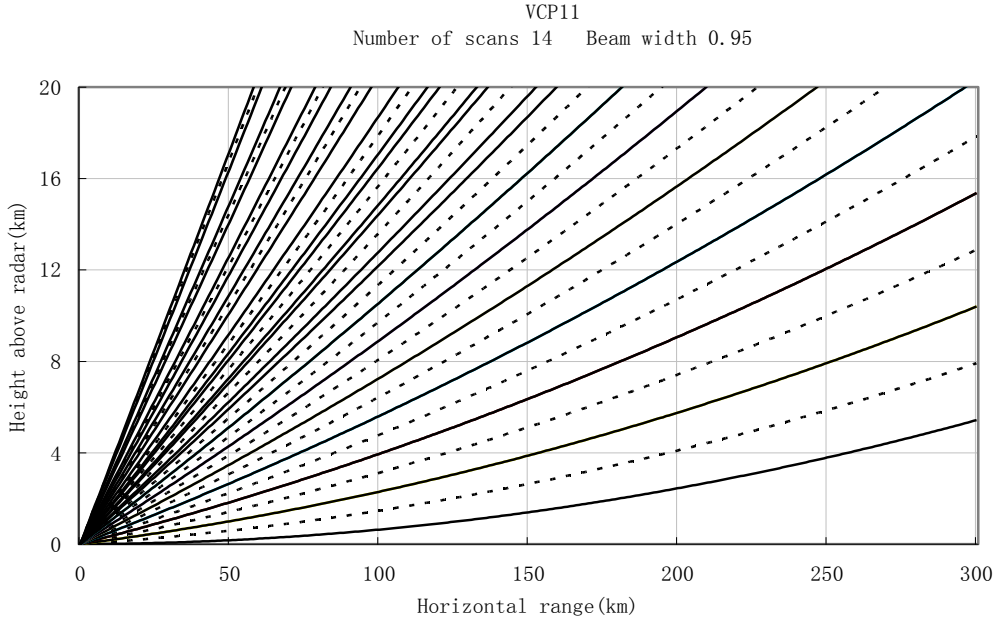

Figure 2.2 Representation of the radar beams in case of 14 elevations scan.

Radar rain observation and quantitative estimates on the Tibetan Plateau reports all the known radar errors classically recognized in any operational weather radar

with some addition and enhancements especially due to orography. The CMA Group that provided the data within the CEOP-AEGIS Project used in this work performed a variety of pre-processing to the raw data in order to minimize these errors. A brief review of these methods is presented.

2.2.4.1 Beam blocking and hybrid scan

Weather radars operating in complex orographic areas usually suffer from partial or total beam blockage caused by surrounding mountains. This shielding effect may seriously restrict the use of the lowest antenna elevation angles which provide the most useful information for rainfall rate estimation at ground level. This problem is particularly severe over the Tibetan Plateau and Qinghai, where steep orography is unavoidably present very close to radar sites.

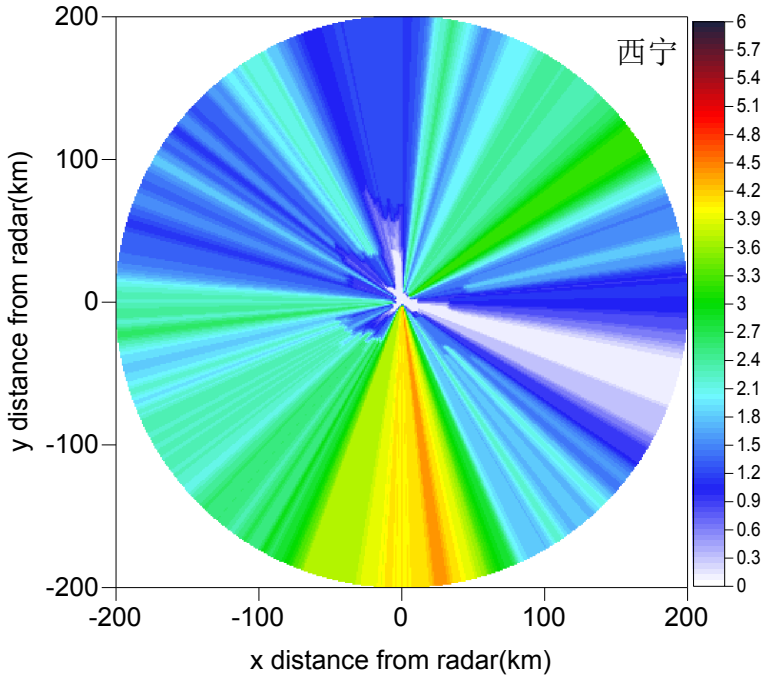

Figure 2.3 The hybrid scan for C band radar in Xining, Qinghai Province. Colors refer to the lowest elevation unaffected by blocking.

To minimize and manage this problem, hybrid scans are constructed starting from the scanned volumes: high resolution Digital Elevation Model (DEM) data, radar beam pattern (Gaussian beam approximation), and radar beam propagation path (assuming radar beams propagate under standard atmospheric refraction conditions) are used.

The hybrid scan is obtained collecting for each radar beam and gate the data of the lowest elevation angle with no mountain blockage for echo azimuth. Figure 2.3 shows the hybrid scan for the Xining radar. We can see that the radar beam is severely blocked by the mountains and for several azimuth the beam is blocked for elevation lower than about 3.5° and higher.

In Figure 2.4 an example of hybrid scan processing applied to the Xining radar: the elevations at 0.5° (2.4b), 1.4° (2.4c), 2.3° (2.4d), 3.4° (2.4e), 4.3° (2.4f) are used to construct the hybrid scan image reported in Figure 2.4a.

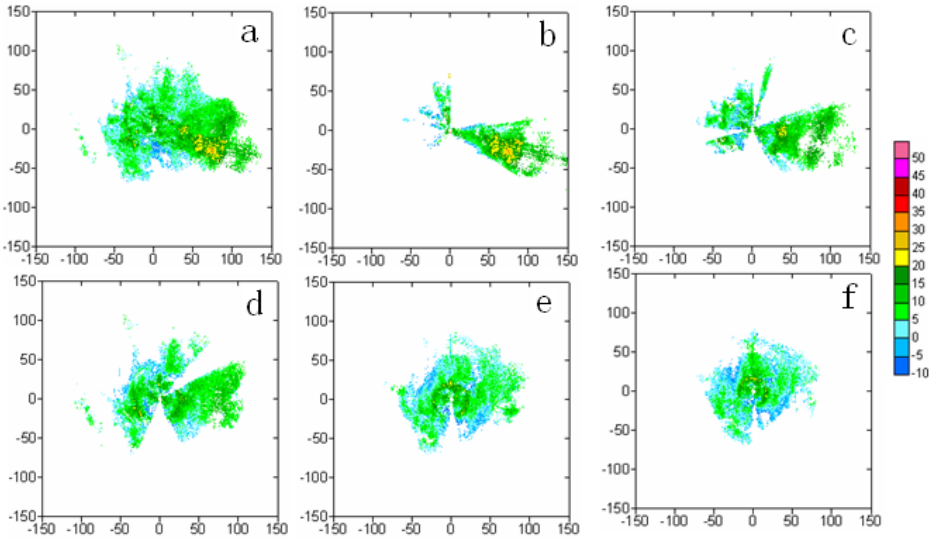

Figure 2.4. Reflectivity at hybrid Scan (a) and original PPI scans at 0.5° (b), 1.4 ° (c), 2.3° (d), 3.4° (e), 4.3° (f) elevations for the Xining radar.

2.2.4.2 Mosaic

The mosaic approach is necessary, in case of radar networks, to calculate a final reflectivity value for grid cells over sampled by more than one radar bins, and thus to merge and mutually correct multiple radar observations. Three approaches have been utilized by CMA for the Tibet-Qinghai radar preprocessing: Nearest-neighbour reflectivity, maximum reflectivity and distance weighted means.

(a) ***Nearest-neighbour mosaic approach***

In this approach, the closest radar is assigned to the grid cell. The nearest neighbour method does not involve any smoothing when creating a mosaic from multiple radars.

(b) ***Maximum reflectivity***

This method uses the maximum reflectivity value among the multiple observations that cover the same grid cell. This method does not involve smoothing and it retains the highest reflectivity intensities in the data fields.

(c) ***Distance weighted means***

The mosaic method considers a weighted mean. The weight is based on the distance between an individual grid cell and the radar location. In this implementations are considered Cressman and exponential weighting function.

Results have shown the distance- exponential-weighted mean scheme provided a spatially consistent reflectivity mosaics while retaining the magnitude of the observations from the close radar, and thus this approach has been used for mosaic extraction.

In Figure 2.5 are shown the Constant Altitude Plan Parallel Indicator (CAPPI) lowest plot of the Haibei (left), Xining (center) and the mosaic of the two (right).

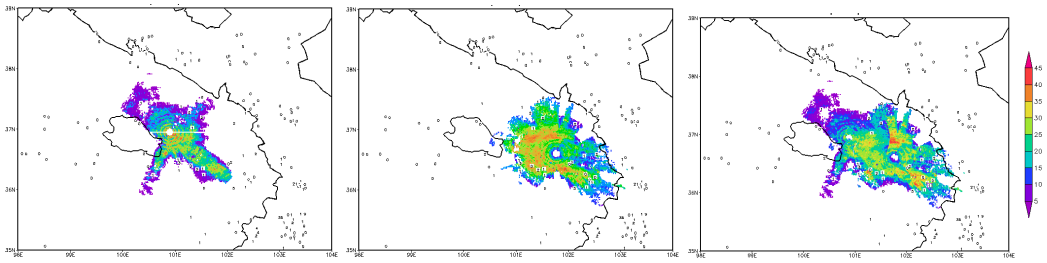

Figure 2.5 CAPPI images for the radar in Haibei (left), in Xining (center), and the mosaic of the two (right)

2.2.4.3 Radar data quality control

For the QC (Quality Control) of radar data is used a fuzzy logic algorithm, to detect the anomalous propagation (AP) ground clutter. For the classification this algorithm uses various derived fields, known as *features*, as input, scales them to a common reference frame by use of a *membership function*, and then computes a weighted sum of the resultant *interest* fields. After application of a threshold, the final output product contain the location of the AP ground clutter. In the Figure 2.6 is shown the general scheme of AP clutter detection algorithm.

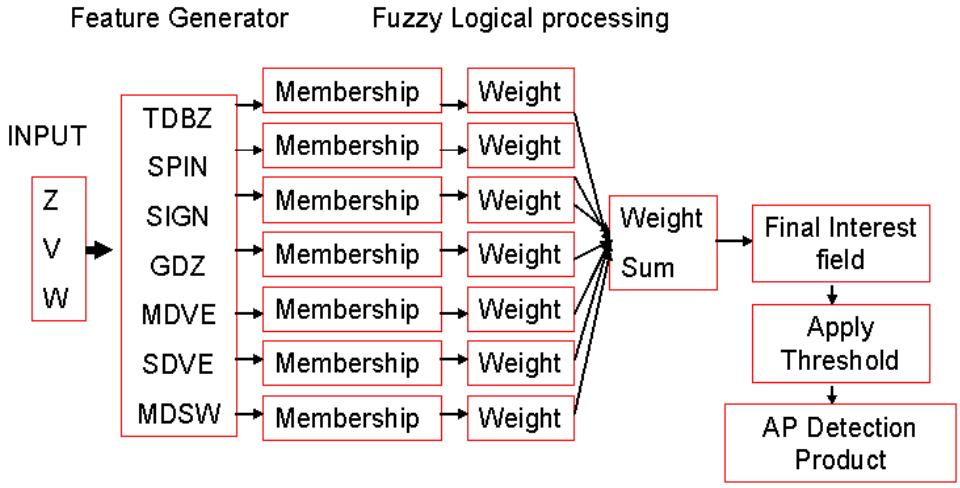

Figure 2.6 The general schematics of AP clutter detection algorithm.

The reflectivity, radial velocity and spectrum width in polar coordinate are input into the *feature generator* for features calculation. The features used in the algorithm includes: texture of the reflectivity (TdBZ), the vertical difference of the reflectivity (GDBZ) between two elevation angles, the median radial velocity (MVE) and spectrum width (MSW), the standard deviation of radial velocity (SDEV), Percent of all of possible differences, that exceed the minimum difference threshold (SPIN) and mean sign of reflectivity change along range (SIGN).

The MDVE and MDSW are calculated by median filtering along the range for 7 gates. Three features from reflectivity, two features from velocity, one from spectrum width and one from vertical structure of reflectivity are used to detect AP clutter. The seven features calculated gate by gate are input to the memberships to calculate the interests, respectively. The difference between this algorithm and other methods proposed lies in the fact that the median velocity and spectrum are used, instead of mean velocity and spectrum, considering the velocity folding and noise of the data. All of memberships are given a equal weight when calculating the interest field of AP clutter, and 0.5 is the threshold to detect the AP clutter. In Figure 2.7 an example of application of the QC algorithm to a radar operated by CMA.

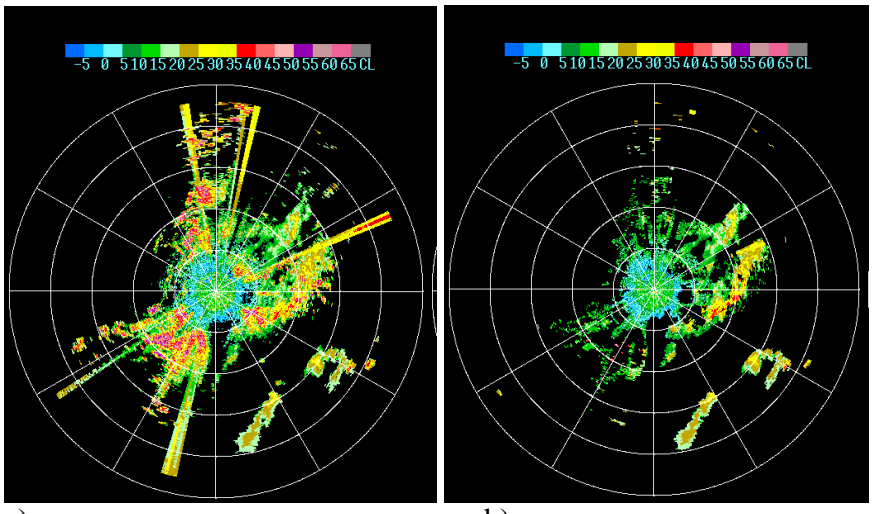

a) b)

Figure 2.7 The lowest PPI original data a) and after QC b)

2.2.4.4. QPE

The QPE (Qualified Precipitation Estimation) Algorithm is based on 3D mosaic pre-processed data. The CAPPI of 3D mosaic reflectivity between 2-5 km (MSL) is chosen to calculate the precipitation. The altitude of CAPPI depends on the domain for QPE, the blockage of radar beam, the precipitation system. The horizontal and vertical resolution of 3D grid data are 2 km and 0.5 km, respectively. Because of the mountain blockage radars beam, the composite reflectivity is used. To filter the reflectivity data two thresholds are used. Isolated sample bins are replaced with a valid reflectivity. Isolated bins are defined as grids cells with reflectivity that exceed a certain threshold (15 dB*Z*) and for which no more than one of the eight surrounding neighbors is also above that same threshold.

A second maximum reflectivity threshold parameter (65 dB*Z*) is used to quality control the extremely large outliers typically associated with residual ground clutter or anomalous propagation that have not previously been removed. If a grid cell has a reflectivity that exceeds this threshold, it is replaced with an average of surrounding values threshold, or assigned a very small value (7 dB*Z*). However, is occurred additionally quality control to remove all residual clutter or anomalous propagation.

The standard *Z–R* power law relationship derived from the empirical relationship in this study is defined as:

$$Z = 300R^{1.4} \qquad (2.21)$$

The *Z–R* parameter settings are designed to be adjustable at each site.

The reflectivity stronger than 55 dBZ are considered as hail cores of thunderstorms. The “hail cap” threshold, an adaptable parameter representing the maximum expected instantaneous, rain rate, has typical values ranging from about 75 mm h^{-1} to about 150 mm h^{-1} except in highly unusual events.

Real-time rain gauge data can be used to adjust the radar rainfall estimates in the algorithm. Optimal Interpolation (OI) analysis is used in this QPE. The advantage of OI is its simplicity of implementation and its relatively small cost if the right assumptions can be made on the observation selection. High resolution (6 min) raingauges data have been used to adjust QPE by correcting the Z-R relationship.

2.3 Satellite systems for precipitation observations over the Tibetan Plateau

Weather Satellites have an important role in the rainfall estimation, for the precipitation pattern monitoring, especially in mountain regions where the data quality of the radars and some sparse rain gauges, is very poor. Satellite derived precipitation estimates at high temporal and spatial resolution are used within forecasting systems in meteo- and hydrological services.

After the first weather satellite, Television InfraRed Observing System (TIROS) put in low earth orbit by U.S. Government in 1960 a series of satellites are launched by U.S., Soviet Union, Japan, European Space Agency, India and China, on different orbits and equipped with a variety of sensors.

There are two primary type weather satellite, depending on the orbit type:

- a geostationary satellite is positioned at a distance from the earth surface d=35,405 km, and located over the equator. It orbits around the earth at the same speed as the earth rotates around its axis. The satellite remains stationary above the same point on the earth, and is able to continuously monitor the same large area.
- a polar-orbiting satellite flies around the earth over both north and south pole. This type of satellites is positioned at an altitude of approximately 800 km and it is often referred as Low Earth Orbit (LEO) satellite, moves

more rapidly and relay more detailed observation than a geostationary satellite but the area monitoring is much smaller.

Other distinction among the satellite systems is about the sensors. If the sensor only receives and measures radiation coming from the earth system is called passive sensor, in case of the system emits radiation and measures the power returned to the sensor after interaction with earth system (such as the radar), the sensor is called active.

According to the satellite's sensor instrument, it is possible to receive data in a wide range of frequencies of the electromagnetic spectrum, to have a variety of data with different properties, and carrying different information on the Earth system.

2.3.1 Resources for multisensor precipitation observation

A multi-sensor satellite approach to derive precipitation estimates is demonstrated to be an effective tool in all the efforts to understand the variability of the atmospheric moist processes over a large space and time scales and improving climatological global water cycle studies (Kidd and Levizzani, 2011 for the most recent development, Levizzani et al., 2007 for wider reference).

The use of VIS/IR part of spectrum offers the possibility of performing precipitation monitoring with relatively high spatial resolution and, when the sensor is on board a GEO platform, also on a global scale and with high temporal resolution, which is the main advantage of VIS/IR systems. The disadvantage of using VIS/IR sensors is that the radiation originates from the top cloud layers and does not directly carry information from rain layers at the bottom of the cloud. Looking from space in the VIS region, the cloud top layers (few hundreds of meters) reflect most of the incident solar radiation, and no information from lower parts of the cloud (where precipitation occurs) can reach the satellite. On the same

token, IR radiation emerging from the warm earth surface, is absorbed by the lowest cloud layer, who emits radiation, following the Planck Law) at lower temperature: the radiation travelling upward is absorbed and emitted by each cloud layer, progressively cooling with height. The IR sensor, in case of cloudy scene, receives the radiation emitted by the highest (and colder) cloud layer, while the precipitation layers are hidden. Given these premises, the rainfall estimation in the VIS-IR spectrum is necessarily of indirect nature.

In the microwave part of the spectrum the interaction between hydrometeors and radiation is more detailed. For the longer wavelengths ($\lambda \geq 1$ cm) the small cloud particles ($r < 1$ mm) weakly scatter radiation, following Rayleigh approximation, while raindrops or hailstones interact strongly with the incident radiation field. For higher frequencies (e.g. 85 GHz) all cloud and rain particles are strong scatterers. As for the absorption properties of water and ice, the imaginary part of the refraction index of water is about 10^3 times larger than the one of ice, indicating water drops as more effective absorbers as compared with ice particles.

The following properties can summarized: 1) ice essentially does not absorbs microwave radiation, only scatters, 2) drops both absorb and scatter, but absorption dominates and 3) scattering and absorption both increase with frequency and rain rate, however scattering by ice increases much more rapidly with frequency than scattering by liquid. In the first part of the microwave spectrum (10 to 22 GHz) absorption is the primary mechanism affecting the transfer of microwave radiation through a cloudy atmosphere; scattering does occur but is negligible and the ice crystals and aggregates above the rain layer are nearly transparent. Between 22 and 60 GHz both scattering and absorption are important, while above 60 GHz scattering dominates: radiometer senses the ice and not the rain below.

The use of active microwave sensors, such as the TRMM Precipitation Radar (PR, launched in 1997 and still working) and the Cloudsat Cloud Profiling Radar (CPR, launched in 2006) have in the last years greatly improved the knowledge of precipitation systems over areas not covered by surface radars. Moreover, these

active sensors provided unprecedented tools for precipitation direct observations from space. However, their direct use as space-borne precipitation estimation for real time use is prevented by their poor coverage, given the LEO orbits of the two spacecrafts and the narrow swaths (1 pixel for CPR).
For the present work it was of interest a full exploration of the satellite approach and for the precipitation estimation over the Tibetan Plateau, and in the next sections the space-borne instruments used in this study are presented.

2.3.2 Satellite instruments for precipitation estimation over the Tibetan Plateau

In this Section is present a review of the operational satellites and their sensors for the possible application for precipitation estimations over the Tibetan Plateau. It has to be mentioned that the only mission specifically designed for precipitation is the TRMM, carrying a Precipitation Radar (TRMM-PR), while other sensors provide data that can indirectly be related to precipitation at the ground.

2.3.2.1 Aqua and Terra satellite

Terra satellite was launched by the Earth Observing System (EOS), in December 1999 and was followed by the 'sister' Aqua satellite, launched on May 2002.
The Aqua satellite operate in near-polar and sun-synchronous orbit, at an altitude of 705 km, with an inclination of 98.2°. Aqua orbits the Earth every 98.8 min, moving north across the equator at 1:30 P.M. local time, and south across the equator at 1:30 A.M. local time.
The TERRA satellite in contrast of AQUA Satellite, moves south across the equator at 10:30A.M. local time and north across the equator at 10:30 P.M. local time.

Formally, TERRA and AQUA satellites were named EOS-AM, and EOS-PM, respectively. Approximately are 14 consecutive passes over the equator on a day. In the Figure 2.8 is shown the schematic of the Aqua orbits, for nine consecutive passes over the equator.

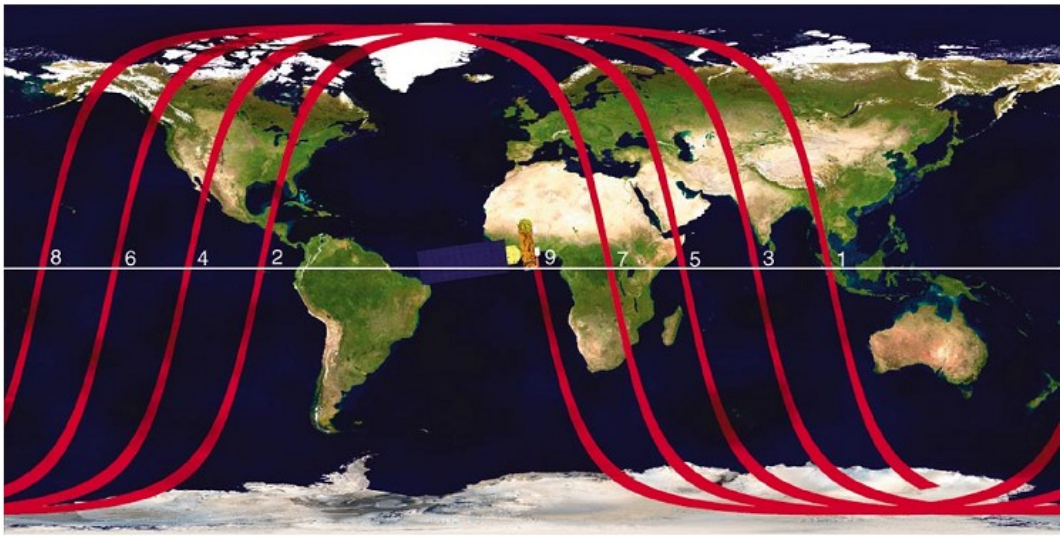

Figure 2.8. Schematic of the Aqua orbits, for nine consecutive passes over the equator. (Schematic by J.Allen)

The Aqua satellite carries six distinct earth observing instruments: the Atmospheric Infrared Sounder (AIRS), the Advanced Microwave Sounding Unit (AMSU), the Humidity Sounder for Brazil (HSB), the Advanced Microwave Scanning Radiometer for EOS (AMSR-E), the Moderate Resolution Imaging Spectroradiometer (MODIS) and Cloud and the Earth's Radiant Energy System (CERES) (Parkinson, 2003).
The three instruments AIRS, the AMSU and the HSB are cross-track scanners obtaining information at multiple levels of the atmosphere.

AIRS is a high-spectral-resolution sounder, with 2378 channels measuring infrared radiations in a spectrum range of 3.7-15.4 μm and 4 channels measuring visible and near-infrared radiation in the range of 0.4-0.94 μm. Its primary

purpose is to obtain atmospheric temperature and humidity from surfaces upward to an altitude of 40 km, and to provide substantial improvements especially in the temperature measurements.
The primary purpose of the 4 channels VIS and NIR measurements is to provide diagnostic support through higher spatial resolution, for the Infrared retrievals. The secondary purpose is on the searching products for the surface solar radiation flux and for the height of low-level clouds. Horizontally spatial resolution data for the IR radiation measurements is 13.5 km at nadir, and for the visible and near infrared measurement is 2.3 km at nadir. Vertically spatial resolution is 1 km layers in the troposphere and 3-5 km layers in the stratosphere.

AMSU is a 15 channels sounders consisting in two physically separated units called AMSU-A1 and AMSU-A2. Twelve channels measuring radiation in a frequency range between 50 GHz and 60 GHz, are used for temperature sounding and the other three channels measuring radiation at frequencies of 23.8 GHz, 31.4 GHz and 89 GHz, used predominantly for water vapour and precipitation measurements. The AMSU horizontal spatial resolution varies from 16 to 40.5 km at nadir, depending on the frequency.

HSB is a microwave humidity sounder, with a purpose to determine humidity, cloud liquid water and precipitation. HSB has four channels, one measuring radiation at 150GHz and the other three channels measuring radiation bands on strong water vapor absorption line at 183.31 GHz. The horizontal spatial resolution is 13.5 km at nadir.

CERES (Clouds and the Earth's Radiant Energy System) is a broadband scanning radiometer with three channels, one in the wavelength band 0.3-0.5 μm measuring solar radiation reflected from the earth or atmosphere, one in the wavelength band 8-12 μm (atmospheric window) measuring top of the

atmosphere radiation emitted and one measuring top of the atmosphere total reflected and emitted radiative energy, in a wavelength band from 0.3 μm to grater than 100 μm. The CERES horizontal spatial resolution is 20 km at nadir.

MODIS (Moderate Resolution Imaging Spectroradiometer) is a cross-track scanning radiometer operating on both the TERRA and AQUA satellite. The instruments capture data in 36 spectral wavelength bands ranging from 0.4 μm to 14.4 μm.

MODIS instrument is designed to generate a wide variety of ocean, land and atmosphere products, including photosynthetically active radiation, chlorophyll fluorescence, organic matter concentrations, sea surface temperature and emissivity, snow cover, cloud top properties, cloud optical thickness and microphysical properties, aerosol size distribution, total ozone, total precipitable water, temperature and water vapor profiles, and others.

Spatial resolution data is 250km for 2 bands, 500 m for 5 bands and 1 km for 29 bands, which is the finest spatial resolution data of the AQUA instruments.

In the Table 2.1 are shown the 36 channels wavelength range bands, spatial resolution data and primary using of each channels data measurements.

Table 2.1 MODIS channels specifications

Band	Wavelength (nm)	Resolution (m)	Primary Use
1	620–670	250	Land/Cloud/Aerosols Boundaries
2	841–876	250	
3	459–479	500	Land/Cloud/Aerosols Properties
4	545–565	500	
5	1230–1250	500	
6	1628–1652	500	
7	2105–2155	500	
8	405–420	1000	OceanColor/ Phytoplankton/ Biogeochemistry
9	438–448	1000	
10	483–493	1000	
11	526–536	1000	
12	546–556	1000	
13	662–672	1000	
14	673–683	1000	
15	743–753	1000	
16	862–877	1000	
17	890–920	1000	Atmospheric Water Vapor
18	931–941	1000	
19	915–965	1000	
Band	Wavelength (μm)	Resolution (m)	Primary Use
20	3.660–3.840	1000	Surface/Cloud Temperature
21	3.929–3.989	1000	
22	3.929–3.989	1000	
23	4.020–4.080	1000	
24	4.433–4.498	1000	Atmospheric Temperature
25	4.482–4.549	1000	
26	1.360–1.390	1000	CirrusClouds Water Vapor
27	6.535–6.895	1000	
28	7.175–7.475	1000	
29	8.400–8.700	1000	Cloud Properties
30	9.580–9.880	1000	Ozone
31	10.780–11.280	1000	Surface/Cloud Temperature
32	11.770–12.270	1000	
33	13.185–13.485	1000	Cloud Top Altitude
34	13.485–13.785	1000	
35	13.785–14.085	1000	
36	14.085–14.385	1000	

AMSR-E (Advanced Microwave Scanning Radiometer for EOS) is a twelve-channel conically scanning passive microwave radiometer, with vertically and horizontally polarized measurements at six-frequencies of 6.925, 10.65, 18.7 23.8, 36.5 and 89 GHz. The Earth-emitted microwave radiation is collected by a parabolic reflector 1.6 meters in diameter that scans across the Earth along an imaginary conical surface, maintaining a constant Earth incidence angle of 55° and providing a swath width array of six feedhorns. The radiation collected by the feedhorns is then amplified by 14 separate total-power radiometers. For the 89.Ghz channels are two feedhorns in order to achive 5 km along-track spacing.

The ASMR-E spatial resolution varies from approximately 5 km for the 89.GHz channels to 56 km for the 6.9GHz channels. Observation will be produced at spatial resolution of 10 km and 5 km, the highest resolution over the earlier satellite passive microwave instruments.

Brightness temperature derived from the Level 2A stage of processing is a result of a linear combination of actual observations, and will be defined as **'**constructed observation' or an 'effective observation'. The data products from the AMSR-E are rainfall areal measurements, total column water vapor and total column cloud water, sea surface temperature/wind speed, sea ice temperature, snow depth on land, surface soil moisture, etc.

The Satellite data products are being analyzed for their accuracy through numerous validation efforts. In Figure 2.8 is shown a schematic wavelength and frequency ranges of measurement from each AQUA observing instruments, allowing scientists to monitor many earth and atmosphere variables.

The processed data from Aqua are available form NASA's Distributed Active Archive Center (DAAC).

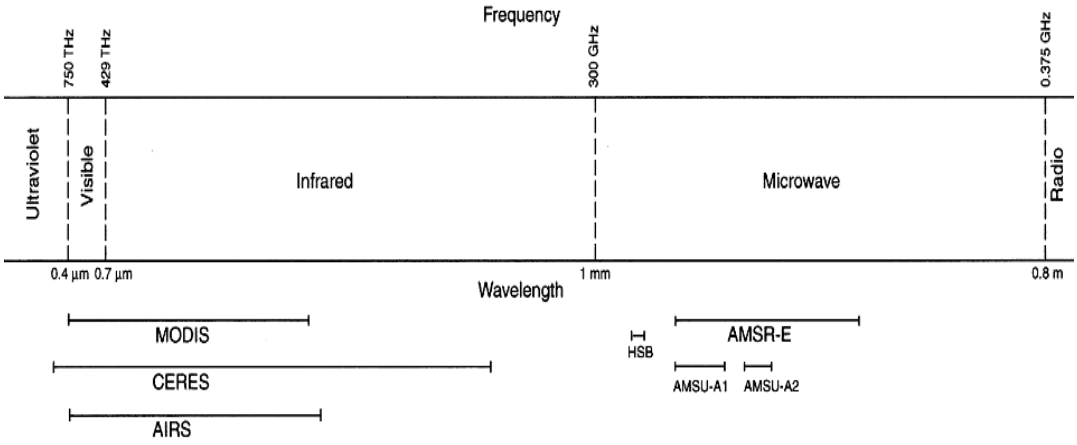

Figure 2.8 Schematic wavelength and frequency ranges of measurement from each AQUA' observing instruments.

2.3.2.2 DMSP satellite

DMSP (Defence Meteorological Satellite Program) is a polar orbiting sun synchronous satellites of the US Department of Defence with a numerous sensor aboard. Can mention OLS (Operational Linescan System) a visible and infrared sensor, which produce imagery in two different resolution: SMOOTH and FINE. The DMSP satellite operate at an altitude of 833 km, with an inclination of 98.8° causing missing the polar caps. DMSP orbits the Earth every 102 min, approximately 14 orbits every day and pass over a given point on the earth at the same local time each day. The DMSP satellites have three microwave sensors: SSM/T or SSM/T-1, SSM/T-2 and SSM/I or SSMI. SSM/T-1 (Passive Microwave Temperature Sounder) and SSM/T-2 (Passive Microwave Temperature Sounder-Water Vapor) are primarily focused on the retrieval of temperatures in the upper troposphere. SSM/I (Special Sensor Microwave/Imager) sensor is focused on the retrieval of microwave energy emitted from the Earth's surface .

The passive microwave SSM/I sensor has a broadband, corrugated, parabolic reflector scanning mechanism. The SSM/I instrument measures the Earth's radiation at four frequencies 19.35 GHz, 22.235 GHz, 37.0 GHz and 85.5 GHz. Except the 22 GHz frequency, at each frequency operate two separated channels detecting vertically and horizontally polarized microwave energy.

Thus SSM/I has seven operational channels. Spatial resolution data is 50 km at 19 GHz and 22 GHz frequencies, 25 km at 37 GHz frequency and 13 km at 85 GHz frequency. The SSM/I channels measure the brightness temperature directly related with the real temperature by the equation $T_B = eT$, where e is the emissivity of the Earth's surface, varying from 0 to 1. In Fig. 2.9 is shown the profiling absorption of a atmosphere accomplished in water vapour and oxygen absorption bands. At 22 GHz region, is one of the maximum absorption of microwave energy, caused by water vapour in the atmosphere. Thus the 22 GHz channel was chosen to provide water vapour estimations in the atmosphere.

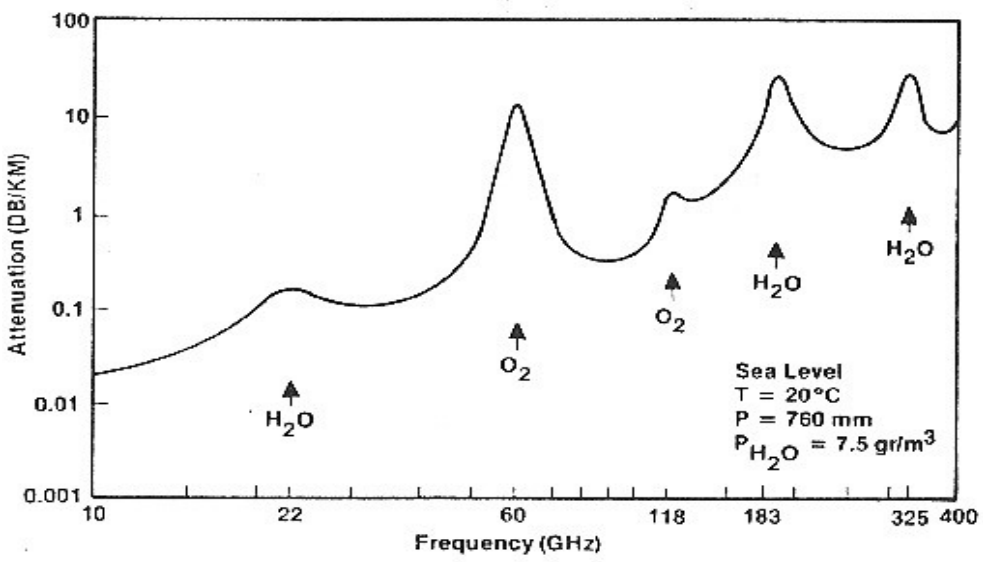

Figure 2.9 profiling absorption of a atmosphere accomplished in water vapour and oxygen absorption bands.

The emissions at 22 GHz coming from the atmospheric water vapour usually is randomly polarized and does not have a preferred sense of polarization. For this reason at 22 GHz operates only one vertical channel on the SSM/I. At 85 GHz frequency channels radiation carries information that can be used for precipitation estimates, since at the wavelength of 3.5 mm, the radiation is close to the size of water droplet and ice particles, given the scattering properties of raindrops and ice particles in the atmosphere. The 19 GHz channels are sensitive to the characteristic of Earth's surface, such as land surface moisture, land type, ocean surface roughness, etc. Surface winds can be derived from 19V GHz, 22V GHz, and 37 GHz channels, studying the ocean surface roughness.

The **SSMI/S** (Special Sensor Microwave Imager/Sounder) sensor is a passive conically scanning microwave radiometer that combines and extends the current imaging and sounding capabilities of three previously separate DMSP microwave sensors: the SSM/T-1 temperature sounder, the SSMI/T- 2 moisture sounder, and the SSMI. The SSMIS instrument measures microwave energy at 24 discrete frequencies from 19 to 183 GHz with a swath width of 1700 km.

2.3.2.3 TRMM satellite

The TRMM is the first mission dedicated to observing and understanding tropical/subtropical rainfall and how this rainfall affect the global climate. TRMM is a joint project between US and Japan (Japan Aerospace Exploration Agency – JAXA). TRMM operates in circular not sun-synchronous orbit, with and inclination of 35° to equator at an altitude approximately of 402 km. The TRMM is part of NASA's project, effort to study the Earth as a global environmental system. The primary instruments aboard the TRMM for measuring precipitation are the PR, the TMI and the Visible and Infrared Scanner (VIRS). Aboard the TRMM are the Lighting Imaging Sensor (LIS) and the CERES.

In the Table 2.2 are shown the instrument specifications of TRMM Microwave Imager (TMI), Visible and Infrared Scanner (VIRS) and PR.

The PR is the first space-borne rain radar instrument, designed to provide three dimensional maps of the rain during a brief time. The horizontal resolution of Precipitation Radar data is about 5 km with a swath width of 250 km.

The Precipitation Radar is able to detect light rain-rates down to 0.7 mmh^{-1}. The most important features of PR is the ability to provide vertical profiles of the rain and snow from surface up to a 20 km of altitude. Although, it has the ability to separate out rain echoes fort vertical sample size of 250 m when looking straight down. The measurement of rain over land, where passive microwave has difficulty, is a unique features of PR. The Precipitation Radar is the most innovative instrument aboard the TRMM satellite.

Table 2.2 TRMM instrument specifications

Instrument	**Frequencies**	**Resolution**	**Scanning**	**Swath W**
Microwave Radiometer	10.7, 19.3, 21.3 37.0, 85.5 (GHZ) Dual polarized expect for 21.3	11 km X 8 km field of view at 37 GHz	Conically scanning	880 km
Visible and Infrared Radiometer	0.63, 1.6, 3.75 10.8 12 (μm)	2.5 km	Cross-track scanning	830 km
Precipitation Radar	13.8 (GHZ)	5 km footpri Vertic 250 m	Cross-track scanning	250 km

2.3.2.4 CLOUDSAT satellite

Cloudsat is a NASA Earth Science System Pathfinder (ESSP) mission and operates in sun-synchronous orbit, at an altitude of 705 km. The Cloudsat satellite mission is to provide the first global survey of the entire cloud vertical profiles

structure and physical characteristics. The 94 GHz nadir-looking radar instrument (CPR) onboard the Cloudsat satellite, has a great sensitivity providing detailed information of the water droplet and ice crystals inside the large cloud masses. The CPR radar measures the power backscattered by clouds as a function of distance from the radar.

The 94 GHz frequency offers the best compromise of performance within the spacecraft instrument design. The footprint for a single profile is approximately 1.7 km along-track and 1.3 km across-track.

Cloudsat's radar sensitivity allows scientist to penetrate into the clouds with a unprecedented level of detail, and provides the first time global vertical cross section, showing how clouds form, evolve and affect weather and climate.

2.3.2.5 Meteosat 7 satellite

Meteosat 7 is a geostationary satellite, launched on September 1997. Meteosat 7 is the last of Meteosat First Generation geostationary satellite series, that have provided full Earth's images for 25 years continuously. On November 1995 Meteosat satellites passed under the control of EUMETSAT (European Organization for the Exploitation of Meteorological Satellites). Meteosat 7 has moved to 57.5° E, after Meteosat 8 reached the full operational stage in 2005, in the frame of the Indian Ocean Data Coverage (IODC) Service, and the primary mission is to provide high resolution images over the Indian Ocean and surrounding areas.

Its main instrument is the Meteosat Visible and InfraRed Imager (MVIRI) which operates in three spectral channels: visible, infrared, and water vapour regions of electromagnetic spectrum, chosen in accordance of the primary Meteosat missions of mapping clouds distribution and water vapour distribution.

Meteosat 7 provides data from MVIRI every 30 minutes, in the form of radiance from the visible and infrared channels. The visible band (0.45- 1.0 μm), used for

daylight imaging, corresponds to peak solar irradiance (transparent atmospheric gases), while the water vapour absorption band (5.7-7.1 μm) provide the amount of water vapour in the upper trophosphere. The thermal infrared band is used for day and night imaging, measuring the cloud tops temperature and the ocean's surface temperature.

2.3.2.6 FengYung-2C satellite

FengYung-2c (FY-2C) is a geostationary satellite developed by Shanghai Academy of Space Flight Technology and China Academy of Space Technology and operated by CMA. The FY-2C is the first Chinese operational meteorological satellite, launched on October 2004 and located above the equator at longitude 105°E.

The objective of the mission is to monitor the temperature and the clouds above China and neighbouring areas and also to provide meteorological information for the Asia-Pacific region. The upgraded Stretched-Visible and Infrared Spin-Scan Radiometer (S-VISSR) is one of the major payloads onboard the FY-2C. This optical imaging radiometer consists of one visible channel and four infrared channels. It can acquire one full disc image covering the Earth surface from 60° N to 60° S in latitude and from 45° E to 165° E in longitude per hour and 30 min per acquisition for flood season.

Chapter 3

Data and Algorithms for precipitation retrieval over the Plateau

In this Chapter will be described the data from raingauges, ground radars, remote sensors and control data available for the set up of precipitation observation tools over the Tibetan Plateau. The CEOP-AEGIS Project focused on three years, from 2008 to 2010, and all the data collected are within this period. Radar and raingauge data have been delivered as case studies for selected rainfall episodes occurred on the Plateau: these data have been used to study precipitation characteristics and to calibrate and set up satellite algorithms. Satellite data used to perform precipitation estimation have been collected for the whole three year period.

The algorithms used for the precipitation estimates are also introduced and described in this chapter.

3.1 3-years raingauges and 3-D radar gridded data for case studies and technique calibration.

The datasets provided by CMA in the frame of CEOP-AEGIS project will be described.

The datasets delivered are:

1) Hourly raingauges data over the Tibetan Plateau and surrounding areas
2) 3D mosaic of quality controlled radar reflectivity data for Qinghai region
3) 3D mosaic of quality controlled radar reflectivity data for Tibet region

4) Quantitative Precipitation Estimation from adjusted radar data for Qinghai region

5) Quantitative Precipitation Estimation from adjusted radar data for Tibet region

3.1.1 Rain Gauges Data

In Table 3.1 the main characteristics of raingauge gridded data, delivered by CMA are shown.

Table 3.1 Raingauge data characteristics.

day of the year YYYYMMDD	grid size Lines x Columns	Latitude min - max	Longitude min - max	Grid step (deg) in lat lon
20080720	300x500	25.05 - 40.00	78.05 - 103.0	0.05
20090716	300x500	25.05 - 40.00	78.05 - 103.0	0.05
20090801	300x500	25.05 - 40.00	78.05 - 103.0	0.05
20090802	300x500	25.05 - 40.00	78.05 - 103.0	0.05
20090726	300x500	25.05 - 40.00	78.05 - 103.0	0.05
20090727	300x500	25.05 - 40.00	78.05 - 103.0	0.05
20090728	300x500	25.05 - 40.00	78.05 - 103.0	0.05
20090816	300x500	25.05 - 40.00	78.05 - 103.0	0.05
20090802	300x500	25.05 - 40.00	78.05 - 103.0	0.05
20100607	300x500	25.05 - 40.00	78.05 - 103.0	0.05
20100716	300x500	25.05 - 40.00	78.05 - 103.0	0.05
20100717	300x500	25.05 - 40.00	78.05 - 103.0	0.05
20100804	300x500	25.05 - 40.00	78.05 - 103.0	0.05
20100827	300x500	25.05 - 40.00	78.05 - 103.0	0.05

3.1.2 3-D mosaic of quality controlled radar reflectivity

The radar dataset consists in 3 dimensional volumes of reflectivity for the two regions covered by the radar: Qinghai (2 radars) and Tibet (4 radars). The volumes are recorded with time step of 5 minutes for 2008 and with time step of

6 minutes for 2009. In Table 3.2 and Table 3.3 are reported the radar data characteristics of Qinghai and Tibet regions, respectively.

Table 3.2 Qinghai radar data characteristics

Qinghai 3D Reflectivity day of the year	volume size lines x columns x levels	Latitude min - max	Longitude min - max	Step (deg) lat lon
20080718	601x601x33	33.599 - 39.609	98.779 - 104.789	0.01
20080719	601x601x33	33.599 - 39.609	98.779 - 104.789	0.01
20080720	601x601x33	33.599 - 39.609	98.779 - 104.789	0.01
20080721	601x601x33	33.599 - 39.609	98.779 - 104.789	0.01
20090716	423x492x20	34.349 - 38.579	98.540 - 103.460	0.01
20090802	423x492x20	34.349 - 38.579	98.540 - 103.460	0.01

Table 3.3 Tibet radar data characteristics

Tibet 3D Reflectivity day of the year	volume dimension lines x columns x levels	Latitude min - max	Longitude min - max	Step (deg) lat lon
20080618	641x1152x37	26.260 - 32.670	85.889 - 97.409	0.01
20080619	641x1152x33	26.260 - 32.670	85.889 - 97.409	0.01
20080718	641x1152x33	26.260 - 32.670	85.889 - 97.409	0.01
20080719	641x1152x33	26.260 - 32.670	85.889 - 97.409	0.01
20080720	641x1152x33	26.260 - 32.670	85.889 - 97.409	0.01
20090727	324x871x20	27.649 - 30.889	87.029 - 95.739	0.01
20090728	324x871x20	27.649 - 30.889	87.029 - 95.739	0.01
20090816	324x871x20	27.649 - 30.889	87.029 - 95.739	0.01

The size of the grid and the number of vertical levels vary as indicated in the tables. The data are stored as counts and have to be converted in reflectivity (dBz). An example of 3D reflectivity data image is shown in figure 3.1, where the level 6 CAPPI for the Tibetan radars is reported for 2009 08 16 at 11:12 UTC.

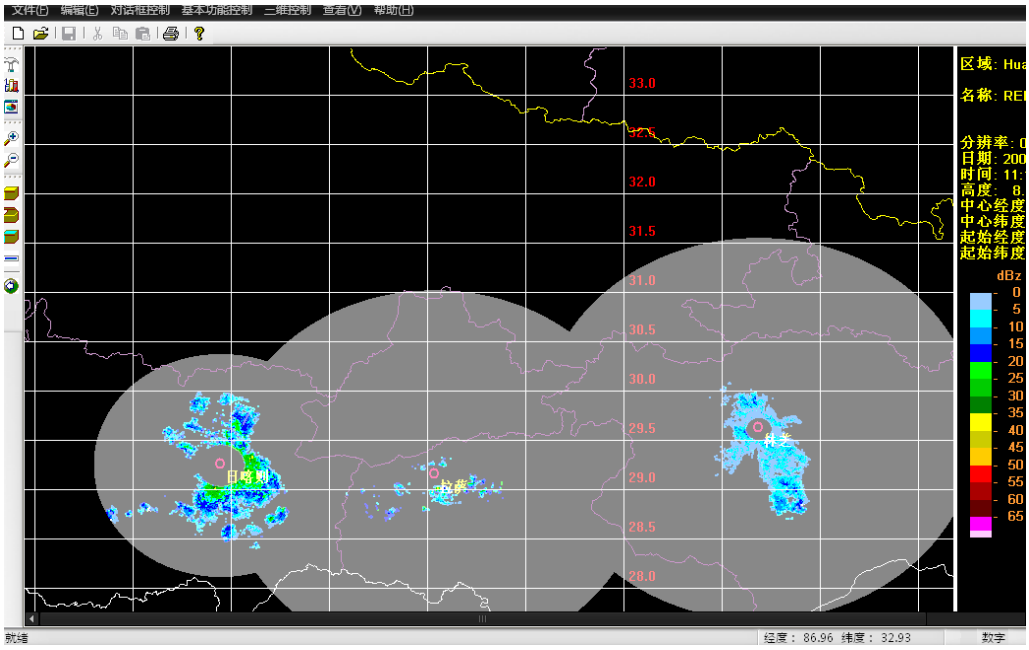

Figure 3. 1. Screen dump of the visualization of a level of the reflectivity volume.

3.2 Data from Satellites sensors

Satellite sensor data will utilized first to evaluate the sensitivity of different bands/channels to the precipitation on the ground, and then to develop and/or apply precipitation retrieval algorithms over the Tibetan Plateau.

3.2.1 MODIS data

The data of MODIS sensor in HDF-EOS format are downloaded from : http://laadsweb.nascom.nasa.gov

The granules dimension are 2030*1354 pixels, extracted by MOD021km-products and the geolocation data from MOD03-products, with a spatial resolution of 1km. The considered MODIS channels are shown in the Table 3.4 with their specific primary use.

Table.3.4 MODIS sensor bands characteristics

Band	**Wavelength** (nm)	**Primary use**
1	620–670	Land/Cloud/Aerosols Boundaries
2	841–876	
6	1628–1652	Land/Cloud/Aerosols Properties
18	931–941	Atmospheric Water Vapor
19	915–965	
Band	**Wavelength** (μm)	**Primary use**
20	3.660–3.840	Surface/Cloud Temperature
21	3.929–3.989	
31	10.780–11.280	Surface/Cloud Temperature
32	11.770–12.270	

3.2.2 AMSR-E data

The data product of AMSR-E/ Aqua L2A , contains brightness temperatures at 6.9GHz, 10.7GHz, 18.7GHz, 23.8GHz, 36.5GHz and 89GHz are downloaded from :

http://nsidc.org/data/amsre/index.html

All channels have a mean spatial resolution of 56km for L2A (smoothed) of AMSR-E, with a global coverage between 89.24°N and 89.24°S and granules dimension are approximately of 2002*243 pixels.

Format data are in HDF-EOS format. The data scale, the offset values and the data values in the specified units (Kelvin) are correlated by the relation:

$$\text{Data\_value\_in\_units} = (\text{stored\_data\_value} * \text{scale\_factor}) + \text{offset} \quad (3.1)$$

The scale_factor is 0.01 and the offset value is 327.68 then T_B (K) is defined:

$$T_B\,(\text{K}) = (\text{stored\_data\_value} * 0.01) + 327.68 \quad (3.2)$$

3.2.3 MVIRI data

The data of MVIRI sensor (on board the Meteosat 7 spacecraft) are downloaded from the EUMETSAT Earth Observation Portal, in EUMETSAT native format: (http://www.eumetsat.int/Home/Main/DataProducts/ProductNavigator/index.htm?l=en)

The full disc data called A-format, is 2500lines*2500column for the 11 μm thermal infrared and 6.7 μm water vapor channels, utilized for the interval 2008-2010, day and night every 30 minutes. Spatial resolution is 5x5 km^2 at sub satellite point (ssp) and approximately 7x10 km^2 over the Tibetan Plateau.

The IR pixel value is to be converted into radiance by the relations:

$$R = (\text{count} - \text{IRSPC}) * \text{IRCAL} \quad (3.3)$$

$$R = (IR - S) * c \quad (3.4)$$

where, *IR* is the count in the infrared channel, S are the Space_Count, an *c* is the Calibration Offset.

After the radiance has been computed, the corresponding temperature is picked up from the instrument specific radiance-to-temperature look-up tables.

3.2.4 Cloudsat-CPR data

Cloudsat-CPR data have been downloaded in HDF format from the Cloudsat Data Processing Center (http://www.cloudsat.cira.colostate.edu/index.php) for the cold and dry months (JFMAM-OND) of the years 2008, 2009, 2010, for a total of 807 orbits.

Radar reflectivity vertical profiles and auxiliary data have been downloaded for the satellite overpasses on the Tibetan Plateau. Auxiliary dataset includes the height of the vertical profiles radar bins and the air temperature at the ground, as estimated by the analysis of the European Center for Medium-range Weather Forecasting (ECMWF).

3.2.5 2A25 TRMM PR

2A25 is a higher level of PR data processing. Data collected by the precipitation radar (PR) onboard of TRMM satellite are processed from level 1 to 3. 2A25 is part of the level 2 of product type processed based on level 1 processing. 2A25 processing is to calculate Z factor correcting rain attenuation(Z_e) for each beam position using radar equation. The vertical product of rain rate (Rr) is produced on accordance with Z-R relationship ($R = a \cdot Z^b$). The calculation accuracy of rain rate is the output and each resolution pixel is 4kmx4kmx250m.

The 2A25 data product was downloaded from:

http://pmm.nasa.gov/TRMM/products-and-applications

3.3 Precipitation retrieval algorithms

In this section the retrieval algorithm considered for application over the Tibet Plateau will be described. A number of these algorithm are adapted from the

literature to work on the Plateau, others are originally developed for this work, and in cases of global products available from open archives (such as C-MORPH and TMPA) we simply downloaded the data of interest.

3.3.1 Cloudsat CPR Snow rate estimation technique

The main technical characteristics of CPR are: sensitivity defined by a minimum detectable reflectivity factor of -29 dBZ, cross-track and along-track resolution of 1.3 and 1.7 km, respectively, a dynamic range of 70 dB, 500 m vertical resolution and calibration accuracy of 1.5 dB.

The CPR sends 94 GHz wave pulses of a width of 3.3 μs with a repetition frequency of 4.3 MHz and measures backscattered power along the beam. The beam is sampled in 240 m deep bins and the measurement takes place in the lower 30 km of the atmosphere.

In figure 3.2 is shown the density of the CPR observation over the Plateau for the 2008, 2009 and 2010 for the cold season.

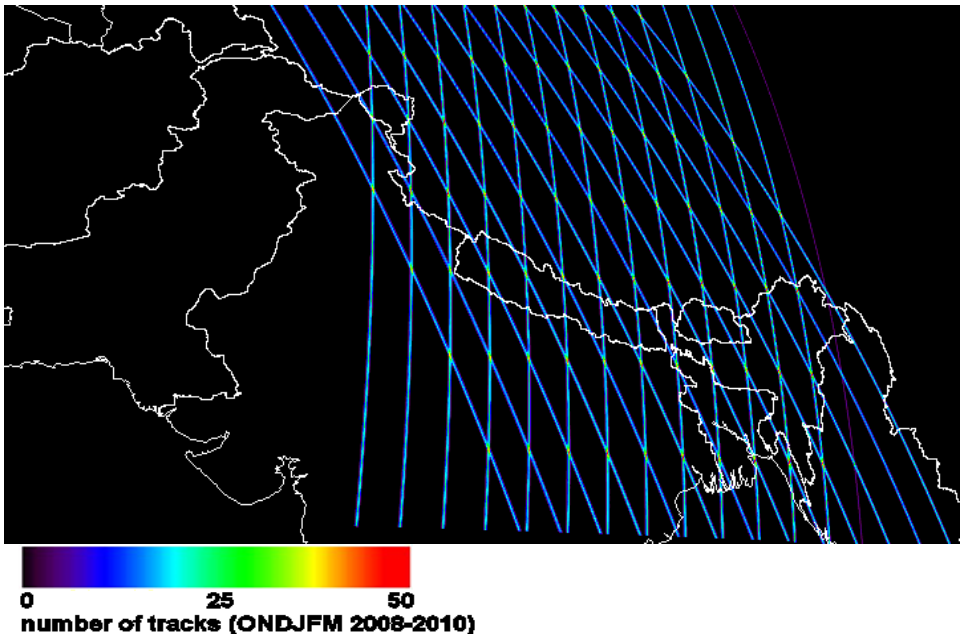

Figure 3.2. Number of CPR observations for the considered period.

The cold season is defined in this case for the months from January to May (JFMA) and for the months from October to December (OND). Approximately the satellite overpasses Tibetan Plateau twice a day.

The algorithm, originally developed for global scale application by Kulie and Bennartz (2009) works as follows.

A threshold reflectivity value of -15 dBz is assumed to indicate the presence of a cloud layer. The relationship between the radar equivalent reflectivity factor Z_e [mm^6 m^{-3}] and the amount of snow in the scanned volume is defined by the following equation (Kulie and Bennartz, 2009):

$$Z_e = \frac{\lambda^4}{\pi^5 \mid K \mid_\lambda^2} \int_{D_{\min}}^{D_{\max}} \sigma(D)_{b\lambda} N(D) dD \tag{3.5}$$

where λ is the radar wavelength, K the refractive index of the atmospheric targets (hydrometeors), D is their diameter, $\sigma(D)_b$ is the frequency-dependent backscatter cross section for an individual frozen particle shape and size, and $N(D)$ is the size distribution of the hydrometeors in the scattering volume. The snow rate can be obtained by an empirical relationship between snow particle size and mass and fall speed, as follows:

$$S = \frac{1}{\rho_w} \int_{D_{\min}}^{D_{\max}} v(D) m(D) N(D) dD \tag{3.6}$$

where ρ_w is the water density and $m(D) = aD^b$ and $v(D) = \alpha D^\gamma$ express the relation between the diameter D and particle mass m and velocity v, respectively. These relations are empirically determined, computing the a, b, α, γ coefficients as best fit from the literature (Kulie and Bennartz, 2009).

The relation between Z_e and S can be expressed in exponential form as $Z_e = aS^b$, where a and b coefficients have to be determined by scattering simulations and strongly depends on particles shape.

In Table 3.5 are reported the values of these coefficients determined by the particles shape (Kulie and Bennartz, 2009, Hiley et al., 2011).

Table 3.5. Values of the coefficients for the Z_e-S relationship for different particles size.

type	**a**	**b**
3 bullets rosette	13.16	1.4
aggregate	56.43	1.52
average	21.6	1.2
average + 1s	61.2	1.1
average - 1s	7.6	1.3

Over the Tibetan Plateau there are no observation available of particles size and shapes, thus a sensitivity study for the different a and b values listed in Table 3.5 has been carried out and the results are illustrated in figure 3.3, where the Probability Density Functions (PDF) for the snow rate over the Plateau are plotted. The sensitivity is rather high, and the snow rate distributions vary especially for the highest values, ranging from 1 to 5 mm h^{-1}.

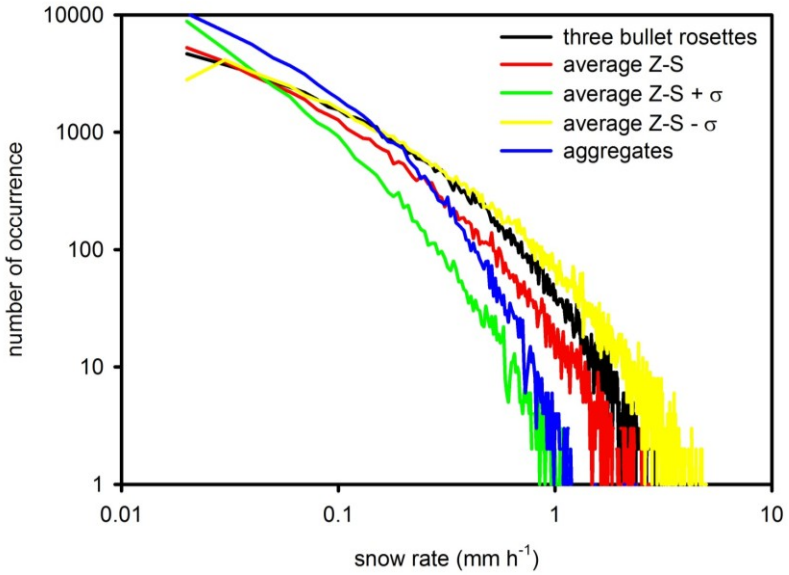

Figure 3.3 Snow rate PDF for the 2008-2010 cold season over the Plateau for different choices of *a* and *b* coefficients.

For the application to the Tibetan Plateau, the "three bullet rosette" coefficients are used, also compensating the different Diameter-Speed relation due to reduced air density above 3600 m a.s.l..

The algorithm logical steps can be summarized as follows (Kulie and Bennartz, 2009):

1) "near surface" reflectivity data are used. To avoid, or minimize, ground clutter contamination, the 6th bin from the surface is considered, i.e. about 1.3 km above the ground, as determined by the CPR DEM. This is especially needed over complex orography as in the case of Tibetan Plateau area.

2) Since the inversion scheme is based on the backscattering properties of frozen hydrometeors, a threshold in the 2 m temperature is applied. The retrieval is performed only where the 2 m temperature (from the ECMWF data) is lower than 273 K, minimizing the case of wet snow.

3) A threshold in the reflectivity value is then applied in order to consider only cloudy bins: the chosen value is –15 dBz. At the same time, a "vertical continuity" test is applied to screen out too thin clouds and residual clutter. Only profiles with at least 5 cloudy bins above the lowest considered are selected for retrieval: only clouds thicker than 1 km are processed.

4) The "three bullets rosette" reflectivity-snow rate relationship (Ze-S) is then applied to the lowest cloudy bin and the value assigned to the given profile.

3.3.2 C-NAW Algorithm

The Calibrated Negri-Adler-Wetzel technique is an IR technique based on the original NAW technique (Negri et. al, 1984), designed to estimate the instantaneous precipitation rate for convective cloud systems. It has been used in combination with ground radar precipitation data (Porcù et al, 1999) and with PMW estimates (Porcù et al., 2000, Kotroni et al., 2005, Casella et al., 2012),

where the radar/PMW estimates were used to calibrate the rainrate values to be assigned to the IR-defined rain areas. The cloud top temperature increases and the cloud thickness decreases with the distance from the convective center, as well as the capability to produce precipitation. The observation of Negri et al. (1984) shown that for about the half cloud area (the warmer one) no precipitation is registered, while stratified precipitation is expected below the 40% of the cloud area between the coldest 10% and the warmest 50%.

As a consequence of these findings, the NAW technique was originally set up as follows:

1) in the calibrated IR (11 μm channel) temperature image, the areas colder than 253 K are isolated and labeled as cloud;

2) for each cloud the temperature structure of the cloud top is analyzed and three areas are identified by means of two thresholds in temperature: coldest 10% (A10), warmest 50% (A50), remaining 40% (A40). Note that the threshold values in K vary from cloud to cloud;

3) nominal rainrates are then assigned to each cloud pixel according to its position in one of the three areas:

$RR(A50) = 0.0\ mmh^{-1}$

$RR(A40) = 2.0\ mmh^{-1}$

$RR(A10) = 8.0\ mmh^{-1}$

This choice was able to maximize the matching with daily cumulated rain measurement obtained with raingauges during the Florida Area Cumulus Experiment (Negri et al., 1984).

Further development shown the possibility to provide an on-line calibration of the technique, by using ground radar (Porcù et al, 1999) or PWM precipitation estimates (Porcù et al., 2000) to compute the actual rainrate of each cloud detected by the NAW technique.

To tailor the NAW technique to the Plateau, first we separated the Monsoon season from the rest of the year. For the summer (June to September) we considered as reference data for reliable precipitation the QPE products provided

by CMA. For the winter situation, usually dry with some snowfall, we considered as reference the CloudSat CPR snowfall algorithm implementation above introduced. After comparisons with rain (from the ground radar) and snowfall (from the CPR) fields, we found the best matches of the C-NAW estimates are reached with the following settings:

-for the cold-dry months (JFMAM-OND)

Tb threshold for cloud detection = 248 K

RR(A50) = 0.0 mmh^{-1}

RR(A40) = 0.25 mmh^{-1}

RR(A10) = 0.5 mmh^{-1}

-for the monsoon season (JJAS)

Tb threshold for cloud detection = 253 K

RR(A50) = 0.0 mmh^{-1}

RR(A40) = 2.0 mmh^{-1}

RR(A10) = 5.0 mmh^{-1}

The C-NAW technique has been applied to the Plateau region for the three years 2008, 2009 and 2010.

The IR data are from the METEOSAT-7 spacecraft. The 11 μm channels equivalent black body temperature are computed by using the calibration coefficients and the conversion tables available from the EMETSAT UMARF website.

3.3.3 CDRD Algorithm

The Cloud Dynamics Radiation Database (CDRD) Algorithm has been developed at the Institute for Sciences of the Atmosphere and Climate of the National Council of Research of Italy (ISAC-CNR) in Rome (Sanò, 2011, Casella, 2011,

Sanò et al., 2012), and it has been applied to the Tibetan region for the monsoon seasons 2008, 2009 and 2010.

3.3.3.1 The forward and the inverse problem

The CDRD algorithm is a cloud model-based statistical retrieval technique for estimating surface precipitation and cloud profiles. The retrieval is based on the Bayesian estimation theory. A schematic block diagram of CDRD is shown in figure3.3. The two boxes refer to the two main blocks common to all physically based retrieval approaches, referred as the "forward problem" and the "inverse problem". The forward problem consists in the generation of a database (the Cloud Radiation Database (CRD)), using a Cloud Resolving Model (CRM) and a Radiative Transfer Model. At the base of the forward problem there is the fact that precipitation on the ground can not be directly observed from space. It can be derived from knowledge of cloud microphysical structure along the direction of sight. Consequently, information relating cloud microphysics to observations from satellite-borne microwave radiometers needs to be contributed from external sources. Such microphysical information can be derived from a Cloud Resolving Model. The model used is the CRM "University of Wisconsin – Non-hydrostatic Modeling System" (UW-NMS) (Tripoli 1992).

A shortcoming of this approach is that it is currently not possible to run these models in-line with the flow of satellite data. It is therefore necessary to run the CRM off-line for a number of well-documented events (generally, results of re-analysis exercises) and collect the results in a database.

The collection of cloud and precipitation microphysical profiles for a series of different CRM simulations and of the associated TBs at the instrument (for instance SSM/I or SSMIS) channel frequencies constitutes the CRD. It is important to use several cloud model simulations for different types of precipitation systems, and to generate the corresponding cloud-radiation databases in order to specialize the algorithm to different storm structures.

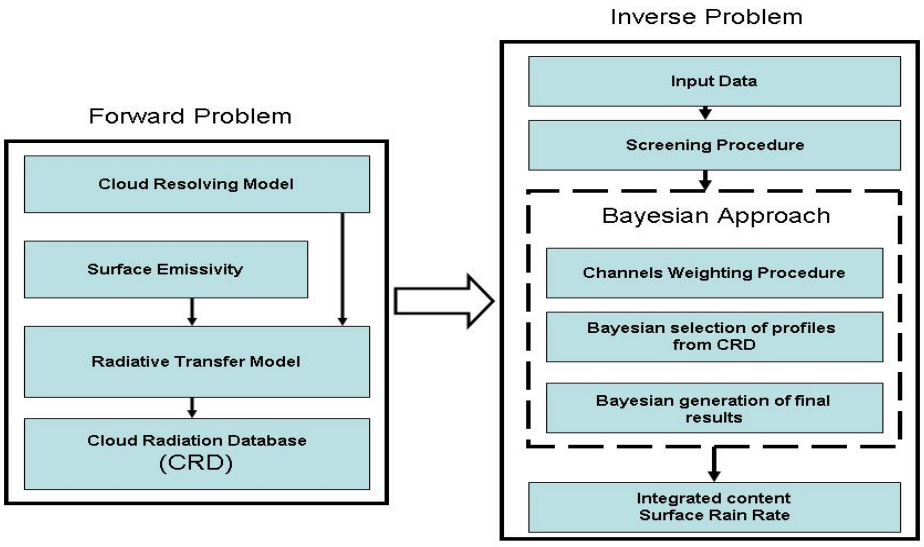

Figure 3.3. Block diagram of the Bayesian Algorithm for Microwave-Based Precipitation Retrieval (CDRD).

The inverse problem consists in the retrieval of meteorological parameters, the hydrometeor columnar content and the surface rain rates, using the experimental data (the brightness temperatures) of a microwave radiometer, and a probabilistic analysis (Bayesian) of the CRD.

3.3.3.2 The theoretical Bayesian method

The main resulting expressions of the theoretical Bayesian method utilized in the "inversion problem" will be presented. In the case of CRD database, considering the vector **g** related to a cloud profile and the multispectral vector t_m related of radiometer measurements, the optimal estimation of the minimum Mean Square (MMS) Bayesian method is defined as:

$$\hat{\mathbf{g}}_{MMS} = \int \mathbf{g}\, p(\mathbf{g}|\mathbf{t}_m)\, d\mathbf{g} \qquad (3.7)$$

According to Bayes Theorem the probability density function $p(\mathbf{g}|\mathbf{t}_m)$, can be expressed as:

$$p(\mathbf{g}|\mathbf{t}_m) = \frac{p(\mathbf{t_m} \mid \mathbf{g})p(\mathbf{g})}{p(\mathbf{t_m})} = \frac{p[\boldsymbol{\varepsilon}_t(\mathbf{g})]p(\mathbf{g})}{p(\mathbf{t_m})} \tag{3.8}$$

where $p(\mathbf{t}_m)$ is the pdf of $\mathbf{t}_m$, $p(\mathbf{g})$ is the apriori pdf of $\mathbf{g}$, $\boldsymbol{\varepsilon}_t(\mathbf{g})=[\mathbf{t}_m - \mathbf{t}(\mathbf{g})]$ is the Tb error with $\mathbf{t}(\mathbf{g})$ the simulated Tb vector related to $\mathbf{g}$ by means of the adopted radiative transfer model. Assuming that the errors in the observation and the simulated observations are Gaussian and uncorrelated, the approximate expression of the i-th element $\hat{g}_{MMS}(i)$ of the hydrometeor profile results as (the dependence of $\boldsymbol{\varepsilon}_t$ from $\mathbf{g}$ is not considered)

$$\hat{g}_{MMS}(i) = \frac{1}{k}\sum_{j=1}^{NP} g_j(i) \cdot \exp(-0{,}5 \cdot (\mathbf{t}(\mathbf{g}_j) - \mathbf{t_m} - \bar{\boldsymbol{\varepsilon}}_t)^T \cdot \mathbf{C}_{\varepsilon t}^{-1} \cdot (\mathbf{t}(\mathbf{g}_j) - \mathbf{t_m} - \bar{\boldsymbol{\varepsilon}}_t)) \cdot h(g_j(i), \Delta\mathbf{g}_j) \tag{3.9}$$

where $\mathbf{g}_j$ is the j-th profile sample of the cloud radiation database with $g_j(i)$ the i-th element, $\mathbf{t}(\mathbf{g}_j)$ is the corresponding Tb, $\mathbf{C}_{\varepsilon t}$ is the error covariance matrix, and $h(\mathbf{g}_i,\Delta\mathbf{g}_i)$ is the histogram relative to the sample $\mathbf{g}_i$ within a variable bin $\Delta\mathbf{g}$. The normalizing constant k is given by the expression

$$k = \sum_{j=1}^{NP} \exp(-0{,}5 \cdot (\mathbf{t}(g_j) - \mathbf{t_m} - \bar{\boldsymbol{\varepsilon}}_t)^T \cdot \mathbf{C}_{\varepsilon t}^{-1} \cdot (\mathbf{t}(g_j) - \mathbf{t_m} - \bar{\boldsymbol{\varepsilon}}_t)) \cdot h(g_j(i), \Delta\mathbf{g}_j) \tag{3.10}$$

The profiles (NP) utilized in the last expressions are selected from CRD database on the basis of the "Bayesian distance" $d2tb(\mathbf{g}_i)$ among the measured brightness temperatures ™ and the simulated $\mathbf{t}(\mathbf{g}_j)$ of the profile $\mathbf{g}_i$

$$D2tb(\mathbf{g}_i) = ((\mathbf{t}(\mathbf{g}_i) - \mathbf{t_m})^T \cdot \mathbf{C}_{\varepsilon t}^{-1} \cdot (\mathbf{t}(\mathbf{g}_i) - \mathbf{t_m})) \cdot \mathbf{W} \tag{3.11}$$

where **W** is the weight vector of the microwave channels. Profiles with a distance grater than an a-priori fixed threshold are rejected.

3.3.3.3 The retrieval system

In Figure 3.4 details of the inversion scheme of the inversion are illustrated. The scheme refers to the general case where, in addition to the use of brightness temperatures (TB), also the use of dynamical variable (Tag) is considered.

The TBs measured by SSM/I or SSMIS microwave radiometer are firstly processed (block "Interpolation Procedure") in order to estimate the TB measurements by all different channels at the same geographical position (latitude and longitude). This is necessary because the low frequency channels (19, 22, and 37 GHz) have larger footprints than the higher-frequency channels, and therefore a lower number of TBs is measured for them during each swath. Thus, an interpolation procedure is used for the low resolution channels. In parallel (block "Interpolation Procedure for Dynamical Variables") the values of tags obtained from NOAA are interpolated to match those of CDRD, in terms of time and geographical location (latitude, longitude).

Subsequently, all the TBs are analyzed with a "screening procedure" in order to reject areas (pixels) having incorrect TB values due to sensor errors (quality control screening), or recognized as areas without rain or with a very low probability of rain (geographic screening).

The PTC at 85 GHz is preferred in order to optimize the sensitivity to rainfall and spatial resolution. The TBs of selected pixels, and the corresponding tags, are then used for the inversion algorithm, using the data (TBs and tags of profiles) of the CDRD. In the inversion procedure, for each pixel a set of profiles must be selected from the database, basing on their proximity (in terms of TBs and tags values) to the observed (pixel) values.

This selection of profiles is carried out using the ”Bayesian distance” among the measured vectors of brightness temperatures and tags, and the corresponding simulated vectors of the previously selected set of profiles of the CDRD database.

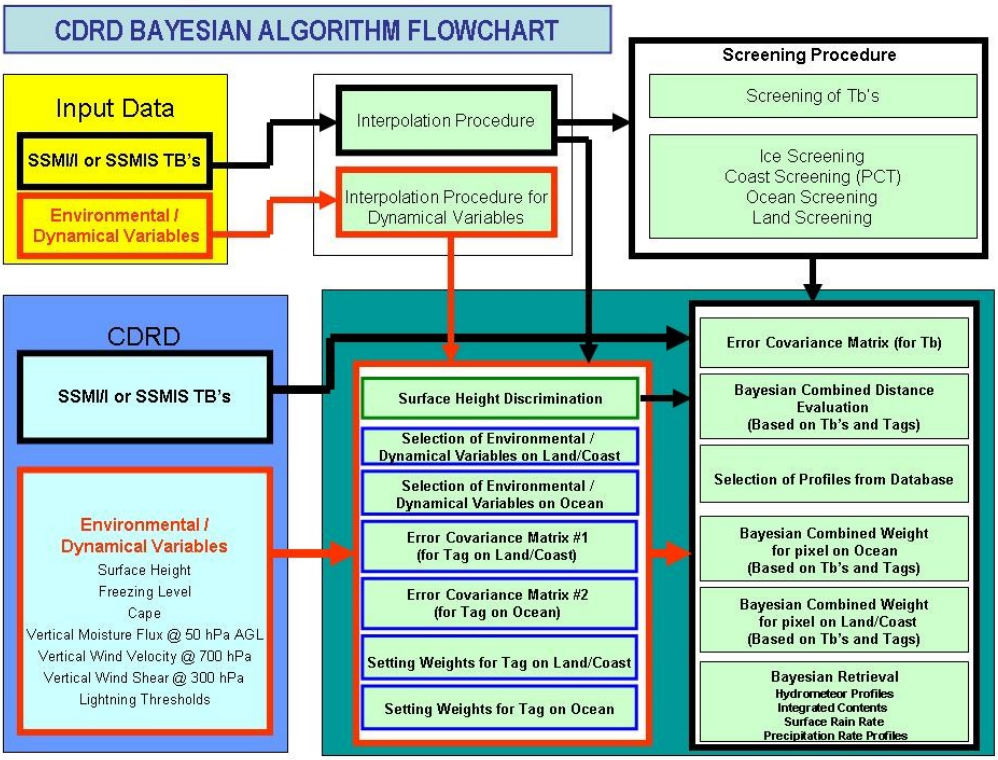

Figure 3.4. Block diagram of the CDRD retrieval algorithm.

The profiles obtained after the selection are used, with their different Bayesian weights depending on the proximity to the measured data, to compute the expected value of the retrieved surface rain rate and the associated rain rate Bayesian variance. For the application over the Tibetan Plateau, the collection of synthetic cloud and precipitation microphysical profiles obtained by CRM, have been integrated with three new simulations specifically carried out by UW-NMS for case studies over the Tibetan Plateau.

3.3.4 TANN Algorithm

The Tibetan Plateau Artificial Neural Network technique (TANN) is derived from a published algorithm (Capacci and Porcù, 2009): this technique has been developed using data from for mid latitude and trained with radar and raingauges data for different applications.

For this Project two TANN version have been implemented, with different reference precipitation fields in the training supervised datasets for the monsoon season. The first version, TANN-R, has been calibrated by using ground radar network QPE data, while the second one (TANN-S) makes use of the CDRD derived rainrate fields. For colder months the same training dataset have been used, based on CPR snow rate retrieval.

3.3.4.1 Physical basis

The type of neural network used here is the 'Multilayer Perceptron' or MLP (Rosenblatt 1962), which consists of input nodes, hidden nodes and output nodes, the nodes being called 'perceptrons'. The ANN configuration used is the single hidden layer version employing a sigmoidal transfer function at the nodes, as described by Pankiewicz et al. (2001). The input nodes are the numerical values of the selected features (i. e. satellite brightness temperatures and features): the appropriate set of features and therefore the number of input nodes has to be established. The number of outputs depends on the number of classes and ANN theory shows that each output is just the posterior class probability. Since the sum of the posterior probabilities of all the classes is 1 it is possible to reduce the number of outputs to the number of classes less 1. In the rain/no rain case, therefore, only one output is required and with the value 1 corresponding to the class 'rain' (more strictly, precipitation) the output is the posterior probability of the class precipitation or simply the Probability of Precipitation (PoP), to which a

threshold may be applied to delineate regions of precipitation. The output of each node in one layer is connected to the inputs of all the nodes in the next layer. The strengths of the connections are represented by continuously variable, signed multipliers known as 'weights'. The process of training the ANN consists of adjusting the values of these weights. To build the ANN there are two phases: the training phase and the testing phase. For these phases there are two independent data sets: the training data set and the testing data set. In the training phase the correct output has to be known a priori. Considering a series of labeled samples (0 = no rain, 1 = rain) the ANN generates an output value from each set of feature-values presented at its inputs. After each such presentation its internal weights are adjusted, until the ANN's behavior is stable and its output matches the true values to an acceptable accuracy. The ANN thus 'learns' to recognize the correct output from the input feature-values. The weights are adjusted using the well-known backpropagation method using gradient-descent applied to a sum-of-squares error function (see, for example, Bishop 1995: Chapter 4). In the testing phase, the weights remain fixed at the values established in the training phase and the ANN computes output values for a series of samples from an independent data set. From the ANN output, values less than or equal to 0.5 are considered to correspond to no rain, and those more than 0.5 to rain, in the original set up of the technique.

Taking the independent rainrate measurements (such as radar, raingaugesas or other satellite products) of precipitation 'true' indications of rain or no rain we can calculate statistical measures of ANN performance (Capacci and Conway, 2005). The main parameter used here is the Equitable Threat Score (ETS), but also Probability of Detection (POD) and False Alarm Rate (FAR) are used for diagnostic: all these parameters are defined below (Nurmi, 2003):

$$\text{Probability of detection: } \mathrm{POD} = \frac{H}{H+M} \tag{3.12}$$

$$\text{False-alarm ratio: } \mathrm{FAR} = \frac{F}{H+F} \tag{3.13}$$

Equitable threat score: $$\mathrm{ETS} = \frac{H - G}{H + M + F - G} \quad (3.14)$$

where $$\mathrm{G} = \frac{(H + M)(H + F)}{(H + M + F + Z)} \quad (3.15)$$

H (hits) = number of grid boxes correctly classified as rain,

M (misses) = number of grids boxes incorrectly classified as no rain,F (false alarm) = number of grids boxes incorrectly classified as rain, and

Z (correct no rain) = number of grids boxes correctly classified as no rain.

3.3.4.2 Implementation over the Tibetan Plateau

The original algorithm has been modified in order to work on the Tibetan Plateau area. First, three appropriated supervised dataset are created for the training phase of the network. A monsoon season training set used as "truth" data the observations of the ground radars operated by CMA (for the TANN-R algorithm). Also for the summer months training set used as 'truth' rain-rate data estimated by the CDRD algorithm, described in previous section (for the TANN-S algorithm). For the winter months, when rare and solid precipitation occurs, the training set was formed by using the CPR derived snowrate estimate, for both algorithms.

A second relevant modification was about the inputs: the original technique works on 9 channels of the SEVIRI on board Meteosat Second Generation, while for this project the three-channels MVIRI sensor on board METEOSAT-7 is used. Only two channels were continuously available night and day over the Plateau: WV and IR. The contribution of the WV channel is expected in removing cold soil contamination, since the WV weighting function is peaked in the upper troposphere and the WV radiation does not carry surface contribution. Earlier studies (Hsu et al., 1997, among others) shown that textural cloud top features can be also weakly related to the cloud structure and, therefore, to precipitation at the ground. Following this approach, two others input were added for each channel:

the local standard deviation and the average of the temperature in the IR and WV channels as computed over a 3x3 pixel.

Finally, the original technique provides as output and index varying between 0 and 1, that indicates the probability of precipitation. We fitted an empirical function that related the ANN output to the rainrate obtained by reference measurements (i.e. ground radar and CDRD algorithm for the summer and CPR for the winter), to convert the output in rainrate.

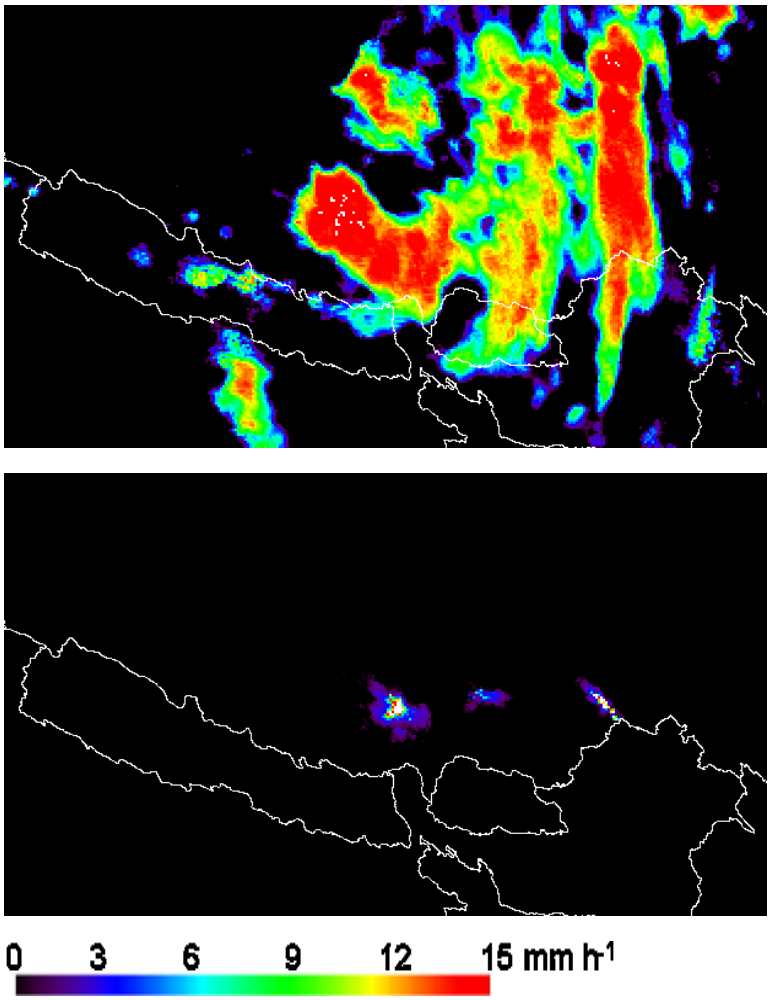

Figure 3.8. TANN-R (a) and radar (b) 3-hours averaged rainrate maps for the 24/08/2009 at 18:00 UTC

The TANN-R estimate is shown in figure 3.8 for the 24 August 2009 at 18:00 UTC in comparison of radar rain map at the same time, averaged over 3 hours.
It can be remarked that the calibration area (i.e. the area covered by the radar network) it is very small with respect to the region of interest, and also the calibration is carried on the same area, and thus the technique should not be able to resolve high rainrates events, such as the ones typically occurring on the eastern part of the Plateau (Ueno, 1998). The calibration carried on with CDRD satellite derived products is expected to overcome these problems, even if the quality of the satellite estimates is probably power than the one of radar QPE.

3.3.5 GCD technique

The original GCD (Global Convective Diagnostic) technique was developed (Mosher 2001, Martin et al., 2008) to delineate deep-convection areas from GEO observation. Further developments aim to assign precipitation rates to the deep-convection areas, after calibration with a reliable reference rainrate measurement. Precipitation based MW retrievals in conjunction with the GCD technique is a new method to provide precipitation estimates from heavy convective storm at the GEO time and space resolution (Casella et al., 2012), after a calibration with satellite derived rainrate estimates.
The technique works as follows. For each GEO IR pixel the brightness temperature difference ΔT_B between WV and IR channels, is interpreted as deep convection signal when is higher that a given threshold (-1 K).
A strong correlation between ΔT_B and RR can be found in the limitation of a single cloud and to a given time. A local empirical relation between two quantities can be obtained by calibrate ΔT_B in term of corresponding RR values, obtained from another reliable source.

In order to generate this relationship for each cloud and each corresponding observations, the (ΔT_B , RR) values that refer to all cloud pixels into 0.5K - intervals centered at 0K, ± 0.5K, ± 1K, ± 1.5K are grouped, and so on, within such intervals, the averaged RR values. These sets of (ΔT_B , RR) values can be fitted by exponential functions:

$$RR=\alpha e^{\beta \Delta T_B} \tag{3.16}$$

Where the best fit of α and β coefficient values, can vary considerably with season, latitude, time of the day and cloud type.

Then the GCD formula applies to all pixels for all GEO images associating rain rates values, for the selected cloud, until a new MW observation is available. An incorporated simple cloud tracking algorithm, makes possible to follow the evolution of the various precipitating clouds from a GEO observation to the next.

The GCD applied over the Tibetan Plateau uses radar derived QPE data to infer robust and flexible a and b values to be used in (3.16) to retrieve rainrate. The tests we carried on was really unsatisfactory, because the database we used for calibration did not allow to extend the relationship toward high rainrates. As an example, in Figure 3.9 is reported the ΔT_B-RR relationship we found for Tibet cases (left) and the one assessed by Casella et al. (2012) for Mediterranean area (right).

There are marked differences between the two datasets: over the Tibetan Plateau the dynamics of ΔT_B is much higher, spanning between -15 K to 10 K, but the rainrates are lower, while in the Mediterranean rainrates as high as 18 mm h-1 are related with comparably lower ΔT_B, around 3-4 K.

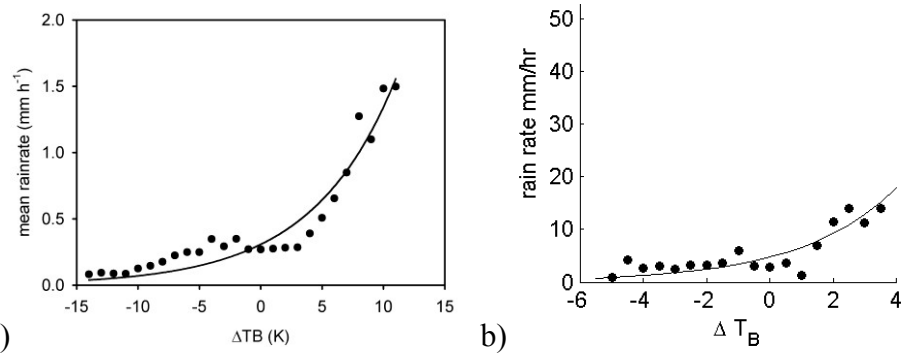

a) b)

Figure 3.9 Relationship of rainrate and brightness temperature differences: experimental data (black dots) and exponential fit (solid line). Plots refer to Tibet dataset (a) and Mediterranean dataset (b), as found in Casella et al (2012).

For these basic reasons we decided to not use GCD output in the precipitation analysis over the Plateau, considering also that, the ANN we introduced above is certainly able to manage linear combinations of input channels.

3.4 Available global precipitation products

Global satellite precipitation products are freely available on the web, released by scientific institutions and weather services, mainly for climatological purposes, but also can be used for satellite reference during the implementation of new algorithms, especially over ocean or region not covered by conventional instruments.

Two the different approaches make use of satellite data in the MW spectrum, usually to ensure a reliable quantitative rainrate estimates, while GEO IR is used to increase the temporal sampling of the estimate.

3.4.1 3B42-TRMM product

The TRMM Multisatellite Precipitation Analysis (TMPA) provides a calibration-based sequential scheme for combining precipitation estimates from multiple satellites, as well as gauge analyses where feasible, at fine scales (Huffmann et al., 2007). TMPA is available both after and in real time, based on calibration by the TRMM Combined Instrument (TCI) and TRMM Microwave Imager (TMI) precipitation products, respectively. Only the after-real-time product incorporates gauge data at the present. The dataset covers the latitude band 50°N–S for the period from 1998 to the delayed present on a grid 0.25x0.25 degrees.

Validation results show reasonable TMPA performance at monthly scales, although it is shown to have precipitation rate–dependent low bias due to lack of sensitivity to low precipitation rates over ocean. At finer scales the TMPA is successful at approximately reproducing the surface observation–based histogram of precipitation, as well as reasonably detecting large daily events. The TMPA, however, has lower skill in correctly specifying moderate and light event amounts on short time intervals, in common with other fine scale estimators.

The purpose of Algorithm 3B-42 is to produce Tropical Rainfall Measuring Mission merged high quality (HQ)/infrared (IR) precipitation and root-mean-square (RMS) precipitation-error estimates.

The 3B-42 estimates are produced in four stages; (1) the microwave estimates precipitation are calibrated and combined, (2) infrared precipitation estimates are created using the calibrated microwave precipitation, (3) the microwave and IR estimates are combined, and (4) rescaling to monthly data is applied. Each precipitation field is best interpreted as the precipitation rate effective at the nominal observation time.

3.4.1.1 High Quality (HQ) microwave estimates

All of the available passive microwave data are converted to precipitation estimates prior to use, then each data set is averaged to the 0.25° spatial grid over the time range ±90 minutes from the nominal observation time. All of these estimates are adjusted to a "best" estimate using probability matching of precipitation rate histograms assembled from coincident data. The algorithm takes the TCI as the calibrating data source. However, the coincidence of TCI with any of the sensors other than TMI is highly sparse, so we establish a TCI—TMI calibration, then apply that to TMI calibrations of the other sensors to estimate the TCI-calibrated values. After extensive preliminary testing, the ocean calibration is performed in regions of significant precipitation and applied everywhere. In all cases the calibration is a simple match-up of histograms.

The calibration interval is chosen to be a month to ensure stability and representativeness, except the TMI—AMSR-E calibration is computed with 2 months for stability.

Once the estimates are calibrated for each satellite the grid is populated by the "best" data from all available overpasses, although the most likely number of overpasses in the 3-hr window for a given grid box is either one or zero. When there are multiple overpasses, data from TCI, TCI-adjusted TMI, TCI-adjusted AMSR-E, and TCI-adjusted SSM/I are averaged together, and TCI-adjusted AMSU-B estimates are used if none of the others are available for the grid box. Tests show that the histogram of precipitation rate is somewhat sensitive to the number of overpasses averaged together when that number is small. Accordingly, in the future we expect to test a scheme taking the single "best" overpass in the 3-hr period.

3.4.1.2 Variable Rain Rate (VAR) IR estimates

The 3B-42 algorithm, for the period from 7 February 2000 onwards, the CPC merged IR is averaged to 0.25° resolution and combined into hourly files as ±30 minutes from the nominal time. The amount of imagery delivered to CPC varies by satellite operator, but international agreements mandate that full coverage is provided for the 3-hourly synoptic times from 00Z. Histograms of time-space matched HQ precipitation rates and IR TBs, each represented on the same 3-hourly 0.25° grid, are accumulated for a month, and then used to create spatially varying calibration coefficients that convert IR TBs to precipitation rates. As in the HQ, the calibration interval for the IR is a calendar month, and the resulting adjustments are applied to data for the same calendar month. This choice is intended to keep the dependent and independent data sets for the calibrations as close as possible in time. In fact, the full month of data in the estimates includes the dependent data. A second ambiguous screening is performed on the matched microwave data after accumulation; compared to instantaneous screening, the monthly screening provides better control of artifacts.

By design, there is no precipitation when the 0.25°x0.25°-average TB is greater than the local threshold value that matches the frequency of precipitation in the IR to that of the microwave. Increasingly colder TBs are assigned increasingly large precipitation rates using histogram matching. Those grid boxes that lack coincident data throughout the month, usually due to cold-land dropouts or ambiguous editing, are given calibration coefficients by smooth-filling histograms of coincident data from surrounding grid boxes. Once computed, the HQ-IR calibration coefficients are applied to each 3-hourly IR data set during the month.

3.4.1.3 Combined HQ and VAR estimates

The ultimate goal of this algorithm is to provide the "best" estimate of precipitation in each grid box at each observation time. It is frequently quite

challenging to combine different estimates of an intermittent field such as precipitation. The process of combining passive microwave estimates is relatively well-behaved because the sensors are quite similar and the Goddard Profiling algorithm (GPROF) is used for most retrievals. This is not the case for the HQ and VAR fields.

A simple approach for combining the HQ and VAR estimates is considered, namely the physically-based HQ estimates are taken "as is" where available, and the remaining grid boxes are filled with VAR estimates. This scheme provides the "best" local estimate, at the expense of a time series that is built from data sets displaying heterogeneous statistics.

3.4.1.4 Rescaling to monthly data

The final step in generating 3B-42 is the indirect use of rain gauge data. It is highly advantageous to include rain gauge data in combination data sets. However, experience shows that on any time scale shorter than a month the gauge data are not reported with sufficient density nor reported with consistent observational intervals to warrant direct inclusion in a global algorithm that provides sub-monthly resolution. The authors solved this issue in the GPCP One-Degree Daily combination data set by scaling the short-period estimates to sum to a monthly estimate that includes monthly gauge data. Here, we take a similar approach with the 3B-42 estimates. All available 3-hourly HQ+VAR estimates are summed over a calendar month to create a monthly multi-satellite (MS) product. The MS and gauge are combined to create a post-real-time monthly satellite-gauge combination (SG), which is a TRMM product in its own right (3B43). Then the field of SG/MS ratios is computed (with controls) and applied to scale each 3-hourly field in the month.

The monthly multisatellite (Ms) product are combined with gauge to create a post real monthly satellite-gauge combination (SG), which is 3B43 TRMM product.

3.4.2 CMORPH technique

CMORPH (CPC MORPHed precipitation) is a high resolution, real-time global precipitation estimates technique, developed at NOAA's Climate Prediction Center (CPC). CMORPH method uses precipitation estimates derived from low orbiter satellite microwave sensors, and whose patterns characteristic are transported via spatial propagation information that is obtained entirely form geostationary IR sensors (Joyce et al., 2004).

Half hourly IR from GEO satellites data are used as a means to transport the microwave-derived precipitation features during the intervals between subsequent PMW observations. Propagation vector-matrices are produced by computing spatial lag correlations on successive IR images of geostationary satellite, which is used to propagate the microwave derived precipitation estimates. The shape and the intensity of the precipitation features are modified (morphed) during the time between microwave sensor scans by performing a time-weighted linear interpolation. The method is flexible that permit precipitation morphing from any satellite source (AMSU, TMI, AMSR-E, SSM/I).

CMORPH shows substantial improvements over both averaging of the microwave estimates and over techniques that blend microwave and infrared information but that derive estimates of precipitation from infrared data when passive microwave data is unavailable.

The CMORP products is downloadable from the NOAA-CPC ftp-site: ftp.cpc.ncep.noaa.gov. Archived 3-hourly cumulated precipitation on a grid of 0.25×0.25 degrees are available from tear 2003 onwards, while last week instantaneous rainrates can be obtained at 8x8 km resolution every 30 minutes. Precipitation maps extend from 60S to 60N in latitude, given the extension of GEO satellites observation domain.

Chapter 4

Satellite precipitation estimates over the Tibetan Plateau: preliminary studies, applications and intercomparison

In this chapter firstly will be described the remapping phase of all dataset obtained from ground, satellite and algorithms retrieval. Secondly, will be presented a study on the sensitivity of sensors channels to the presence of precipitation at the ground, as measured by raingauges data as "truth" values. Then will be shown the result of all algorithms retrieval for the precipitation estimation over the Tibetan Plateau and, finally, will be described the validation of the algorithm results and intercomparison among the different algorithms.

4.1. Data remapping process

All the data processed in this work are received mapped on their own grid, determined by the Institution in charge of data pre-processing (CMA in case of raingauge and radar data), or by the data acquisition characteristics (e.g. geometry, resolution, type of the orbit) in case of satellite data. In order to design intercomparison studies and multisensor procedures, remapping procedures have been defined to reduce different data to the same grid. Three reference grids are defined onto which remap the data for different applications: the rain gauge grid, the radars grid and MVIRI grid. In figure 4.1 the considered grid are plotted: grid labelled as 1 is the raingauge grid, number 2 and 3 are the Tibetan and Qinghai radar grids, respectively, and number 4 is the MVIRI grid. Each satellite pixel in

its native grid is positioned accordingly with longitude and latitude values provided by the satellite navigation references.

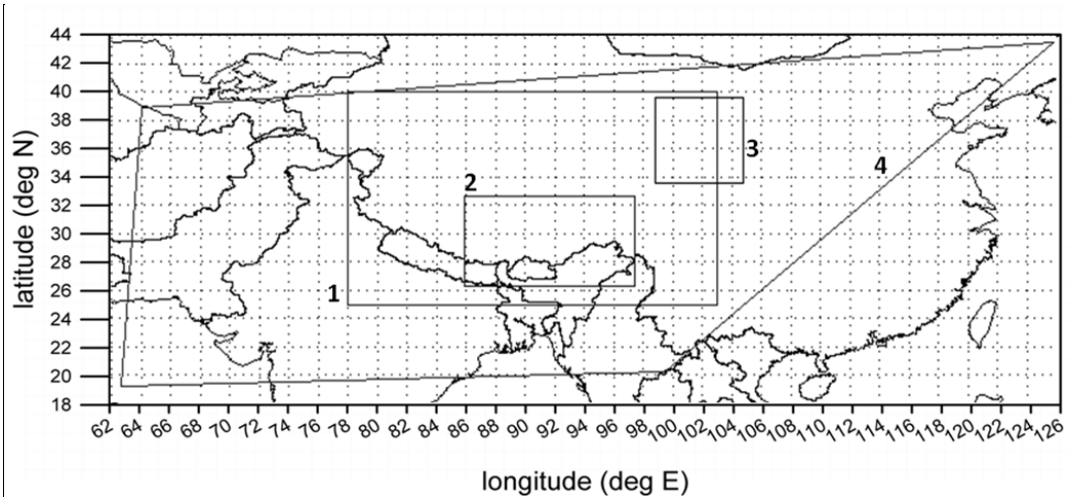

Figure 4.1. Plot of the reference grids used in this study: 1 raingauge; 2 Tibetan radar network; Qinghai radar network; 4 Meteosat MVIRI grid.

In the remapping process we calculate the pixel position with respect to the reference grid by using the Nearest Neighbour approach, which consist to associate at a given cell of the reference grid the satellite pixel closest to it, if it exists. Then the relative size of the satellite pixel with respect to the reference grid cell size is considered: if the reference grid cell is large enough to include more than one satellite pixel, the associated values will to be the averaged values of all satellite pixels contained in the grid cell.

In the table 4.1 is shown the remapping process for all data provided by the instrument and algorithm described in Chapter 3 and the grid referee. The pixel size of MVIRI (Meteosat 7) varies from the reference 5×5 km^2 at the sub satellite point (at coordinates 57E, 0N) due to the Earth curvature. On the Tibetan Plateau the pixel size varies approximately from 5.5×5.5 km^2, for the lowest latitude and longitude, to around 14×11 km^2 for the highest (see figure 4.1). In figure 4.2 is shown the distribution of MVIRI pixels area in the selected grid.

Table 4.1 Remapping data into the reference grid

REFERENCE GRID Size	Instruments data and algorithms retrieval data										
	GAUGE	**RADAR**	**MODIS**	**AMSRE**	**PR *TRMM***	**MVIRI**	**SSMIS**	**CPR**	**TANN**	**CMORPH**	**3B42**
GAUGES 0.05°×0.05°	*		□	●	●						
RADAR 0.01°×0.01°		*	●	●							
MVIRI ~7×9 km^2		□				*	●	●	*	□	□

Legend

* - coincident grids

● - Nearest Neighbour only

□ - Nearest-Neighbour and pixel averaging

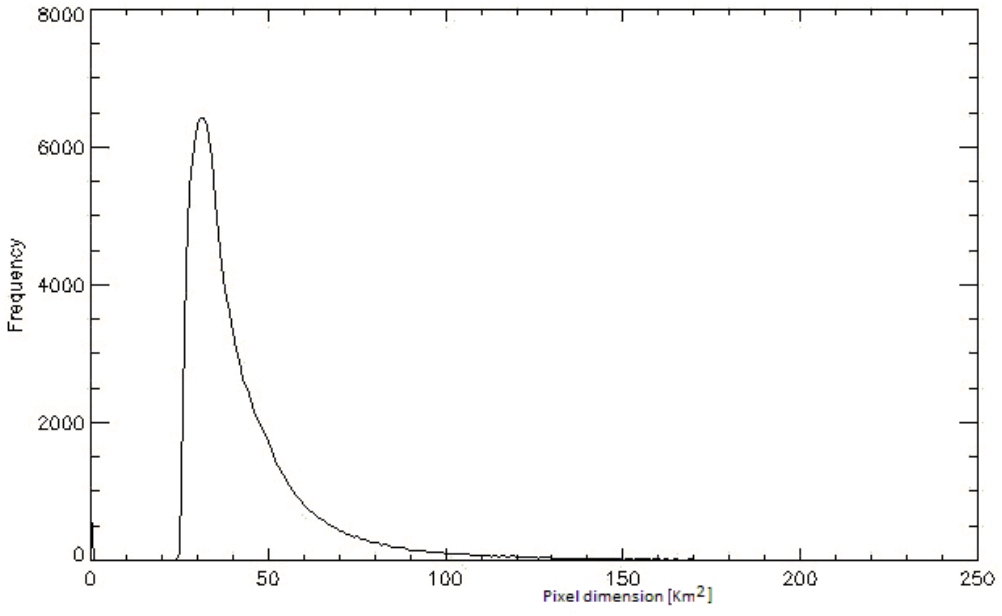

Figure 4.2. Distribution of MVIRI pixel area in the grid sketched in figure 4.1.

4.2 Sensitivity analysis for rain/no-rain discrimination

In this section will be investigated the sensitivity of the radiances at the wavelengths available for this study to the rain/no-rain discrimination. As true rainfall rate we used the raingauges measurements for selected case studies during the 2008 and 2009 monsoon seasons. For each channel of the considered sensors the measured radiance map is matched with the precipitation map obtained from the raingauges network. Two curves are then computed as function of the radiance value: one collects the number of satellite IFOV where gauges measured precipitation rates higher than 0.2 mm h^{-1} (rain curve), the other collects the number of IFOV without precipitation (no-rain curve). A wavelength is assumed to be sensitive to precipitation as far as the two curves are well separated in the plots, with moderate overlapping. On the contrary, the channel sensitivity is low if the two curves are mostly overlapped.

In the following we will be describe the sensitivity analysis of rain and no-rain discrimination of selected MODIS channels, all AMSR-E channels and the TRMM-PR 14 GHz sensor.

4.2.1 Sensitivity of MODIS channels

The channels sensitivity of the precipitation is determined by the normalized distribution of the radiance or reflectance of MODIS channels, for classes rain/no-rain of the hourly raingauges "truth" data. To make easier the comparison between the different channels, also the radiance values are normalized.

In Figure 4.3 (a) and (b) are shown the normalized reflectance distributions for precipitation classes rain/no-rain, of ch01 and ch02 (VIS wavelengths) which are primarily used for Land/Cloud/Aerosol discrimination, and in Figure 4.3 (c) the same for the channel ch06, in the short wave infrared at 1.6 μm, used for cloud particle size and phase estimate and for the detection of snow at the ground.

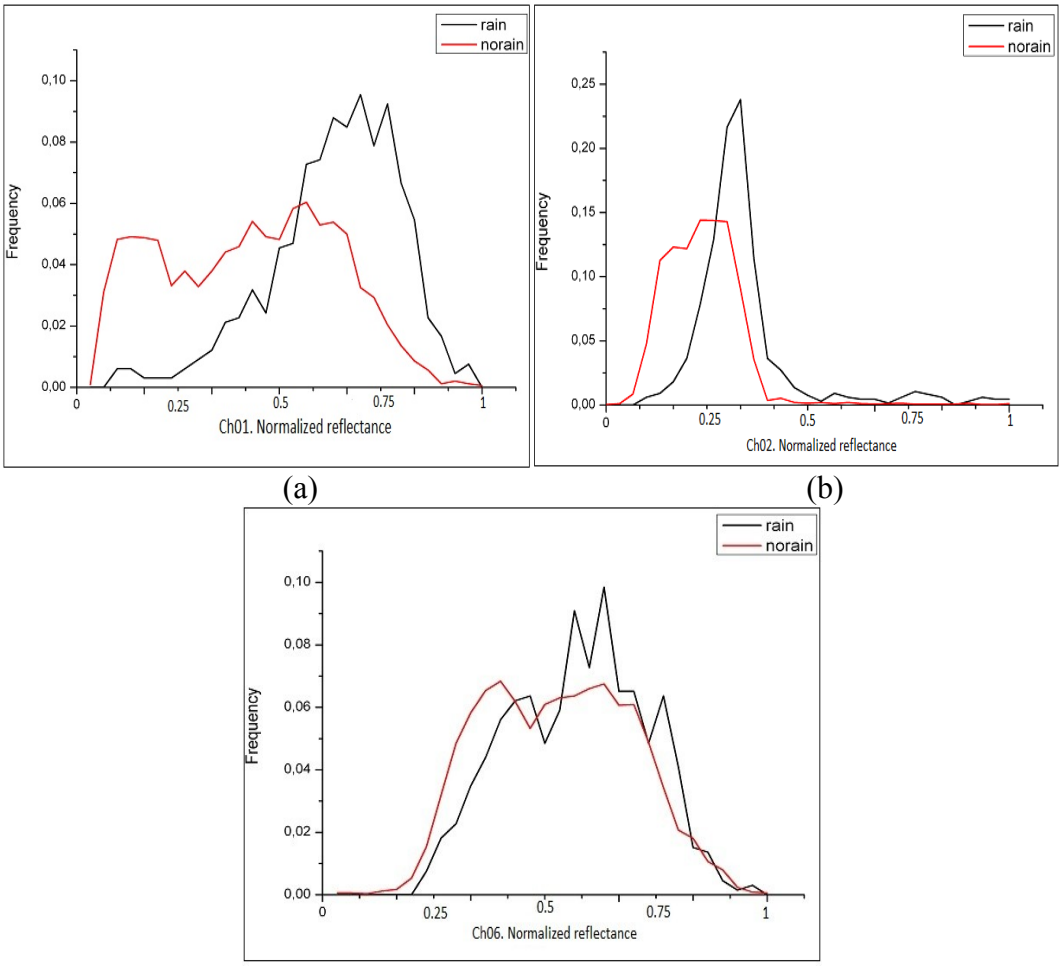

Figure 4.3 Normalized reflectance distributions for precipitation classes rain and non-rain. Channel considered: Ch01 (a), Ch02 (b) and Ch06 (c).

Results show very limited skill in rain detection of ch06, while ch01 is the most effective in separating rain and no-rain pixel given the contrast between dark background (in summer) and thick highly reflecting clouds. This behaviour is quite similar to what is known in the literature of other parts of the word (Capacci and Conway, 2005).

In Figure 4.4 (a) and (b) are shown the normalized radiance distribution for precipitation classes rain/no-rain, of the Ch18 and Ch19 sensitive to WV atmospheric content, showing good separation between curves.

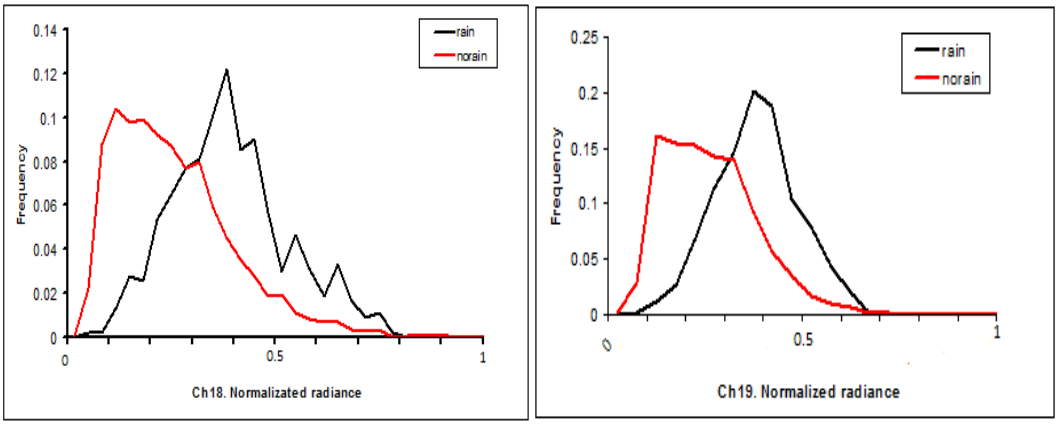

(a) (b)

Figure 4.4 Normalized radiance distributions for precipitation classes rain and no-rain. Channel considered: Ch18 (a) and Ch19 (b).

In the Figure 4.5 (a) and (b) are shown the normalized radiance distribution for precipitation classes rain/no-rain, of the channel 20 and channel 21 (NIR) , with primary use: Surface/Cloud temperature. In this part of the spectrum (around 3.9 μm) there is a contribution of solar reflectance and terrestrial emission during daytime, while during night-time only the emitted radiation is present. The reflected component of day-time data at this wavelength has been used as a strong indicator of precipitation (Lenski and Rosenfeld, 1997), since it is sensitive to cloud top particles size through the effective radius. The effective radius is defined as the ratio between third and second moments of the particle size distribution and is a weight of the relative importance of absorption and scattering properties of the cloud particles. The sensitivity of these channel to precipitation over the Plateau seems to be very small for both the considered channels.

This can be due to the fact that we could not separately consider day-time and night-time slots because the database was too limited.

In the Figure 4.6 (a) and (b) are shown the normalized radiance distribution for precipitation classes rain/no-rain, of the channel 31 and channel 32 (IR), with primary use: Surface/Cloud temperature. The window IR channels can be

considered as the most used for precipitation estimation because of its day and night availability.

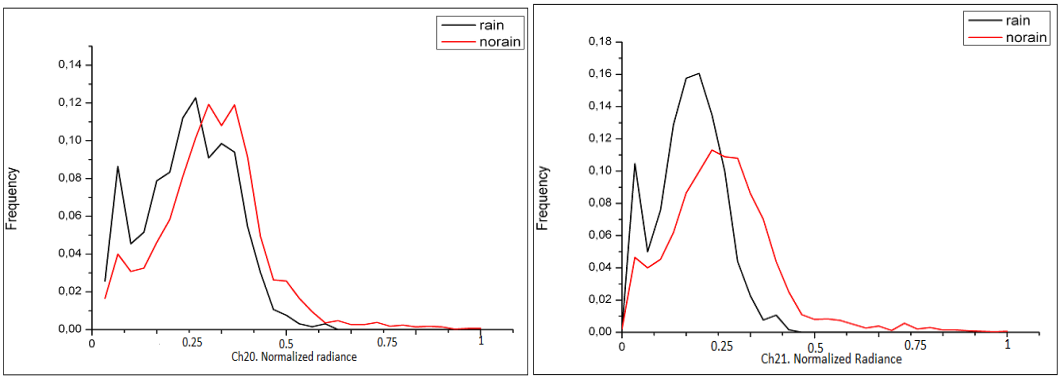

(a) (b)

Figure 4.5 Normalized radiance distributions for precipitation classes rain and no-rain for channels Ch20 (a) and Ch21 (b).

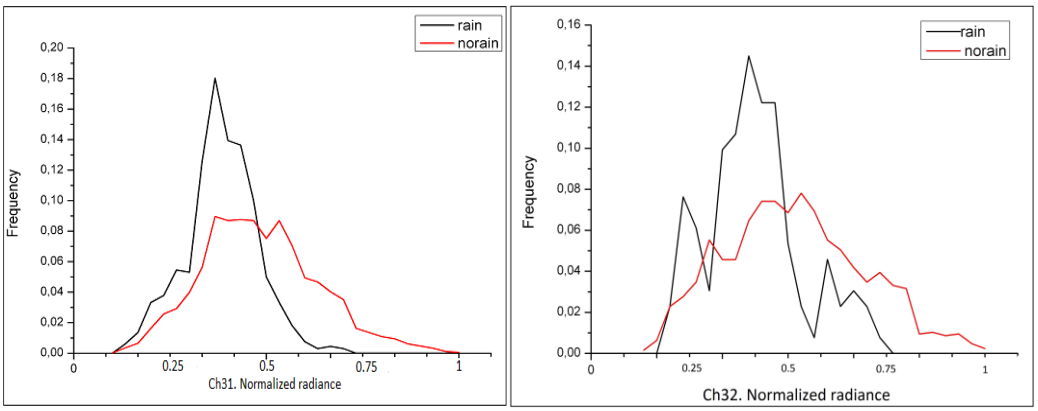

(a) (b)

Figure 4.6 Normalized radiance distributions for precipitation classes rain and no-rain for channels Ch31 (a) and Ch32 (b).

The radiance can be converted in brightness temperature, which is very close to the thermodynamic equilibrium temperature of the observed cloud top.

The rain/no-rain discrimination at IR window channels is similar for Ch31 and Ch32 and presents a rather sharp peak for precipitation for lower radiance values, while the no-rain curve spans over the whole radiance range. The Plateau cold

background during the night, also in summer, and the presence of relatively low top precipitating clouds (Shimitzu et al., 2001) contribute to make the contrast between precipitating cloud top and background less sharp with respect to other parts of the Earth.

The near-infrared total-column precipitable water is very sensitive to boundary-layer WV since it is derived from attenuation of reflected solar light from the surface. Techniques employing ratios of WV-absorbing channels 17, 18, and 19 with the atmospheric window channels 2 and 5 are used. The column WV amounts are derived from the transmittances based on theoretical radiative-transfer calculations and using look-up-table procedures. Other, split-window, methods also exist. This class of techniques uses the difference in WV absorption that exists between channel 31 (10.78-11.28) μm and channel 32 (11.7-12.27) μm. In this case of study the channel 31 and 32 is not sensitive for the rain/no-rain discrimination.

4.2.2 Sensitivity of AMSR-E channels

To test the sensitivity to precipitation of the PMW channels we considered the AMSR-E data because it has very similar frequencies as other widely used sensors, such as TMI and SSM/I. As for the MODIS channels, the TB values are matched with raingauges rainrates maps for the available case studies, and rain/no-rain curves are plotted. In the Figure 4.7 are shown normalized brightness temperatures distribution of 6.9 GHz, 10.7 GHz and 18.7 GHz horizontally and vertically polarized channels.

The radiation measured at the lowest frequencies in the PMW spectrum mainly carries information on the large water drops in the cloud rain layers: the relatively long wavelength (between 4 and 1.6 cm) makes the interaction with small cloud droplets and crystals negligible, so the radiation emitted by cloud drops (water is a good emitter in the MW) can reach the satellite with little extinction (Ferraro et al.,

1998). The signal from precipitation layers, however, is often masked by the strong signal coming from the surface (especially land). The emissivity of the ground in PMW is usually highly polarized and rapidly varying in space and time, due to the dependence of the soil emissivity on its condition: vegetation and its conditions, moisture content, and snow cover modify the amount of radiation reaching the sensor.

Thus it is often difficult to screen out the ground contribution from the total measured radiation to isolate the rain signal and number of different approaches have been pursued in the literature (Levizzani et al., 2007).

From the figures, it seems that the only channel with a marked separation between rain and no-rain curves is the vertically polarized 6.9 GHz, which shows the rain slightly colder than the no-rain peak. For other channels the sensitivity to precipitation is very low.

Increasing the frequency, thus decreasing the wavelength, the interaction of the radiation with smaller cloud particles and crystals becomes more effective, due to scattering, and the radiation reaching the satellite carries information on the cloud upper layer.

The signal at 89.9 GHz (corresponding to λ = 3.3 mm), as an example, is a measure of the scattering due to ice particles on the upper cloud layers. Also at these frequencies it is expected a strong surface signal, able to mask the atmospheric contribution.

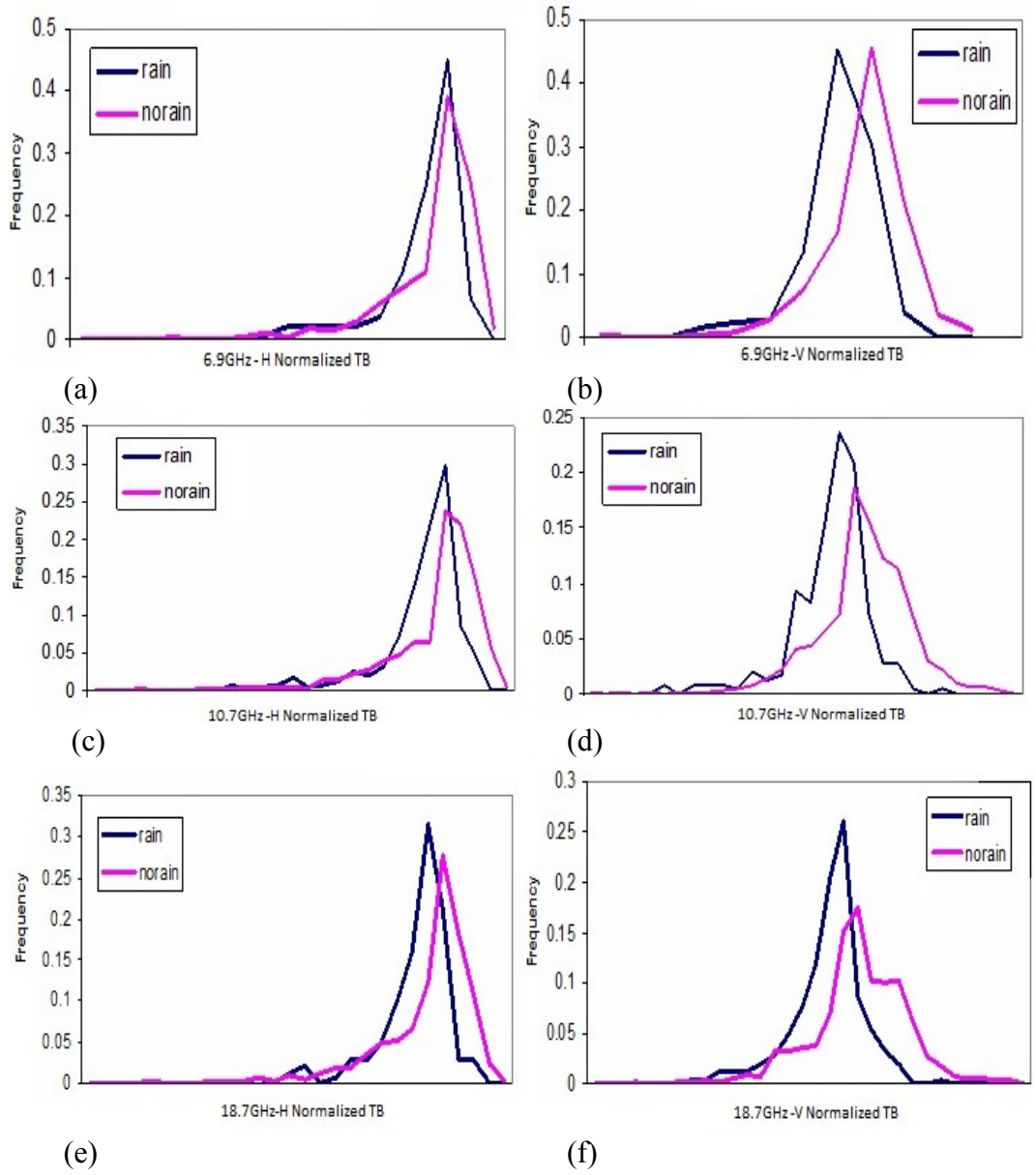

Figure 4.7 Normalized distribution of TB6.9H (a) TB6.9V GHz (b), TB10.7H GHz (c) TB10.7V GHz (d), TB18.7H GHz (e), and 18.7V GHz (f) in correspondence to wet and dry raingauges.

In figure 4.8 are shown normalized brightness temperatures distribution at 23.8 GHz, 36.5 GHz and 89.0 GHz at horizontal and vertical polarization.

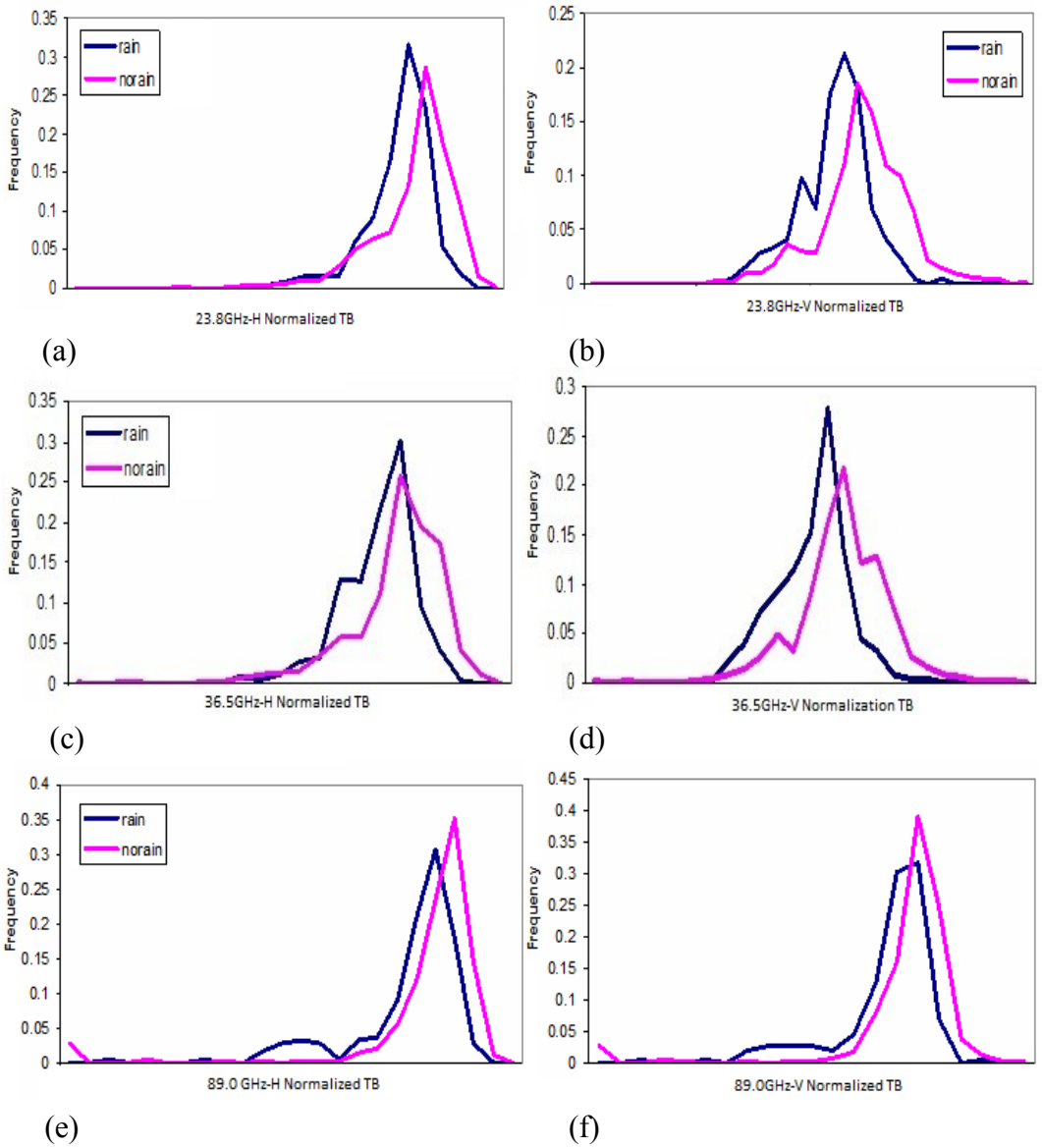

Figure 4.8 Normalized distribution of TB23.8H GHz (a), TB23.8V GHz (b), TB36.5H GHz (c), TB36.5V GHz (d), and TB89.0H GHz (e), and TB89.0V GHz (f) in correspondence to wet and dry raingauges.

Also at these wavelengths the separation between rain and no-rain curves is often negligible: the rain curve peak is always colder than the no-rain peak, but with only few degrees of difference. The TB89.0 distribution at both polarizations,

however, shows a smaller, secondary peak rather colder for the rain curve, probably related to heavy precipitation cloud with thick ice layer at the top.
The channels considered in this study are in window regions of the MW spectrum, i. e. the radiation interacts very weakly with atmospheric gases. A valuable approach to retrieve precipitation from absorption channels has been pursued (Cheng and Staelin, 2003, Laviola and Levizzani, 2010). These techniques retrieve precipitation as signal in the water vapour or oxygen emitted radiation. The main advantage is that the contribution of the soil usually does not reach the satellite, being absorbed by gas layers in the atmosphere. On the Tibetan Plateau, however, the atmosphere is thinner (and generally dryer) than in other part of the Earth, and the integral gas content is lower, so that also the signal in absorption bands can be contaminated by surface contribution. For these reasons, we did not consider the sensitivity to MW absorption channels. Moreover, for the PMW retrieval of the Tibetan Plateau, we considered the output of the CDRD algorithm, that fully exploit the physical contents of the MW channels.

4.2.3 Sensitivity of TRMM PR

The TRMM-PR sensitivity of the precipitation is determined in the same way as dome for passive sensors, and results are shown in figure 4.9 for the 2008 and 2009 case studies. We considered the 2A25 TRMM-PR precipitation product (Iguchi et al., 2000), and rain and no-rain curves are plotted as function of the estimated rainrate.
The plots reported show very limited sensitivity, since rain and no-rain curves are mostly overlapped, indicating the inability of TRMM-PR to correctly assign precipitation, when it is well known in literature that TRMM-PR usually provides the best rainrate estimate available from space borne sensors. Two reasons can explain this behaviour: 1) the database is very limited and, given the narrow TRMM-PR swath, the plots are constructed with very few points, 2) the rainfall

rate during these events was low and moderate, where the TRMM-PR estimates are expected to be less accurate.

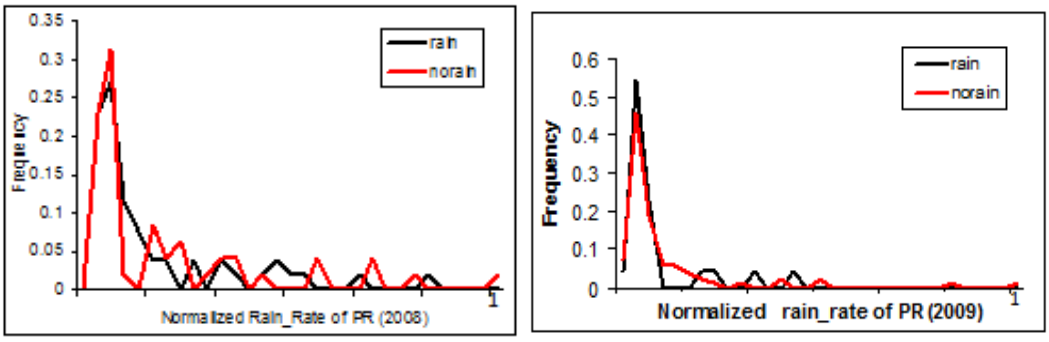

(a) (b)

Figure 4.9 Normalized Rain-Rates distributions of 14GHz PR, to hourly raingauge precipitation as "truth" values.

4.3 Implementation and/or application of retrieval algorithms

To provide rainfall estimation over the Tibetan Plateau, different approaches have been used, as outlined in chapter 2, and the results are described in the next sections. In Table 4.2 implemented algorithms and product characteristic are summarized.

A two steps strategy to implement an effective precipitation estimation approach has been developed, considering the known seasonal characteristics over the Tibetan Plateau. First, two "physical" retrieval algorithms was used for accurate precipitation retrieval during cold months (from January to May and from October to December) and warm season (June to September).

Table 4.2 Algorithms implemented over the Tibetan Plateau.

Algorithm	**Sensor**	**Frequency/ wavelength**	**Time resolution**	**Ground resolution**
KB	CPR/CloudSat	Radar 94 GHz	twice a day over HB	1.3×1.7 km^2
CDRD	SSMI/S	19 to 190 GHz	~6 hours	15×15 km^2
TANN-R TANN-S	MVIRI	6.7 μm + 11 μm	30 min	~6×7 km^2
3B42	MVIRI + TMI + AMSR-E + AMSU-B	11 μm 6 to 190 GHz	3 hours	0.25×0.25 deg
C-MORPH	MVIRI + TMI + SSMIS + AMSU-B	11 μm + 6 to 190 GHz	3 hours	0.25×0.25 deg
C-NAW	MVIRI	11 μm	30 min	~6×7 km^2

In cold months it is expected mainly snowfall and light precipitation, thus an algorithm based on Cloudsat-CPR data has been implemented, while during monsoon season, when convective activity is expected to dominate, a PMW algorithm has been used.

In the second stage, the outputs of the two algorithms have been used to seasonally calibrate IR based retrieval techniques, based on statistical approach.

4.3.1 Implementation of the "seasonal" algorithms

In the next sections will be shown some results of the two satellite algorithms used to calibrate statistical rainrate retrieval algorithms.

4.3.1.1 Snowrate retrieval from Clousat-CPR data (Kulie and Bennartz, 2009)

About 800 CloudSat overpasses have been processed to retrieve snow rate: given the narrow (1.7 km) CPR swath, it is not possible to separately analyze the results of each overpass, and only averaged products will be shown. In figure 4.10 maps at the resolution of 50x50 km^2 are shown for frequency of snowfall and mean snow rate during the whole set of CPR retrievals.
The maximum snowfall frequency (around 50%) is registered in the Karakorum region on the western part of the domain, where also the highest average snow rate is estimated. The southern part of the Plateau seems to be dry even during the winter, while relatively high frequency is also measured on the northern part and high snow rate is found in south-eastern Plateau.
In figure 4.11 are reported three curves. The black one represents the number of 50×50 km^2 pixel of the domain as function of the percentage of overpasses with snowfall with respect to the total satellite overpasses. The green line shows the number of pixel as function of the percentage of cloud covered overpasses, while the red line represents the number of pixels as function of the percentage of snowfall observations with respect to cloudy observations.

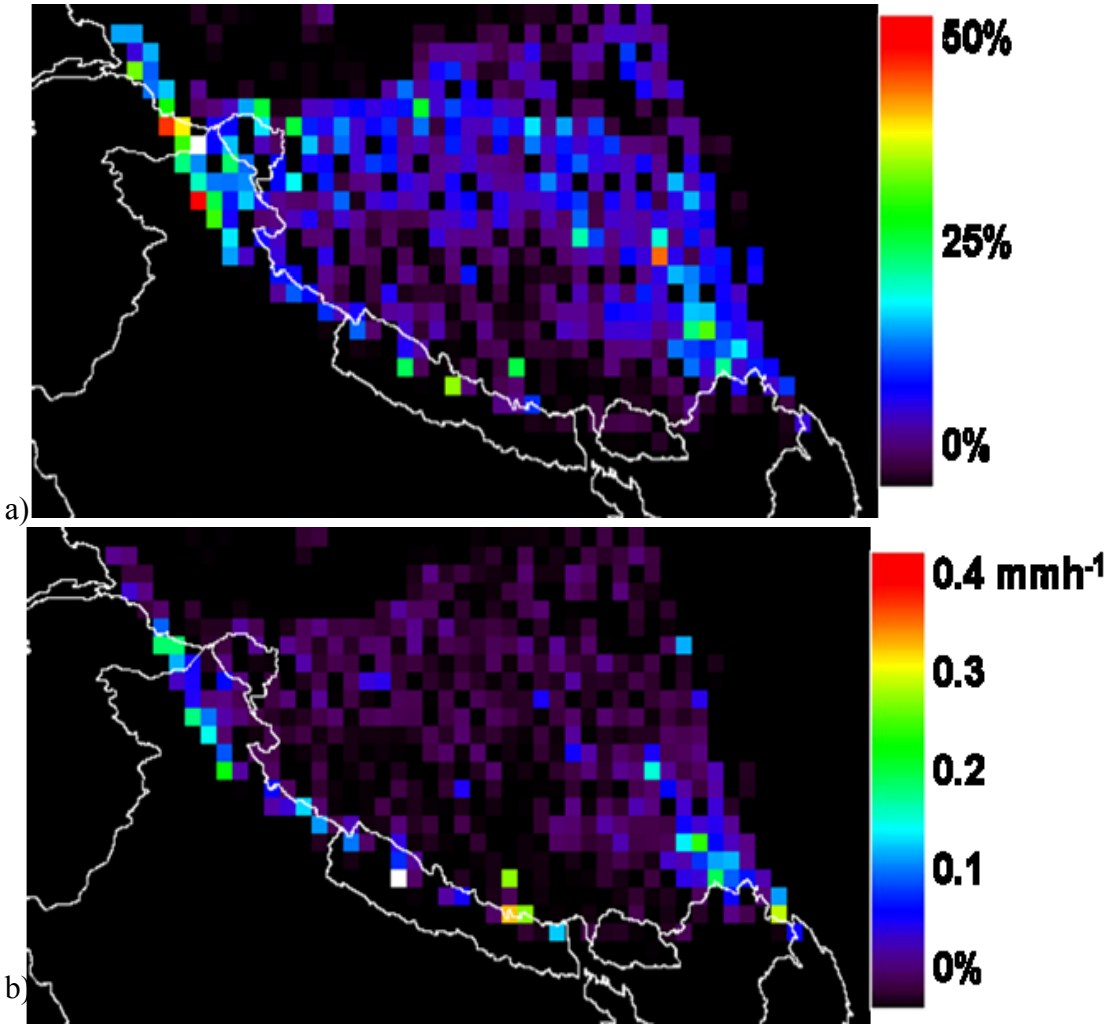

Figure 4.10 Frequency of snowfall occurrence (a) and averaged mean snowfall rate (b) for the years 2008, 2009 and 2010 (805 overpasses)

In most of the areas visited by CPR the frequency of snow occurrence is below 15% (90% of the areas has less than 15% of occurrence), with very few spots between 40% and 50%. The sky is covered between 10% and 40% of the times, while the fraction of producing snow clouds could also very high (above 50% for the 15% of the pixels), but the distribution does not presents marked peaks.

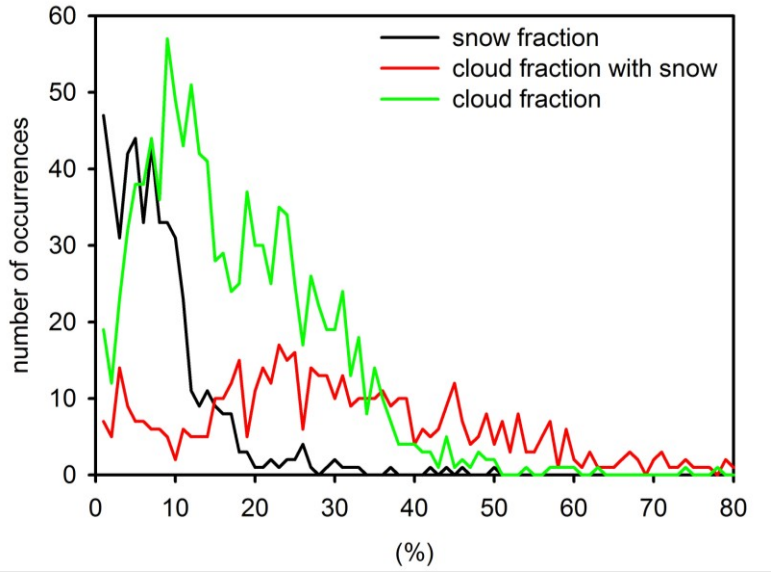

Figure 4.11 Number of 50×50 km^2 pixel as function of cloud fraction (green line), snow fraction (black line) and cloud fraction with snow (red line) for the considered periods.

4.3.1.2 Output of the CDRD technique over the Tibetan Plateau

The CDRD rainfall maps have been provided by the ISAC-CNR in Rome, where the algorithm is developing (Sanò et al, 2012). Four months of SSMI/S overpasses for the years were processed: SSMI/S sensor is currently on board the DMSP satellites F-16, F-17 and F-18, the latter launched in 2010 March. Given the different number of available satellites, the number of overpasses varies across the years: 1312 in 2008, 1314 in 2009 and 1939 in 2010.

As an example, in figure 4.12 the CDRD rainrate map for a case study in 2009 is presented at its original resolution.

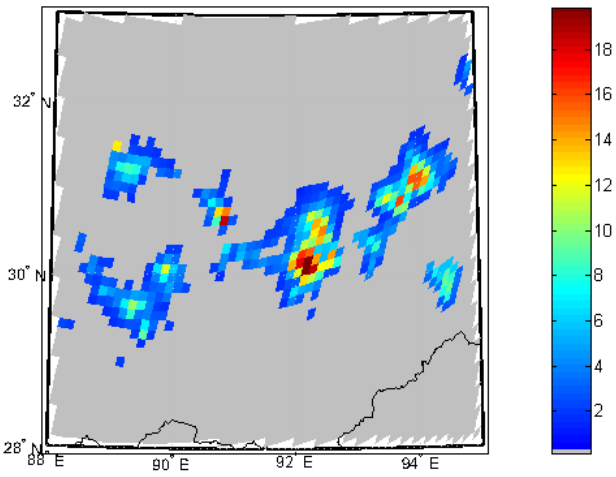

Figure 4.12 CDRD estimated precipitation map for 02/08/2009 at 11:35 UTC, colorscale in mm h^{-1}.

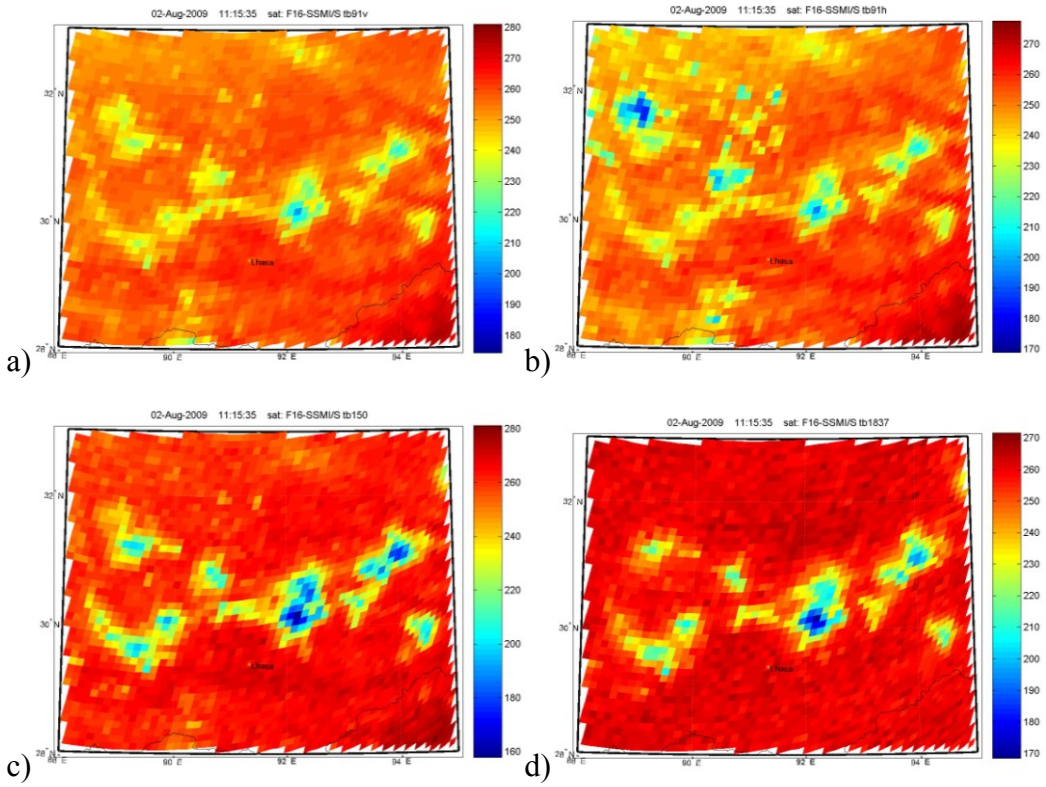

Figure 4.13 SSMI/S TB91H (a), TB91V (b), TB150 (c), TB183±7 (d) for the 02/08/2010 at 11:15UTC. Colorscale in K.

In Figure 4.13 are reported the SSMI/S TB maps more correlated to the estimated precipitation field.

The channels at 91 and 150 GHz are in window with high atmospheric transmittance, and also include strong contribution from the cloud-free surface. The 183.3±7 GHz channels is on the strong WV absorption band, but its weighting function is peaked in mid troposphere so a small surface contribution is expected, given the relatively dry atmosphere and the altitude of the ground.

The rainrate PDF of the CDRD estimates in 2010 (when 3 satellites are operational) is reported in Figure 4.14 for the larger MVIRI grid domain (see Figure 4.1, grid n. 4): the CDRD is able to estimate rather high rainrates (more than 60 mm h^{-1} for few IFOV). The 96% of the rainrates, however is below 20 mm h^{-1}.

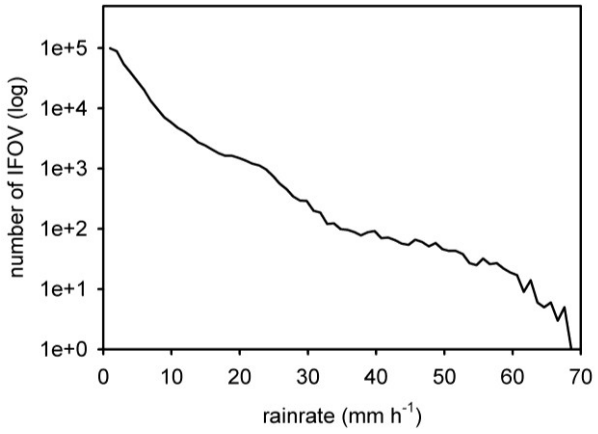

Figure 4.14 Rainrate PDF of the CDRD estimates for the 2010 monsoon season (JJAS)

4.3.2 Implementation and applications of IR-based statistical retrieval techniques

Two approaches have been attempted to make a synergistic use of MW derived precipitation fields and IR GEO satellites data. The first approach is of the type "entity based": clouds are identified by a dynamic threshold in the IR images as

objects and a nominal rainrate is assigned to them on the basis of the outputs of the MW based algorithms (CNAW technique). The second is fully statistic: an ANN is trained using as true precipitation values the outputs of MW retrievals (TANN technique).

4.3.2.1 Application of CNAW technique

The CNAW technique has been applied on the Tibetan Plateau after a off-line calibration based on statistical matching of the HPNA with MW based retrieval output, as described in Section 3.2.

As an example, the determination of the threshold to be used to delineate snowfall in the IR has been made by looking at Figure 4.15, where POD, FAR and ETS are reported as function of the IR threshold temperature. Here snowfall maps are assumed to be the truth and precipitation areas on IR images are defined by varying the threshold. The maximum value for ETS is reached for T = 239 K, and this value has been selected to fix the threshold for precipitation in the cold months.

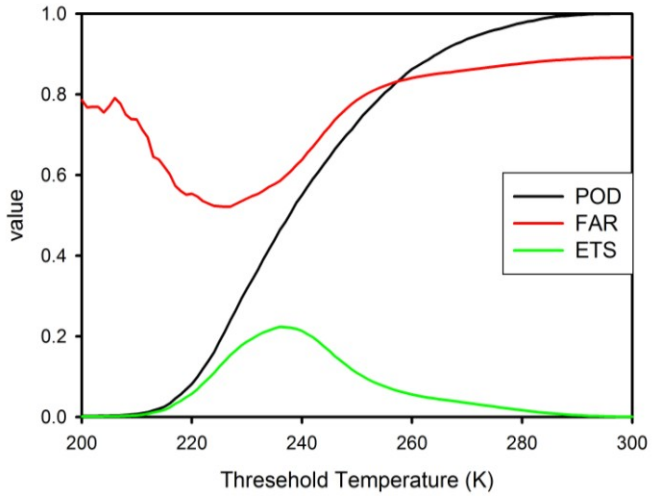

Figure 4.15 Dependence of skill parameters on the threshold temperature used to discriminate precipitation areas on IR images.

To determine the nominal rainrate to be assigned to summertime high precipitation NAW areas, the average rainrate as estimated by CDRD algorithm within each HPNA. In Figure 4.16 the distribution of averaged rainrate for HPNA is shown.

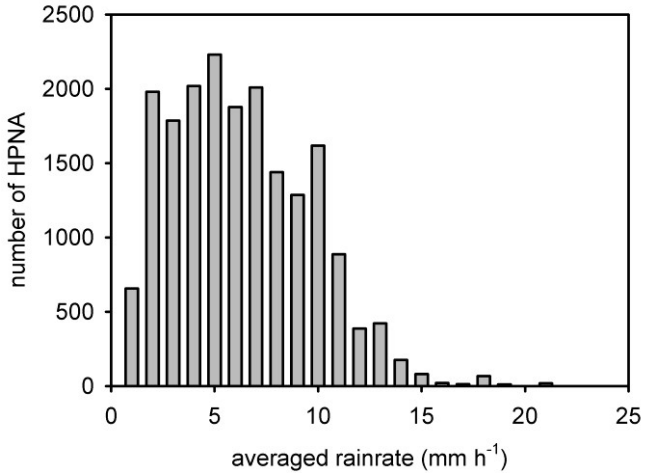

Figure 4.16 Distribution of HPNA averaged rainrate as computed by CDRD for 2009.

An example of CDRD estimate remapped onto the MVIRI grid is compared with the HPNA detected in the nearly simultaneous IR image in Figure 4.17.

Comparison with raingauges has been carried out for the case study occurred on 26-28 July 2009. The scatter plot between POD and FAR are reported in figure 4.18 for different cumulation intervals: 1 hour, 3, 12, and 24 hours, showing that the performance of the technique is rather poor for the 1 hour matching, but already with 3 hours cumulation the POD increases and FAR decreases and for the 24 hours cumulation the POD is always above 0.7 and the FAR below 0.4.

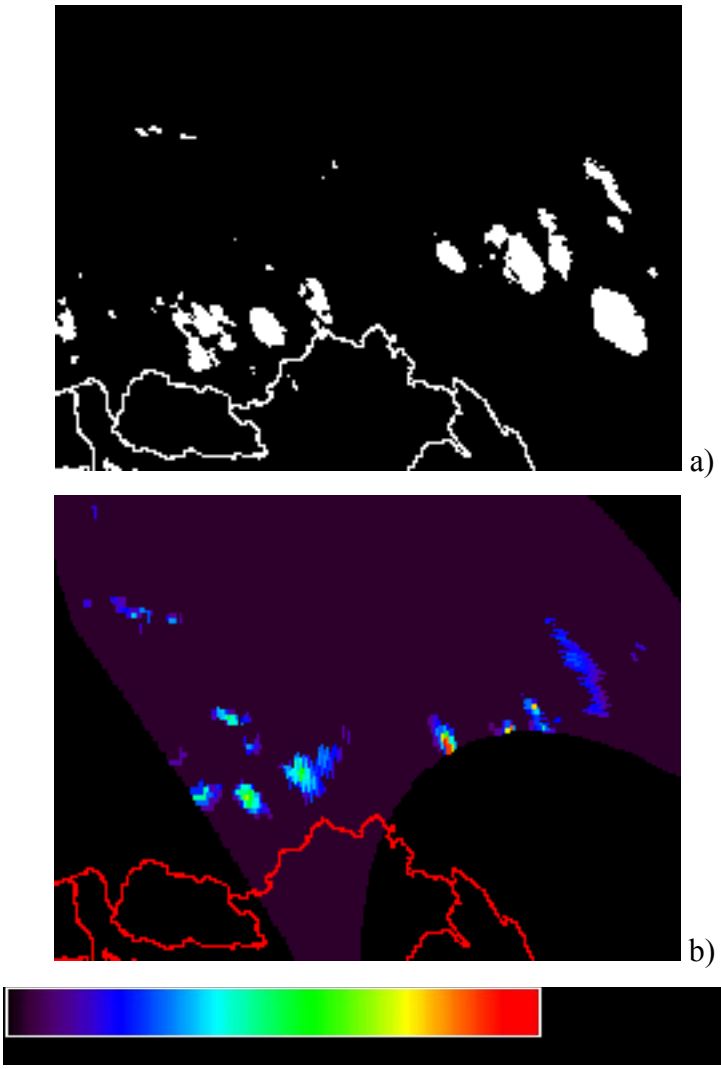

Figure 4.16 HPNA as extracted by the IR MVIRI image (a), and CDRD estimates remapped to match the MVIRI grid (b) for 18/06/2008 at 13:00 UTC

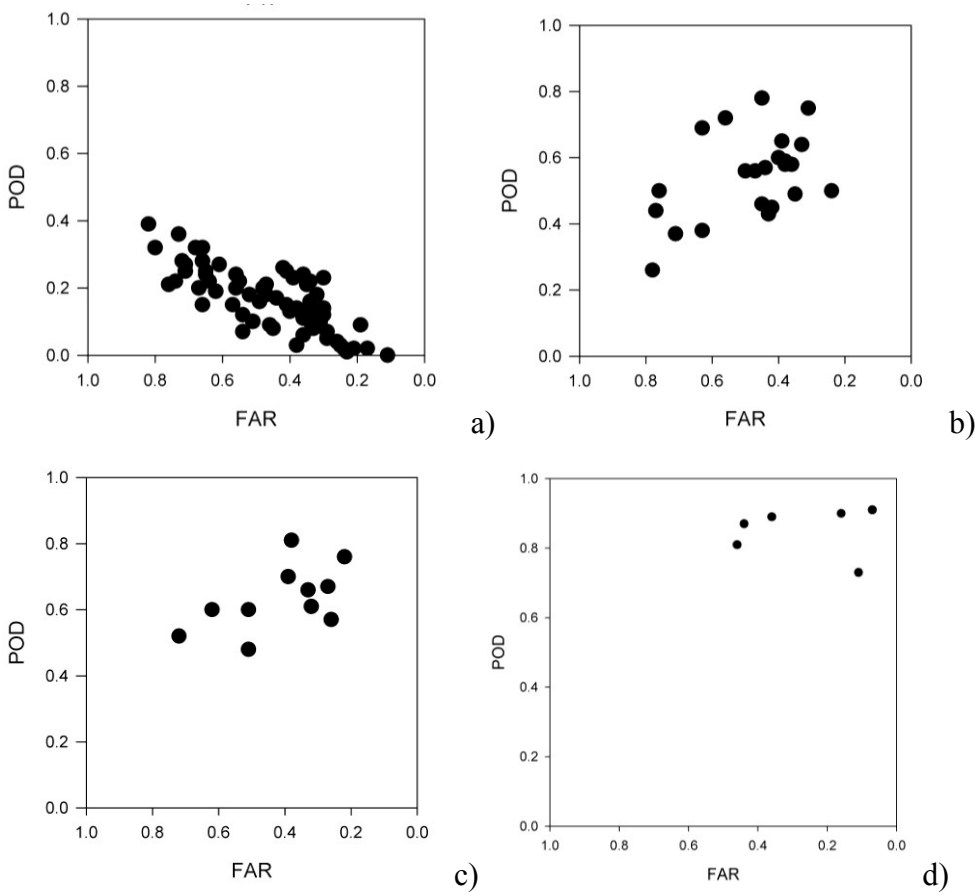

Figure 4.18 POD as function of FAR of raingauges validation of CNAW technique at different cumulation times for the case study occurred on 26-28/07/2009: 1hour (a), 3 hours (b), 12 hours (c) and 24 hours (d)

4.3.2.2 Application of TANN-R technique

As mentioned in section 3.3.4 two different implementation of TANN have been pursued in this work: TANN-R (trained on ground radar data during the monsoon season) and TANN-S (trained on CDRD estimates during the monsoon season). Both techniques have been trained on Cloudsat-CPR data in cold months.

To perform the TANN-R training and testing, the available case studies have been used for the Tibetan network, since in the Qinghai network area the MVIRI pixel size is very large (see Figures 4.1 and 4.2). A total of about 4.6 10^6 pixels in the

MVIRI grid have been used. The PDF of the rainrates measured by the Tibetan radar network is presented in Figure 4.19.

The curve is not fitted by an exponential function: the number of radar cells drops down between 1 and 3 mm h^{-1}, while there is a larger than expected amount of pixel between 20 and 40 mm h^{-1}, where the curve changes the concavity. The maximum detected rainrate by the radar network was 48 mm h^{-1}.

The maximum value of ETS reached during the testing of the monsoon season component of TANN-R was about 0.26, which is rather low, compared with other applications of ANN algorithms in other parts of the world. After the ANN has produced the Probability of Precipitation (PoP) a linear relationship that relates the PoP (between 0 and 1) to the rainrate (between 0 and 48 mm h^{-1}, following Figure 4.19) is applied in order to obtain rainrate maps.

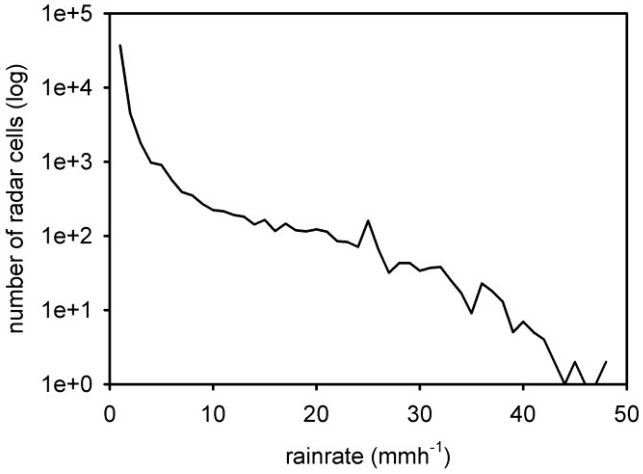

Figure 4.19 PDF of rainrate as measured by the Tibetan radar network for the pixel used for TANN-R training and testing.

As for the cold months component of TANN-R (and TANN-S as well), the calibration has been made by using Cloudsat-CPR retrieval described in Section 4.3.1.1, and the reference PDF is reported in Figure 3.3. (black curve). For this training, carried out on a total of 4 10^4 MVIRI grid pixels, higher values of ETS were reached (ETS = 0.58).

In Figure 4.20 are reported the instantaneous precipitation rate maps obtained from the TANN for cold months (showing a snowfall episode), and a monsoon season map (with convective cells).

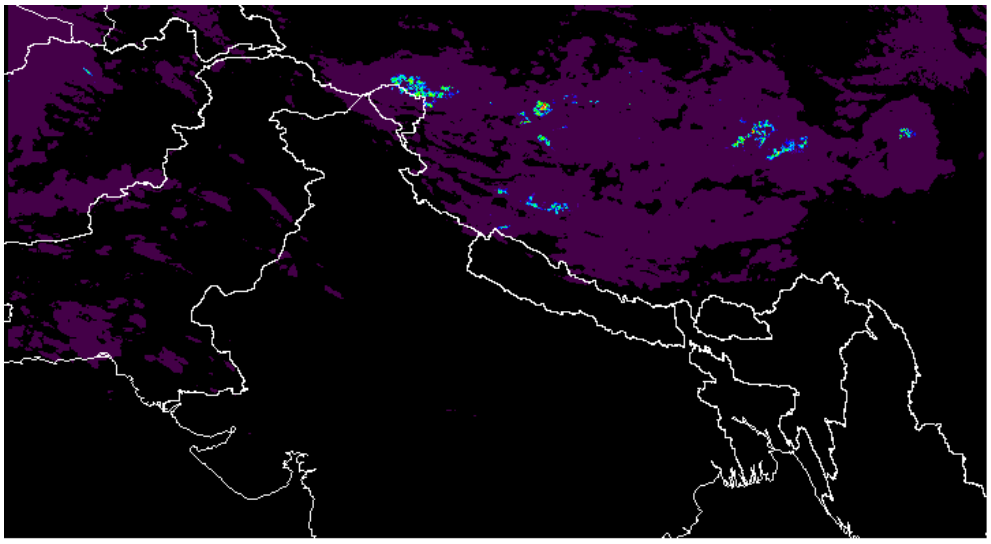

a)

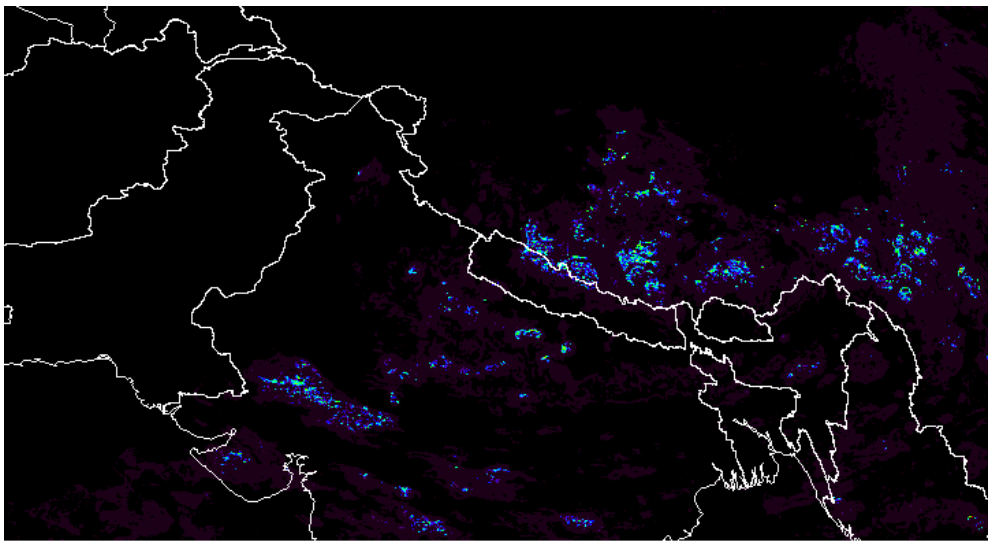

b)

Figure 4.20 Precipitation intensity maps derived from cold months TANN (a) for a snowfall episode occurred on 23/01/2010, and from the TANN-R algorithms (b) for a convective episode occurred on 16/07/2010.

The wintertime map shows wide very low precipitation rate area, with few spots with rates around 1 mm h^{-1}.
The rainrate during monsoon season is much higher, the rain area is smaller and precipitation is retrieved on pixel size spots, with very high spatial variability and sometime isolated precipitation pixel are found, probably due to noise in the original images.

4.3.2.3 Application of TANN-S technique

The cold months component of the TANN-S algorithm has the same ANN as TANN-R, as described above. The monsoon season component has been trained on CDRC estimates, whose PDF is reported on Figure 4.21 for the year 2010. If compared to Figure 4.19, the CDRD is able to estimate higher values of precipitation rate (few IFOV above 60 mm h^{-1}), and the shape of the distribution is more likely to be fitted by a power low. A possible reason for differences between radar and CDRD estimates PDF shapes cold be that the radar data are obtained on a small portion of the Plateau, while the CDRD estimates view extends over the whole area of interest, an in particular over the eastern part of the Plateau, where more intense convective systems are expected (Sugimoto and Ueno, 2010).
The training has been performed on 5.9 10^6 pixel on the MVIR grid, and the ETS of the selected ANN was about 0.41, sensitively higher than the one find during the TANN-S training.
In Figure 4.21 the TANN-S precipitation intensity map for the same episode as in Figure 4.20b is shown. Differences between the two versions of the algorithm can be noted (larger precipitation areas, higher rainrate peaks), and will be more deeply discussed in the next Sections.

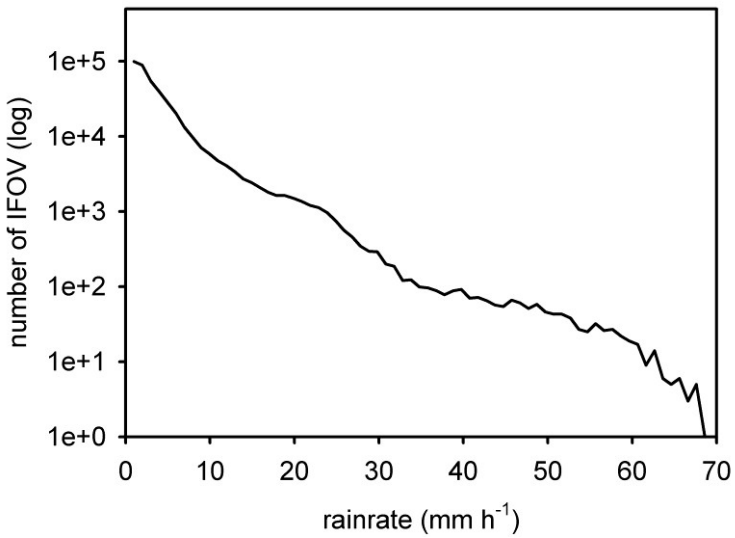

Figure 4.21 PDF of rainrate as estimated over the Plateau by the CDRD algorithm pixel used for TANN-S training and testing.

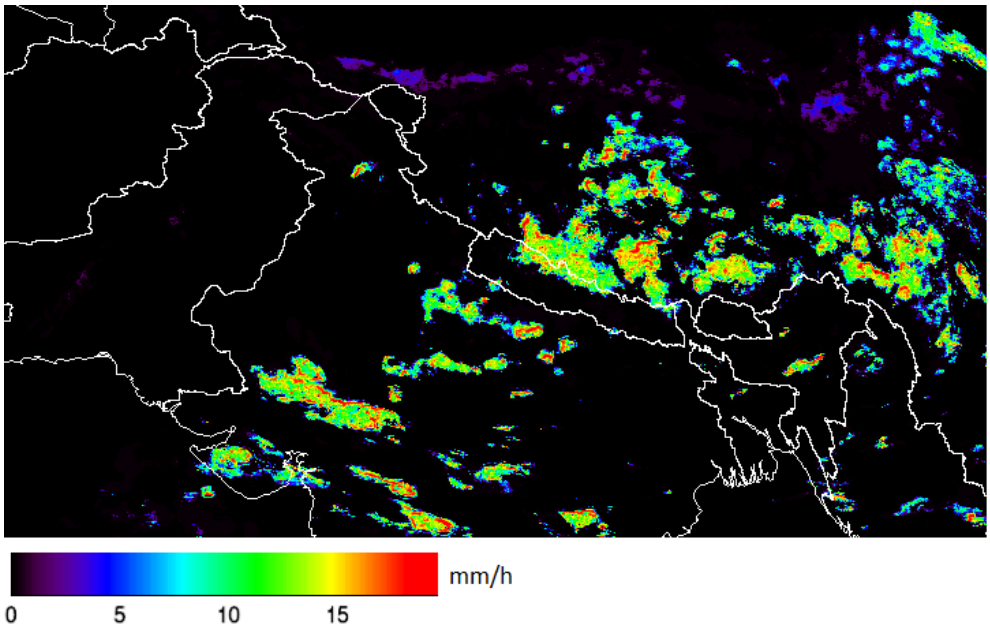

Figure 4.22 Precipitation intensity maps derived from the TANN-S algorithms for the same convective episode shown in Figure 4.19 occurred on 16/07/2010.

4.4 Algorithm intercomparison

Seven algorithms have been applied to the three year period over the Tibetan Plateau (see Table 4.1). Two are for instantaneous precipitation rate and cannot be used for operational monitoring, since they are onboard LEO satellites (Cloudsat and DMSP). Two are global products that uses PMW and IR data: the products can be downloaded at the resolution of 0.25°×0.25° for the Tibetan area, as 3 hourly cumulated maps. Three algorithms are IR based techniques that are calibrated following different approaches and using different data.

4.4.1 Daily precipitation amount

The first comparison is made by reducing all the products at the coarser grid (0.25°×0.25°) and computing daily cumulated values. Thus 5 PDF are derived for monsoon season and 4 for cold months, and are reported after normalization in figure 4.23 (a) and (b), respectively.

The monsoon season PDF of the global products are very similar: the values decreases exponentially after 10 mm, and more than 70 mm are recorded in a significant number of pixels (10^{-4} of the total). The other IR-based techniques behave rather differently. First, they have a large number of low rain amount pixel (between 2 and 10 mm), then the curves descend rapidly to very low values between 20 and 35 mm. Among the three IR-based techniques, the TANN-R reaches the highest values around 35 mm with a fraction of 10^{-4} of the total number of pixels, while TANN-S and CNAW have rather parallel shapes, with the latter showing higher values.

For the cold months the behaviors show differences and similarities. The TMPA product reaches large precipitation amounts as in the warmer months, while for CMORPH the value of 35 mm of precipitation is present a fraction of 10^{-4} of the

total number of considered pixel. Also in this case the IR-based techniques are decreasing more rapidly and the highest values at the 10^{-4}% fraction is 22 mm for CNAW and 26 mm for TANN.

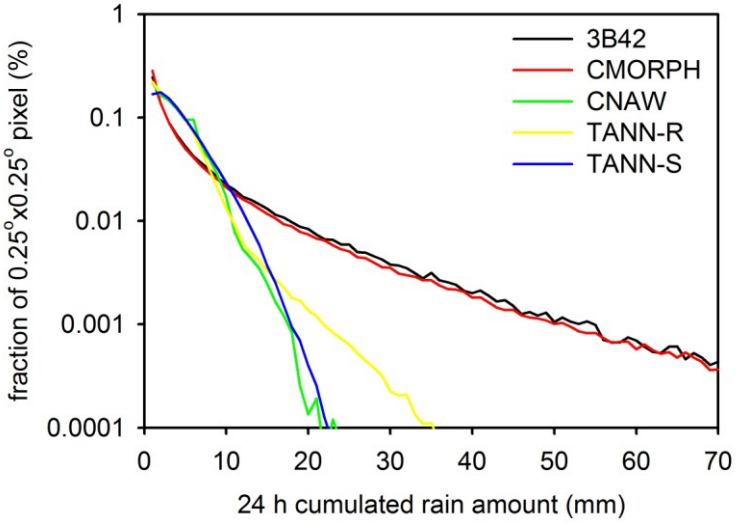

a)

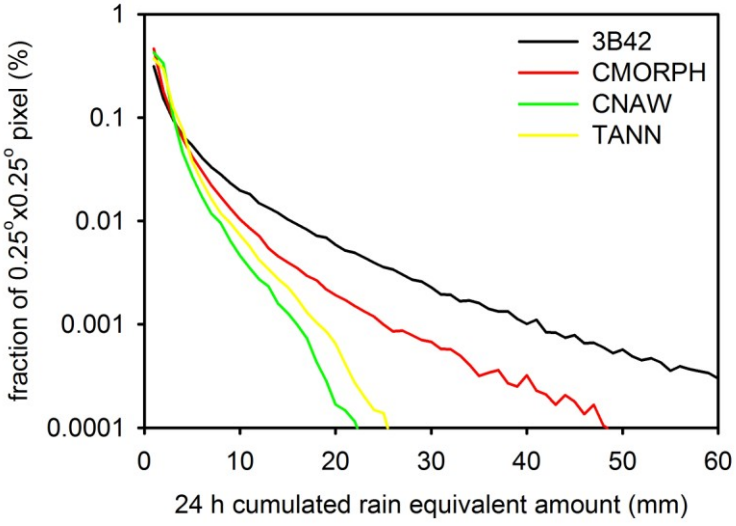

b)

Figure 4.23 Normalized PDF of 24 h rain amount at the 0.25°×0.25° resolution for the year 2009, for cold months (JFMAM-OND) (a), and monsoon season (JJAS).

Few preliminary conclusions can be drawn. The IR based techniques always overestimate the area with lower precipitation amounts, below 10 mm for summer and between 1 and 3 mm for clod months. On the other side, global techniques overestimates larger rain amounts. During monsoon season, could be likely to have an averaged rain amount over an 0.25°×0.25° area exceeding 70 mm, but this is very unlikely during cold months, when weak precipitation is expected.

During the monsoon season TANN-R is able to estimate larger rain amount than TANN-S, this could be due to the finer resolution of radar rainfall maps, that are able to estimate high rainrates, even if Figure 4.19 shows the ability of CDRD to estimate few pixels above 50 mm h^{-1}, while Figure 4.21 shows that our database of radar data is limited by lower rainrate values. Again it has to be mentioned the Tibetan radar network is located in a region where heavy rainfall are rarely observed.

Finally, the time series of Tibetan Plateau integrated daily mean rain amount is shown in figure 4.24 for all the monitoring technique considered in this work, keeping in mind that TANN-R and TANN-S coincide for cold months.

For the first two months the precipitation is very low: well below 0.5 mm for both the global products, but 3B42 shows few peaks above 1 mm, while IR base techniques have values between 1 and 2 mm on the average. A very large peak, probably due to snow at the ground, is estimated by TANN-R, and by other techniques but at markedly lower values, except CMORPH. Around day 80 CMORPH has a 10-day wide peak not sensed by other techniques, while between day 100 and 150 the techniques agree with rather constant averaged value around 1 mm, with some isolated peaks observed by 3B42. Around day 150 there is the onset of monsoon season TANN-R and TANN-S and the precipitation amount increases for all the techniques: average values are now between 3 and 5 mm, except for CMORPH, that keeps below the other curves.

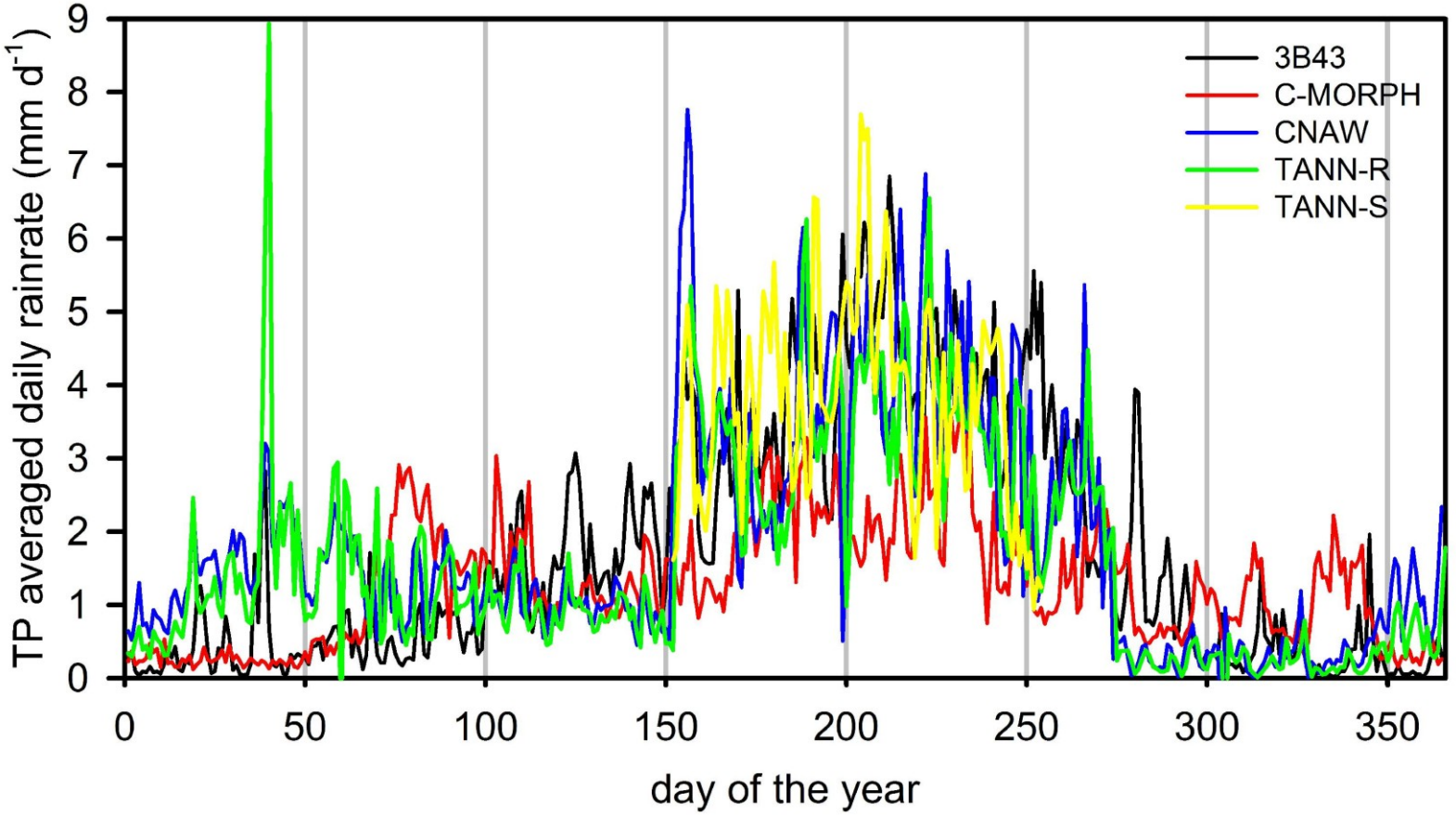

Figure 4.24 Time series of daily precipitation amount integrate over the Tibetan Plateau for the technique considered in this study

Sharp peaks, during 1 o 2 days, are seen during the monsoon season: sometimes they are observed by more than one technique, but in general not with the same values. Even TANN-R and TANN-S are far to be similar, with the latter generally overestimating.

Around day 300, after the monsoon season has finished, the amount of rain decreases with the agreement of all the techniques, except CMORPH, that in this case tends to overestimate precipitation amount. TANN and CNAW are highly correlated.

4.4.2 Case studies

On 24 August 2009 in the late morning (LT) a group of weak convective cells developed on the southern and eastern part of the Plateau and have been observed by both the Tibetan and Qinghai radar network. The data of all the estimation techniques have been remapped onto the coarse grid 0.25°×0.25° (except TANN-R and TANN-S) and cumulated over three hours in order to make all the estimates comparable. The derived maps are reported in Figure 4.25, where also the radar map is shown, reduced a the same resolution of the other products.

Radar network shows a precipitation structure with low precipitation in the 3 hours, and one small peak with cumulated rain around 10 mm (a). CMORPH (b) completely misses the precipitation structures, detecting only low rain accumulation but slightly misplaced with respect to radar observations. CNAW (c) detects several precipitating areas in the region, with rain amount comparable with radar observations, but also a misplacement is noted. The 3B42 (d) estimates is rather good in detecting rain areas, but the amount of rain is underestimated.

TANN-R (e) and TANN-S (f) show similar shapes in the precipitation patterns, and the wet areas is the largest among the estimates. The higher resolution shows

the presence of a structure of precipitation field not seen at lower resolution. TANN-S estimates higher rain amount than any other technique.

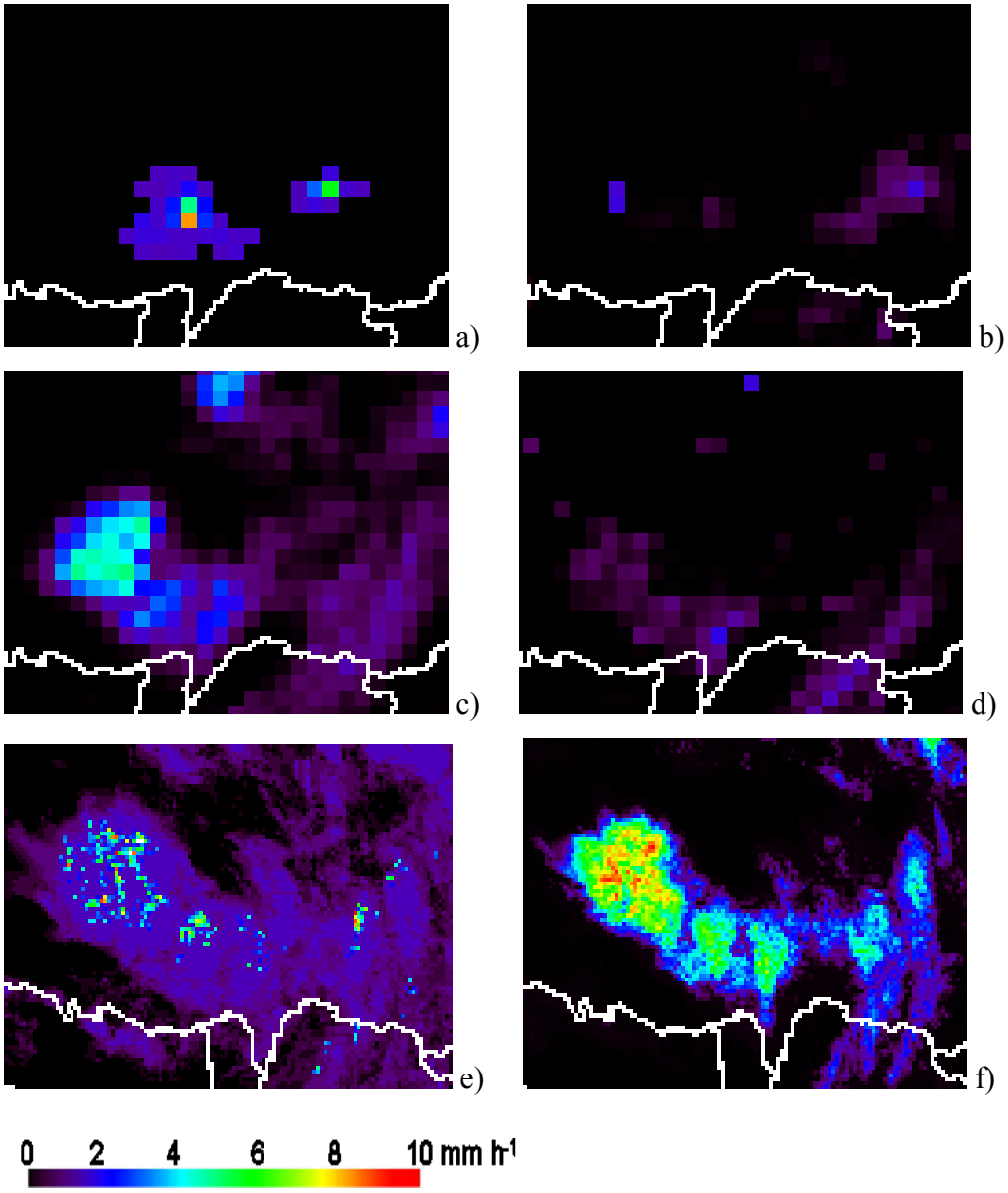

Figure 4.25 Three hourly cumulated rain as seen from different techniques: (a) QPE from Tibet ground radar network; (b) CMORPH; (c) 3B42; (d) CNAW; (e) TANN-R; (f) TANN-S.

On the same day, three hours before the first case stidy, on the eastern part of the Plateau, in the Qinghai Provice, weak convective cells developed, observed by the

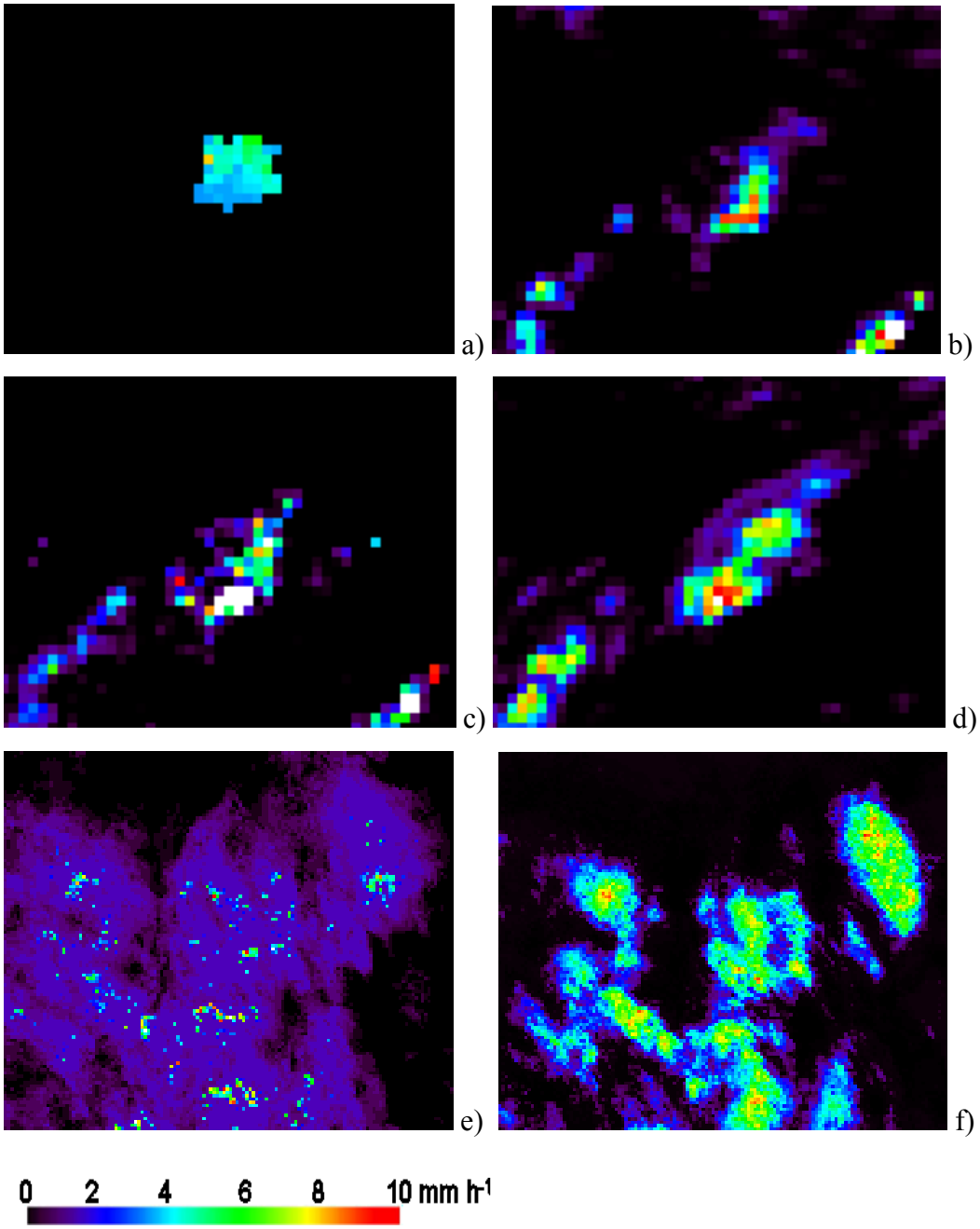

Figure 4.26 Three hourly cumulated rain as seen from different techniques: (a) QPE from Qinghai ground radar network; (b) CMORPH; (c) 3B42; (d) CNAW; (e) TANN-R; (f) TANN-S.

Qinghai radar network, and in Figure 4.26 are reported the radar 3 hours cumualted precipitation (a), and the corresponding estimates: CMORPH (b), 3B42 (c), CNAW (d), TANN-R (e) and TANN-S (f).

In this case all the techniques detect reasonably well the rain areas, but the rain amount is overestimated. Probably there is also a slight misplacement of the rain area, due to parallax problem, that in the Qinghai region is rather sever, given the high longitude with respect to the Meteosat 7 position (see figure 4.1).

Unfortunately, the available radar data were too few to make possible a systematic validation with significant statistics, and only visual matching of the precipitation patterns is possible.

However, the comparisons of the two case studies highlight the difficulties in getting reliable precipitation estimation over the Plateau: satellite estimation techniques based on different data and approaches give rain maps that markedly differs on many points of view. Increasing the cumulation time the outputs of the techniques converge to more similar description.

4.4.3 Annual maps

A final comparison can be considered by looking at the long term precipitation cumulation: Tibet Plateau annual cumulated maps are considered in this section. In Figure 4.27 the annual cumulated precipitation is reported for 3B42 (a), CMORPH (b), CNAW (c), and TANN-R (d). All the estimates find the maximum rain amount over the coast facing the Gulf of Bengal with other secondary peaks along the south slopes of Himalayan chain. Global products show a very dry Plateau: especially 3B42 estimates very low rain amount with relative abundance on the eastern part of the Plateau. Some artifacts can also be detected in the 3B42 maps: square boxes with relatively high spatial precipitation gradient can be due to the image segmentation used for the technique calibration.

The CMORPH map shows also a very dry Plateau, with less intense precipitation peaks on the south Himalayan side, and some patchy pattern also on the northern slopes. An artifact is probably present on the northern border of the Plateau, where a narrow strip of relatively higher cumulated precipitation follows the northern Plateau rim.

The CNAW map appears much different: higher precipitation amount (by a factor slightly lower than 2), the precipitation peak on the southern Himalayan slopes is missing, and relative high precipitation amount is found on the central and east Plateau. Correctly, CNAW finds also relatively high cumulated values on the eastern part of the domain, accordingly to other studies (Sugimoto and Ueno, 2010).

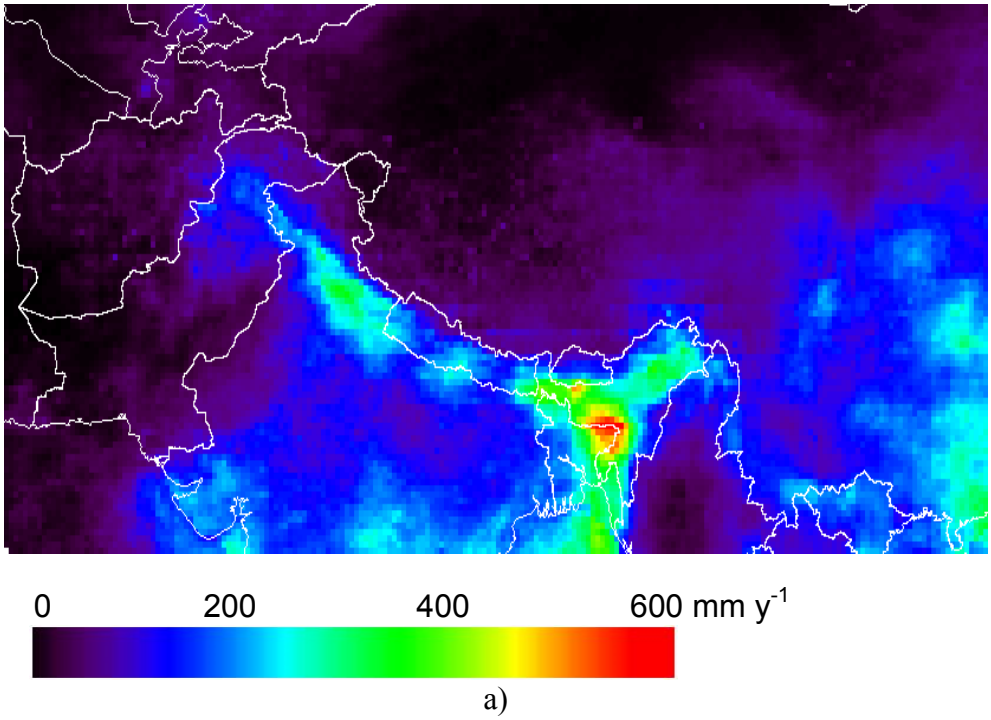

a)

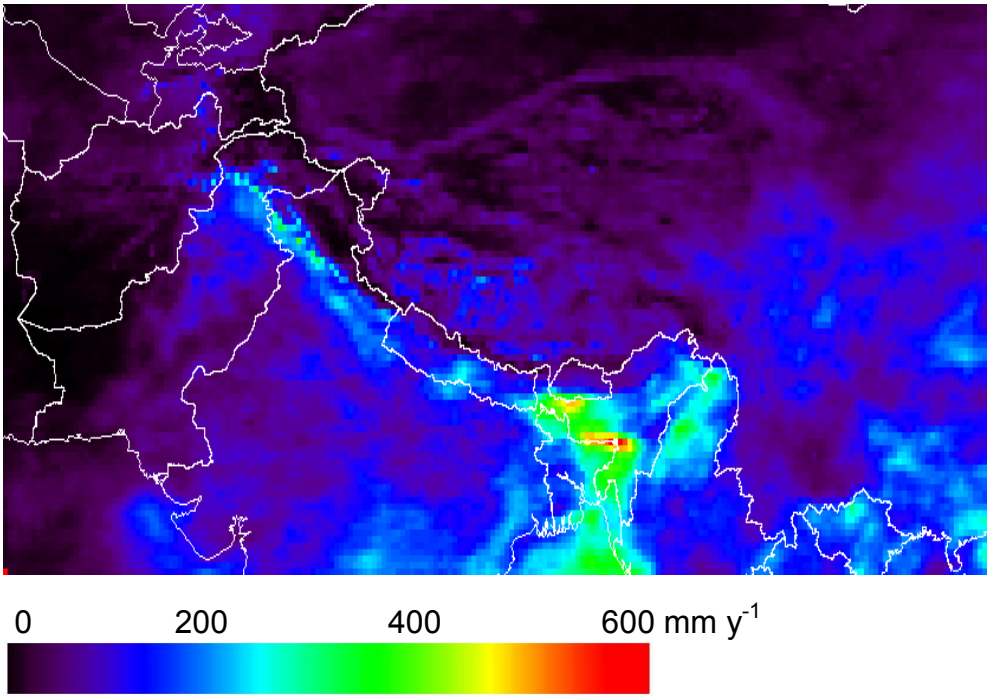

b)

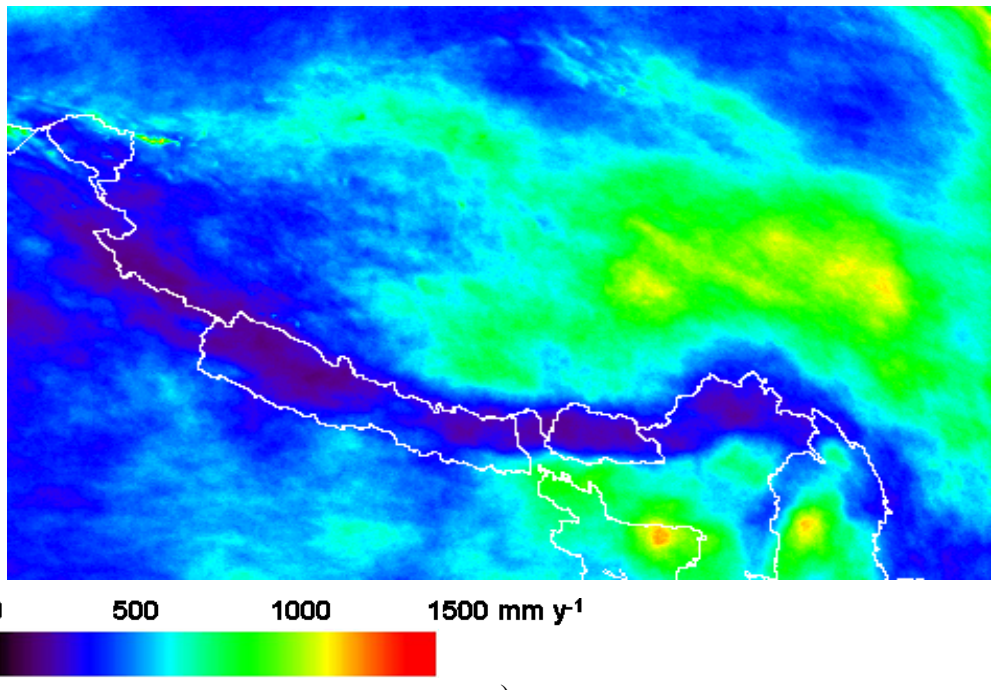

c)

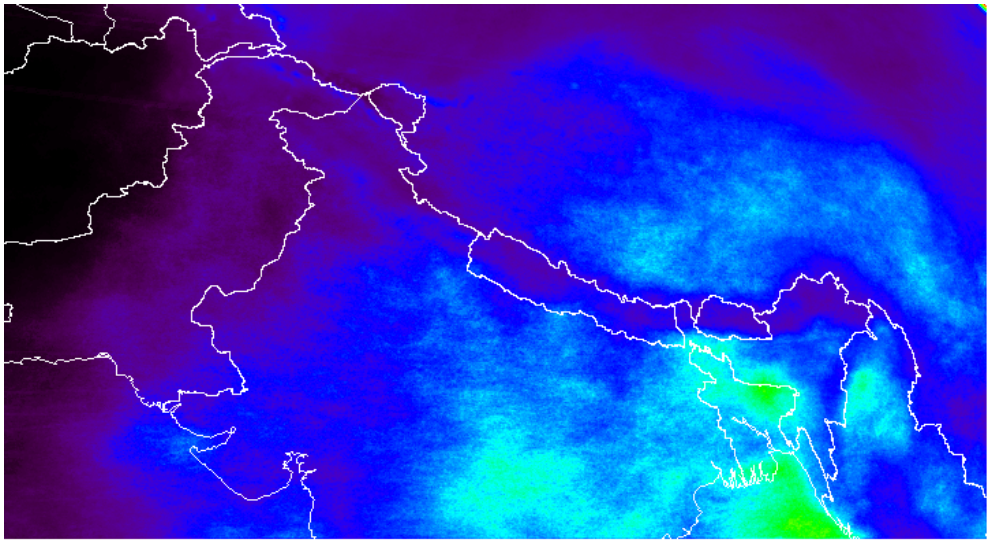

d)

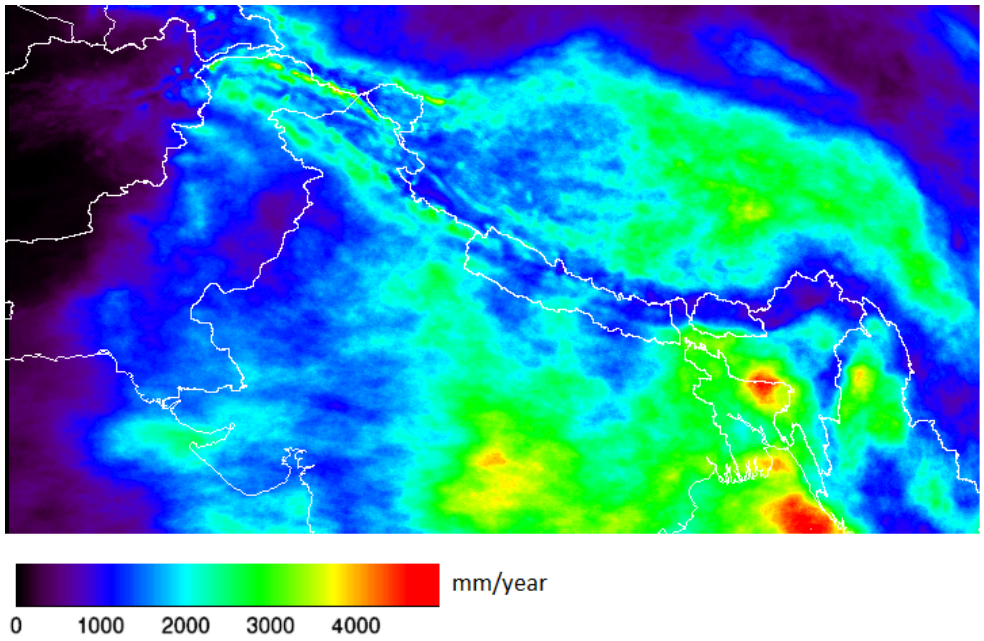

e)

Figure 4.27 Annual cumulated precipitation for year 2010 as computed from: 3B42 (a), CMORPH (b), CNAW (c), TANN-R (d) and TANN-S (e).

TANN-R shows lower cumulated values, weaker and less defined peaks on the Gulf of Bengal, no peaks on the Himalayan south slope and relatively wet eastern part of the Plateau.

The TANN-S maps estimates much higher precipitation amount, finds large peaks on the Gulf of Bengal and along the south Himalayan slope. Also the eastern part of the Plateau receives more precipitation than estimated by the other techniques.

As assessed for case studies and daily values, there are marked differences among the outputs of the different techniques, especially between global products (3B42 and CMORPH) and the IR-based techniques calibrated over the Plateau (CNAW, TANN-R and TANN-S). The basic difference is that global products are able to estimates higher rainrates than other techniques, but underestimates the extent of precipitation areas. Case studies show that global products can miss some area, while IR techniques always find large, low rainrate, patterns. On the single images, or daily means, this results in little differences, but if integrated on a whole year, results in large discrepancies. The setup of blended IR-MW techniques is a trade-off between the IR tendency to overestimate precipitation area size, and the MW inability of detecting low-moderate rainrates.

Further studies are needed to resolve these ambiguities, and the forthcoming full exploitation of the Global Precipitation Measurement mission will probably help on this task.

Conclusions

In this Thesis work, carried out in the frame of CEOP-AEGIS, an EU FP7 funded project, the problem of the precipitation monitoring over the Tibetan Plateau has been addressed. Data from ground based instruments, made available by the Chinese Meteorological Administration, are used for case studies and to feed multiplatform satellite precipitation retrievals.

The main focus is the implementation and applications for three years of data (2008, 2009 and 2010) of an array of satellite precipitation techniques. The work has been broken down as follows.

First, a sensitivity study on the capability of the most used satellite sensors to detect precipitation at the ground, assessed with respect to raingauges data for selected case studies, has been carried out. Results show that the overall behaviour of satellite sensor channels is quite different from the one well known at lower elevation surfaces, probably due to the strong surface signal in the PMW and the varying soil temperature across the day.

Then, two physically based techniques have been implemented for snow rate, based on Cloudsat-CPR data (during cold months) and rainrate derived from SSMI/S data (during monsoon season). These techniques, given the high revisiting time, are not suitable for direct use as precipitation monitoring tool, but are used as "calibrator" of multisensor techniques based on geostationary IR data.

Two approaches are tested to merge MW retrieval to IR data: entity based and fully statistical. The first approach requires the definition of precipitating area as separated entities, and the assignment of rainrates as determined by coincident MW estimates: at the beginning of this work, two techniques were selected CNAW and GCD, but the latter was abandoned because of the poor sensitivity over the Plateau.

The full statistical approach has been pursued by implementing an ANN technique, trained on ground radar data (TANN-R) or PMW retrieval (TANN-S)

for the monsoon season, and on snowfall retrieval from Cloudsat-CPR during cold months.

Finally, two well reputed global precipitation products have been considered for reference and intercomparison: the CMORPH and the TMPA product 3B42. All the techniques have been implemented for the 3 years and the results compared at different spatial and temporal scales.

The analysis of daily rain amount has shown that in general CMORPH and TMPA are able to estimate rain amount larger than the ones estimated by other techniques during the monsoon season. In cold months global techniques underestimate precipitation amount and areas, resulting in a dry bias with respect to IR calibrated techniques. Case studies compared with ground radar QPE data on convective episodes shown that global products tend to underestimate precipitation areas, while IR calibrated techniques provides reliable rainrate patterns, as compared with radar data. Unfortunately, the number of radar case studies was not large enough to allow significant validation studies, and also non data were available for cold months.

Annual precipitation cumulated maps show marked differences among the techniques: IR calibrated techniques generally overestimate precipitation amount by a factor of 2 with respect of global products.

Reasons for discrepancies are probably in the role the IR data have on the techniques: when the rain area delineation is based on IR, overestimation is likely to occur, while when the MW estimate is used, underestimation of low precipitation areas is expected. Further studies are needed to resolve these ambiguities, and the forthcoming full exploitation of the Global Precipitation Measurement mission will surely help on this task, and probably give a clearer picture of precipitation properties over the Tibetan Plateau.

Bibliography

Adler, R.F. and A.J. Negri, 1988, A satellite infrared technique to estimate tropical convective and stratiform rainfall. *J. Appl. Meteor*., **27**, 30-51.

Arkin, P.A. and B.N. Meisner, 1987, The relationship betweenl arge-scalec onvectivera infall and cold cloud over the western hemisphere during 1982-84. *Mon. Wea. Rev.,* **115**, 51-74.

Bishop, C. M., 1995, Neural Networks for Pattern Recognition. Clarendon Press - Oxford, pp 546

Caracciolo, C., Porcù, F. and F. Prodi, 2011, Drop Size Distribution over the Tibetan Plateau. *Geophysical Research Abstracts*, Vol. 13, EGU2011-12732, 2011, EGU General Assembly 2011.

Capacci, D., and B. J. Conway, 2005, Delineation of precipitation areas from MODIS visible and infrared imagery with artificial neural networks. *Meteor. Appl.*, **12,** 291–305

Capacci, D., and F. Porcù, 2009, Evaluation of a Satellite Multispectral VIS–IR Daytime Statistical Rain-Rate Classifier and Comparison with Passive Microwave Rainfall Estimates. *J. Appl. Meteor. Climatol.*, **48**, 284–300.

Casella, D., 2010, Analysis and Verification of the Cloud Dynamics and Radiation Database (CDRD) Methodology for Bayesian Retrieval of Precipitation with Passive Microwave Radiometer Instruments Onboard Satellites. PhD. Thesis, Department of Science, Technical Information and Communication, University of Rome "La Sapienza", Rome, Italy, 121 pp.

Casella, D., S. Dietrich, F. Di Paola, M. Formenton, A. Mugnai, F. Porcù, and P. Sanò, 2012, PM-GCD – a combined IR–MW satellite technique for frequent retrieval of heavy precipitation, *Nat. Hazards Earth Syst. Sci*., **12**, 231-240

Chen F. W. and D. H. Staelin, 2003 AIRS/AMSU/HSB precipitation estimates. *IEEE Trans. Geosci. Remote Sens*., **41**, 410-417

Doviak, R., J., and D. Zrnic, 1994, Doppler radar and weather observations, Dover Publications, 562 pp.

Duchon, C. E. and G. R. Essenberg, G. R., 2001, Comparative rainfall observations from pit and aboveground gauges with and without wind shields, *Water Resour. Res.*, **37**, 3253–3263.

Duchon, C.E. and C.J. Biddle, 2010, Undercatch of tipping-bucket gauges in high rain rate events. *Adv. Geosci*., **25**, 11–15.

Evans, L. J., and R. E. Shemo, 1996, A procedure for automated satellite-based identification and climatology development of various classes of organized convection. *J. Appl. Meteor*., **35**, 638-652.

Ferraro, R.R. and G.F. Marks, 1995, The development of SSM/I rain rate retrieval algorithms using ground based radar measurements. *J. Atmos. Oceanic Technol*., **12**, 755-770.

Ferraro, R. R., E. A. Smith, W. Berg, G. J. Huffman, 1998, A Screening Methodology for Passive Microwave Precipitation Retrieval Algorithms. *J. Atmos. Sci.*, **55**, 1583–1600.

Fujii, H. and T. Koike, 2001, Development of a TRMM/TMI Algorithm for Precipitation in the Tibetan Plateau by Considering Effects of Land Surface Emissivity. *J. Meteor. Soc. Japan*, **79**, 475-483.

Fujinami, H., and T. Yasunari, 2004, Sub-monthly variability of convection and circulation over and around the Tibetan Plateau during the boreal summer. *J. Met. Soc. Japan*., **82**, 1545-1564.

Grody, N. C., 1991: Classification of snow cover and precipitation using the Special Sensor Microwave/Imager (SSM/I). *J. Geophys. Res*., **96**, 7423–7435.

Hiley, M. J., M. S. Kulie, and R. Bennartz, 2011, Uncertainty Analysis for CloudSat Snowfall Retrievals. *J. Appl. Meteor. Climatol.*, **50**, 399–418.

Hsu, K., X. Gao, S. Sorooshian, and H. V. Gupta, 1997: Precipitation estimation from remotely sensed information using artificial neural networks. *J. Appl. Meteor.*, **36,** 1176–1190.

Huffman, G. J., D. T. Bolvin, E. J. Nelkin, D. B. Wolff, R. F. Adler, G. Gu, Y. Hong, K. P. Bowman, and E. F. Stocker, 2007, The TRMM Multisatellite Precipitation Analysis (TMPA): Quasi-Global, Multiyear, Combined-Sensor Precipitation Estimates at Fine Scales. *J. Hydrometeor*, **8**, 38–55

Iguchi, T., T. Kozu, R. Meneghini, J. Awaka, K. Okamoto, 2000, Rain-Profiling Algorithm for the TRMM Precipitation Radar. *J. Appl. Meteor.*, **39**, 2038–2052.

Joyce, R. J., J. E. Janowiak, P. A. Arkin, and P. Xie, 2004, CMORPH: A method that produces global precipitation estimates from passive microwave and infrared data at high spatial and temporal resolution.. *J. Hydromet*., **5**, 487-503.

Kidd, C. and Levizzani, V., 2011, Status of satellite precipitation retrievals, *Hydrol. Earth Syst. Sci*., **15**, 1109-1116.

Kotroni, V, Lagouvardos K Defer E, Dietrich S, Porcù F, Medaglia CM, Demirtas M, 2006: The Antalya 5 December 2002 storm: observations and model analysis. *J. Appl. Meteor*., **45**, 576-590.

Kulie, M. S., and R. Bennartz, 2009, Utilizing Spaceborne Radars to Retrieve Dry Snowfall. *J. Appl. Meteor. Climatol.*, **48**, 2564–2580

Kursinski, A. L., S. L. Mullen, 2008, Spatiotemporal Variability of Hourly Precipitation over the Eastern Contiguous United States from Stage IV Multisensor Analyses. *J. Hydrometeor*, **9**, 3–21.

Lanza, L. G., E. Vuerich, and I. Gnecco, 2010, Analysis of highly accurate rain intensity measurements from a field test site. *Adv. Geosci.,* **25**, 37-44.

Laviola, S., and V. Levizzani, 2010, The 183-WSL fast rain rate retrieval algorithm: Part I: Retrieval design, *Atmos. Res*., **99**, 443-461.

Leitinger, G., N. Obojes and U. Tappeiner, 2010, Accuracy of winter precipitation measurements in alpine areas: snow pillow versus heated tipping bucket rain gauge versus accumulative rain gauge, EGU General Assembly 2010, held 2-7 May, 2010 in Vienna, Austria, p.5076.

Lensky, I. M. and D. Rosenfeld, 1996, Estimation of Precipitation Area and Rain Intensity Based on the Microphysical Properties Retrieved from NOAA AVHRR Data. *J. Appl. Meteor*., **36**, 234-242

Levizzani, V., P. Bauer and J. F. Turk, (eds.), 2007, Measuring precipitation from space: EURAINSAT & the future, Advances in global change research, Vol. 28, Springer, 724 pp.

Li, M., Y. Ma, W. Ma, I., Hirohiko, F. Sun and S. Ogino, 2011, Different characteristics of the structure of atmospheric boundary layer between dry and rainy periods over the northern Tibetan Plateau. *Sciences in Cold and Arid Regions*, **3**, 509–516

Li, Y. W. Yun, S. Yang, H. Liang, G. Shouting, and R. Fu, 2008, Characteristics of summer convective systems initiated over the Tibetan Plateau. Part 1: Origin, track, development, and precipitation. *J. Appl. Meteor. Climatol*., **47**, 2679- 2695.

Ma, Y, H, Ishikawa, O. Tsukamoto, M. Menenti, Z. Su, T. Yao, T. Koike and T Yasunari, 2003, Regionalization of surface fluxes ove rheterogeneous landsacape of the Tibetan Plateau by using satellite remote sensing. *J. Meteor., Soc., Japan*, **81**, 277-293.

Ma, Y., M. Li, X. Chen, S. Wang, R. Wu, W. Ma, L. Zhong, B. Wang, C. ZHU, and T, YAO, 2011, Third Pole Environment (TPE) program: a new base for the study of atmosphere―land interaction over the heterogeneous landscape of the Tibetan Plateau and surrounding areas, Proc. of IUGG2011, Melbourne, 343, 110-117.

Machado, L. A. T., and W. B. Rossow, 1993, Structural characteristics and radiative properties of tropical cloud clusters. *Mon. Wea. Rev*., **121**, 3234–3260.

Marshall, J. S. and W. McK. Palmer, 1948, The Distribution of Raindrops with Size. *J. Meteorol*., **5**, 165-166.

Martin, D.W., R. A. Kohrs, F. R. Mosher, C. M. Medaglia, and C. Adamo, 2008, Over-Ocean Validation of the Global Convective Diagnostic, J. Appl. Meteor. Climatol., 47, 525–543

Mosher, F.R., 2001, A satellite diagnostic of global convention, Preprints, 11th Conf on Satellite Meteorology, Madison, WI. Amer. Meteor. Soc., 416-419

Negri, Andrew J., Robert F. Adler, Peter J. Wetzel, 1984, Rain Estimation from Satellites: An Examination of the Griffith-Woodley Technique. *J. Climate Appl. Meteor.*, **23**, 102–116.

Nurmi, P., 2003: Recommendations on the verification of local weather forecasts. 11 ECMWF Tech. Memo. N. 430, 19pp.2/29/2012

Pankiewicz, G. S., C. J. Johnson, and D. L. Harrison, 2001, Improving radar observations of precipitation with a Meteosat neural network classifier. *Meteor. Atmos. Phys.*, **76,** 9–22

Porcú F., M. Borga and F. Prodi, 1999: Rainfall estimation by combining radar and infrared satellite data for nowcasting purposes. *Meteorol. Appl*., **6**, 289-300.

Porcù F., Prodi F., Dietrich S., Mugnai A. and Bechini R., 2000, Multisensor estimation of severe rainfall events, *Proc. of the 2000 Eumetsat Meteorological Satellite Data Users' Conference*. EUM P 29, Eumetsat, Darmstadt, 371-378

Prodi, F. Caracciolo, C., D'Adderio, L.P., Gnuffi, M., Lanzinger, E., 2011. Comparative Investigation of Pludix disdrometer capability as Present Weather Sensor (PWS) during the Wasserkuppe campaign. *Atm.Res.,* **99**, 162-173.

Rubel, F., 1996. Scale dependent statistical precipitation analysis. *Proc. of the Int. Conf. on Water Resour. & Environ. Res.*, 29-31 ottobre 1996, Kyoto, 317-324

Sanò, P., The Cloud Dynamics and Radiation Database (CDRD) Approach for Precipitation Retrieval by Means of Satellite Based Microwave Radiometry. PhD thesis, Department of Computer, Systems and Production Engineering, Tor Vergata University of Rome "Tor Vergata", Rome, ITALY,, 2010.

Sanò, P., D.Casella, A.Mugnai, G.Schiavon, E.A.Smith, and G.J.Tripoli, 2012, Bayesian Estimation of Precipitation from Satellite Passive Microwave Measurements using CDRD Technique. Part 1: Algorithm Description and Applications over Italy. *IEEE Trans. Geo. Rem. Sens.,* submitted

Sevruk, M. Ondrás, B. Chvíla, 2009, The WMO precipitation measurement intercomparisons, *Atmos. Res.,* **92**, 376-380.

Shimizu, S., K. Ueno, H. Fujii, H. Yamada, R. Shirooka, and L. Liu, 2001, Mesoscale characteristics and structures of stratiform precipitation on the Tibetan Plateau. *J. Meteor. Soc. Japan*, **79**, 435-461.

Smith, E. A., and Coauthors, 1998, Results of WetNet PIP-2 project. *J. Atmos. Sci*., **55**, 1483–1536.

Spencer, W., H. M. Goodman, and R. E. Hood, 1989, Precipitation retrieval over land and ocean with the SSM/I: Identification and characteristics of the scattering signal. *J. Atmos. Oceanic Technol.*, **6**, 254–273.

Sugiura, K., D. Yang, T. Ohata, 2003, Systematic error aspects of gauge-measured solid precipitation in the Arctic, Barrow, Alaska. *Geophysical Research Letters,* **30**, 1-5.

Sugimoto, S. and K. Ueno, 2010, Formation of mesoscale convective systems over the eastern Tibetan Plateau affected by plateau scale heating contrasts, *J. Geophys. Res*., **115**, D16105

Tripoli, G. J., 1992: A Nonhydrostatic Mesoscale Model Designed to Simulate Scale Interaction. *Mon. Wea. Rev.*, **120**, 1342–1359.

Tokay, A., D.B. Wolff, K.R. Wolff and P. Bashor, 2003, Rain Gauge and Disdrometer Measurements during the Keys Area Microphysics Project (KAMP). *J. Atmos. Oceanic Technol.*, **20**, 1460-1477.

Ueno, K., N. Endho, T. Ohta, H. Yabuki, T. Koike, M. Koike, T. Ohata and Y. Zhang,1994, Characteristics of precipitation distribution in Tanggula, monsoon, 1993. *Bull. of Glac. Res.,* **12**, 39-47.

Ueno, K., 1998, Characteristics of Plateau-scale precipitation in Tibet estimated by satellite data during 1993mosoon season. *J. Meteor. Soc. Japan*, **76**, 533-548.

Ueno, K., S. Sugimoto, T. Koike, H. Tsutsui, and X. Xu, 2011, Generation processes of mesoscale convective systems following mid-latitude troughs around the Sichuan Basin. *J. Geophys. Res*., **115**, D16105

Uyeda, H., H. Yamada, J. Horikomi, R. Shirooka, S. Shimizu, L. Liu, K. Ueno, H. Fujii and T. Koike, 2001, Characteristics of Convective Clouds Observed by a Doppler

Radar at Naqu on Tibetan Plateau during the GAME-Tibet IOP. *J. Meteor. Soc. Japan*, **79**, 436-474.

Vuerich, E., Monesi, C., Lanza, L. G., Stag, L., & Lanzinger, E. (2009). WMO Field intercomparison of rainfall intensity gauges. *World Meteorological Organisation - Instruments and Observing Methods Rep. No. 99, WMO/TD No. 1504* , 286.

World Meteorological Organization, 2008, Guide to meteorological instruments and methods of observations, WMO-n 8, 7th edition, Geneva, 681 pp.

Xu, W., and E. J. Zipser, 2011, Diurnal Variations of Precipitation, Deep Convection, and Lightning over and East of the Eastern Tibetan Plateau. *J. Climate*, **24**, 448–465.

Yao, T. and G. Greenwood, 2009, A New "Polar" Program: Third Pole Environment (TPE) Workshop; Beijing, China, 14–16 August 2009. *Eos Trans. AGU*, **90**, 515.

Yao, Z., W. Li, Y. Zhu, B. Zhao, and Y. Chen, 2001, Remote Sensing of Precipitation on the Tibetan Plateau Using the TRMM Microwave Imager. *J. Appl. Meteor*., **40**, 1381-1392.

Yin, Z-Y, X. Zhang, X. Liu, M. Colella, and X. Chen, 2008, An Assessment of the Biases of Satellite Rainfall Estimates over the Tibetan Plateau and Correction Methods Based on Topographic Analysis. *J. Hydrometeor*, **9**, 301–326.

Acknowledgements

The work described here has been supported by the European Commission (Call FP7-ENV-2007-1 Grant nr. 212921) as part of the CEOP-AEGIS project (www.ceop-aegis.org) coordinated by the Université de Strasbourg.
The availability of radar and raingauge data was granted by prof. Liping Liu of the China Meteorological Administration, and the help of Wei Zhuang in data managing is acknowledged.
The group headed by dr. Alberto Mugnai al the ISAC-CNR in Rome, provided the CDRD estimates and the UW-NMS outputs, and particular thanks go to dr. Paolo Sanò and dr. Daniele Casella.
Satellite data have been downloaded free as follows:
The MODIS product was downloaded from :
http://laadsweb.nascom.nasa.gov
The AMSR-E L2A product was downloaded from :
http://nsidc.org/data/amsre/index.html
The 3B24 product was downloaded from NASA-GESDIS server at: http://mirador.gsfc.nasa.gov/, while CMORPH products have been downloaded from the NOAA-CPC ftp site: ftp.cpc.ncep.noaa.gov/precip/global_CMORPH/.
The MVIRI product was downloaded from the EUMETSAT Earth Observation Portal:
(http://www.eumetsat.int/Home/Main/DataProducts/ProductNavigator/index.htm?l=en)
The 2A25 higher product level of TRMM PR was download from:
http://pmm.nasa.gov/TRMM/products-and-applications

I wish to express my sincere gratitude to my advisor Dr. Federico Porcù for his guidance, important technical and scientific contributes to my thesis. I would like to thanks my colleague Lisa Milani for her technical and moral support gave me.

A would like to thanks Dr. Pietro Domenico de Cosmo for his technical contribute.

Outside the work environment I would like to thanks my parents and all my friends gave me their best feelings refilled my heart of positive energy.